Towards High-performance Force-controlled Pneumatic Actuator with Long Transmission Lines:

A Novel Nonlinear Integral Sliding Surface and a New Multimodal Optimization Algorithm

by

Khurram Mahmood Butt

A Thesis submitted to the Faculty of Graduate Studies of
The University of Manitoba
in partial fulfillment of the requirements for the degree of

DOCTOR OF PHILOSOPHY

Department of Mechanical Engineering
University of Manitoba
Winnipeg, Manitoba

December 2018

Preface

This thesis is a result of doctoral research completed by **Khurram Mahmood Butt** under the supervision of **Dr. Nariman Sepehri**. It consists of two published and one submitted for publication research articles. The contents of constituting research articles are re-formatted and re-arranged to present a unified thesis document.

A version of Chapters 2 and 3 and some parts of Chapter 1 has been published as a research article titled **"Globalized and bounded Nelder-Mead algorithm with deterministic restarts for tuning controller parameters: Method and application"** in **"*Optimal Control Applications and Methods*"**. The article was co-authored by **Khurram Mahmood Butt, Ramhuzaini Abd. Rahman, Nariman Sepehri,** and **Shaahin Filizadeh**. For this article, the contribution of each co-author was as follows:
Butt conceived, designed, developed and coded a novel multimodal optimization algorithm so-called "Globalized and Bounded Nelder-Mead Algorithm with Deterministic Restarts". He evaluated the performance of the algorithm using complex multimodal optimization benchmarks and applied the algorithm to the model-based offline tuning of controller parameters. He also conducted experiments, did data analysis, and wrote the article. **Rahman** designed and constructed the test-rig and the simulator for experiments. **Sepehri** initiated and supervised the research and reviewed the contents of the article. **Filizadeh** reviewed the work related to optimization.

A version of Chapter 4 and some parts of Chapter 1 has also been published as a research article titled **"Model-free online tuning of controller parameters using a globalized local search algorithm"** in **"*Optimal Control Applications and Methods*"** as a research article. The article was co-authored by **Khurram Mahmood Butt** and **Nariman Sepehri**. For this article, the contribution of each co-author was as follows:

Butt designed and constructed the setup and method for model-free online tuning of controller parameters. He conducted all experiments, did data analysis, and wrote the article. **Sepehri** supervised the research and reviewed the contents of the article.

A version of Chapters 5 and 6 and some parts of Chapter 1 has been submitted as a research article titled **"A nonlinear integral sliding surface to improve the transient response of a force-controlled pneumatic actuator with long transmission lines"** for publication to **"*Journal of Dynamic Systems, Measurement and Control*"**. The article was co-authored by **Khurram Mahmood Butt** and **Nariman Sepehri**. For this article, the contribution of each co-author was as follows:

Butt developed the nonlinear integral sliding surface using which he designed a sliding mode controller that improved the transient response of a force controlled pneumatic actuator with long transmission lines. He also designed and constructed the experimental setup, an MRI-compatible pneumatic gripper. He conducted simulation/experimental tests, did data analysis, and wrote the research article. **Sepehri** supervised the research and reviewed the contents of the article.

Abstract

A force-controlled pneumatic actuator with long connecting pneumatic tubes is a well-accepted solution to develop MRI-compatible force control applications. Such an actuator represents an uncertain, second-order, nonlinear system with input delay. The integral sliding mode control, because of guaranteed robustness against matched uncertainties throughout the system response, provides a favorable option to design a robust controller for the actuator. However, if the controller is based on a linear integral sliding surface, the response of the actuator overshoots, especially when there are large initial errors. Minimizing overshoot results in a smaller controller bandwidth and a slower system response. This thesis presents a novel nonlinear integral sliding surface to improve the transient response of the actuator. The proposed surface is a linear integral sliding surface augmented by a nonlinear function of tracking error and does not have a reaching phase when there are initial errors and even multiple steps in the desired trajectory. The surface enables the integral sliding mode controller to offer variable damping during the system response and minimizes the overshoot without compromising the controller bandwidth, rise, and settling times. The thesis also implements logically driven, time-efficient tuning of controller for desired transient response of the actuator. For this purpose, first a novel multimodal optimization algorithm is proposed which has better globalization and lower numerical cost as compared to the evolutionary, swarm and available globalized local search optimization methods. Next, the effectiveness of the proposed algorithm is examined for model-based and model-free tuning of a position controller for a servo pneumatic system whose performance has been reported in another doctoral thesis after rigorous trial-and-error tuning. On yielding better results, the same algorithm-based tuning is used to tune the force controllers having the linear and proposed nonlinear integral sliding surfaces for desired actuator response and performance comparison. Simulation studies and

experimental tests conducted on a prototype MRI-compatible test rig show that the controller based on the proposed sliding surface successfully eliminates the overshoot without compromising the controller bandwidth, rise, and settling times. It also outperforms the controller having a linear integral sliding surface. The thesis also establishes the asymptotic stability of the proposed controller using Lyapunov's stability criterion.

Acknowledgments

In the name of Allah, the Most Beneficent, the Most Merciful.

First and foremost, all praises and thanks to Allah, the Almighty. I could not have completed this thesis without His countless favors and blessings.

I owe the deepest gratitude to my research supervisor, Dr. Nariman Sepehri, for helping me right when I needed the most. I am highly indebted to him for his invaluable guidance, support, and words of motivation throughout the research. It was a great privilege and honor to work under his supervision. I would also like to express my sincere thanks to the members of the advisory committee, Dr. Subramaniam Balakrishnan, and Dr. Udaya Annakkage for their comments and valuable insights, which greatly improved the thesis.

I would like to thank the Natural Sciences and Engineering Research Council (NSERC) of Canada for providing financial support for this research. I would also like to acknowledge the financial support from the University of Manitoba Canada for doctoral studies in the form of International Graduate Student Entrance Scholarship (IGSES), International Graduate Student Scholarship (IGSS), and the University of Manitoba Graduate Fellowship (UMGF) awards. Acknowledgment is also due to the Government College University Lahore of Pakistan for granting me the thesis leave for Ph.D. in Canada.

Special thanks are due to my beautiful wife, Iram Khurram, and my beloved children, Arsh, Adan and Anaya for their love, prayers, sacrifices and indefinite support throughout this pursuit. May Allah protect and shower His mercy on all of them in this world and hereafter.

Finally, I would like to place on record my gratitude for all those who directly or indirectly lent their hand in this venture.

Dedication

I dedicate this thesis to my parents, Shahida Butt and Mahmood Ahmed Butt, and grandmother, Khalida Begum, who brought me up with unconditional love and sacrificed their own needs for my education and well-being.

Table of Contents

List of Figures

List of Tables

List of Acronyms

DFT	Discrete Fourier Transform
GA	Genetic Algorithm
GBNM	Globalized and Bounded Nelder-Mead Algorithm
LISS	Linear Integral Sliding Surface
MSP	Multiple Step Polynomials
NLISS	Nonlinear Integral Sliding Surface
PSO	Particle Swarm Optimization
SMC	Sliding Mode Controller

Chapter 1

Introduction*

1.1 Motivation

According to the World Health Organization, 15 million people worldwide suffer a stroke every year. Nearly 6 million of them die while another 5 million are permanently disabled making stroke one of the leading causes of long-term disability. Stroke causes partial destruction of cortical tissues which because of disturbed generation of motor instructions by sensorimotor areas, results in impaired arm and hand motor functions [Prange, Jannink, Groothuis-Oudshoorn, Hermens, & IJzerman, 2006]. According to the US National Stroke Association, almost 40% of stroke survivors experience moderate to severe impairments that require special care and motor rehabilitation.

Advanced robotics has found promising applications in motor rehabilitation of stroke survivors [Fasoli, Krebs, Stein, Frontera, & Hogan, 2003; Wade & Winstein,

* A version of this chapter has been published in parts in
Butt, K., Rahman, R.A., Sepehri, N., & Filizadeh, S. (2017). Globalized and bounded Nelder-Mead algorithm with deterministic restarts for tuning controller parameters: Method and application. *Optimal Control Applications and Methods, 38(6),* 1042-1055.
Butt, K., & Sepehri, N. (2018). Model-free online tuning of controller parameters using a globalized local search algorithm. *Optimal Control Applications and Methods*, 39(5), 1750-1765.
Butt, K., & Sepehri, N. (2018). A nonlinear integral sliding surface to improve the transient response of a force-controlled pneumatic actuator with long transmission lines. Manuscript submitted for publication.

2011] which are also well accepted and tolerated by post-stroke patients [Colombo, Pisano, Mazzone, Delconte, Micera, Carrozza, Dario, & Minuco, 2007]. Functional magnetic resonance imaging (fMRI) can evaluate brain functions safely, effectively, non-invasively, and produces high-quality brain maps. Optimized fMRI methods in combination with magnetic resonance (MR) compatible controlled devices can assist therapists to quantify, monitor, and improve physical rehabilitation [Astrakas, Naqvi, Kateb, & Tzika, 2012].

Recent technological advances have resulted in devices that implement force control to develop impedance or interaction control applications for fMRI studies in the rehabilitation of motor control patients [Chapius, Gassert, Burdet, & Bleuler, 2008; Sergi, Erwin, & O'Malley, 2015; Vigaro, Sulzer, & Gassert, 2016]. However, fMRI's strong magnetic field and vulnerability to image artifacts have proven to impose a severe limitation on the selection of materials, actuators, and transducers for such devices. This makes design and control of fMRI-compatible controlled devices extremely challenging. Most of the fMRI-compatible actuation techniques can be grouped into four categories: remote manual actuation, ultrasonic/piezo motors, hydraulic, and pneumatic transmission [Elhawary, Zivanovic, Davies, & Lampérth, 2006]. Remote manual actuation offers slower procedures and lower resolutions. The ultrasonic/piezo motors are operated with high frequency electric signals which cause moderate loss of signal-to-noise ratio (SNR) and therefore do not guarantee image quality while in motion [Stoianovici, Song, Petrisor, Ursu, Mazilu, Mutener, Schar, & Patriciu, 2007; Fischer, Krieger, Iordachita, Csoma, Whitcomb, & Fichtinger, 2008]. On the other hand, both hydraulic and pneumatic actuations offer the advantage of

maintaining a high signal to noise ratio. However, the back-drivability and natural impedance because of air compressibility make pneumatic actuation favorable for force control applications [Yu, Hollnagel, Blickenstorfer, Kollias, & Riener, 2008]. Furthermore, pneumatic systems are easy to maintain as compared to hydraulic systems because they do not suffer from cavitation and hazardous fluid leakage. These factors make pneumatic actuators a favorable option to develop force-controlled applications for MRI environments. MRI-compatible force-controlled pneumatic actuators, however, require long connecting pneumatic tubes between valves and cylinders due to the commercial unavailability of MRI-compatible valves. The long pneumatic tubes between the flow controlling valve and the cylinder result in reduced and time-delayed flow rates in and out of the cylinder. This reduction and time-delay in flow through the valve necessitate an exceedingly slow system response, which negatively affects the performance of the force-controlled pneumatic actuator. Furthermore, direct cylinder pressure measurements are not possible because MRI-compatible pressure transducers are not available either. This is a serious impediment to the implementation of robust control structures that necessarily require measurements of cylinder pressures for accurate force control of a pneumatic actuator.

The above-mentioned difficulties in controlling pneumatic actuators have inspired many of the researchers to compromise this otherwise favorable actuation technique in developing controlled devices for fMRI studies. An accurate force-controlled pneumatic actuator with long transmission lines and without direct measurements of pressure will encourage researchers to avoid such a compromise. This thesis, therefore, investigates the problem of the accurate force control of a pneumatic

actuator with long transmission lines and indirect pressure measurements and proposes a suitable control scheme.

The proposed controller should outperform the available controllers in literature in an unbiased comparison to justify its use. In doing so, drawing conclusions about the capability of a controller by experimentally analyzing its performance using trial-and-error has a great deal of inaccuracy. This may lead to the unnecessary selection of complex controllers, which may require additional sensory information, and may result in the utilization of additional resources and time, and increased cost. Furthermore, tuning even simple controllers such as a Proportional-Integral-Derivative (PID) controller can be a difficult task. Attaining the best transient and steady state response using trial-and-errors heavily relies on the tuner's perception of what is the best possible response. It also makes tuning even more tedious in applications that are demanding in terms of accuracy and other performance indices. It requires extensive hands-on experience as well. Therefore, the thesis also makes an effort to develop a tuning method driven by optimization algorithm for desired performance. The method should outperform similar available methods in literature in terms of accuracy and time-efficiency. The developed tuning method should be extendible to other control applications as well.

1.2 Background

1.2.1 Force Controllers for Pneumatic Actuators

Pneumatic actuation compares favorably to the other actuation techniques for MRI-compatible force control applications. As MRI-compatible pneumatic cylinders

are available but not the valves, a pneumatic actuator always requires long transmission lines between valve and cylinder to work in MRI environment. The introduction of long transmission lines invokes dominant transmission line dynamics and results in a pneumatic system with input delay from command valve. Such an input delay, if ignored, deteriorates the performance of force-controlled pneumatic actuators. Furthermore, despite using anti-stiction cylinders or friction observers to minimize the contribution of friction towards modeling uncertainties, a pneumatic system has some other factors that make it an uncertain system. These factors include but are not limited to air compressibility, reflection and resonance in pneumatic tubes, and valve spool inertia. A sliding mode control offers a satisfactory solution to compensate for such uncertainties [Shtessel, Edwards, Fridman, & Levant, 2014]. However, the implementation of sliding mode control on pneumatic actuators requires cylinder pressure measurements to compute the dynamic function of the system. In an MRI setting, such a requirement necessitates customized solutions owing to the unavailability of MRI-compatible pressure transducers on commercial basis. Turkseven and Ueda [2017] proposed an asymptotically stable observer to estimate chamber pressures using force and piston displacement measurements. Implementation of such an observer in MRI environment requires an MRI-compatible force sensor which is not commercially available either. To avoid the use of MRI-compatible force sensor or pressure transducers, long pneumatic tubes can be employed to connect cylinder chambers to feedback pressure transducers. To facilitate the estimation of chamber pressures using available feedback pressure measurements, the model of the pneumatic tube can be approximated to be a first-order linear transfer function with time delay.

Yang, Tan, McMillan, Gullapalli, and Desai [2012] proposed such a model using system identification for 9m long transmission lines of 3.125mm internal diameter connected to closed volumes and showed that the model works well over the range of working pressures.

Richer and Hurmuzlu [2000a] proposed full and reduced order sliding mode controllers for a force-controlled pneumatic actuator based on the pneumatic model they presented in [Richer & Hurmuzlu, 2000b]. The full order controller was designed taking into account the valve dynamics as well as reduced and delayed flow because of transmission lines whereas the reduced order controller design neglected the valve dynamics and time delay induced by the valve-cylinder connecting tubes. They showed that the full order sliding mode controller outperformed the reduced order controller for a force-controlled pneumatic actuator with 2m long connecting tubes. Yu, Murr, Blickenstorfer, Kollias, and Riener [2007] also used a reduced order sliding mode force controller for fMRI-compatible pneumatic haptic interface with 4.5m long transmission lines. However, the controller exhibited oscillatory responses and valve chattering of high amplitude. The controllers proposed in both works used a conventional linear sliding surface. The controllers based on such a sliding surface have a problem of reaching phase and can only provide compensation against matched uncertainties after the sliding mode becomes operational [Hamayun, Edwards, & Alwi, 2016].

The idea of integral sliding mode control was proposed to provide compensation against matched uncertainties throughout the system response [Matthews & DeCarlo, 1988; Utkin & Shi, 1996; Wang, Lee, & Juang, 1996; Utkin, Guldner, & Shi, 1999]. Xu, Pan, and Lee [2003]; and Cao and Xu [2004] used integral sliding surfaces for

uncertain systems considering both matched and unmatched uncertainties and demonstrated that the system dynamics while on the sliding surface meet the performance specifications in the presence of matched uncertainties. Castanos and Fridman [2006] demonstrated that the effect of unmatched uncertainties can also be minimized by the suitable choice of an integral sliding surface. Though the use of integral sliding mode effectively rejects disturbances and matched uncertainties right from the beginning of the response, it may result in a compromised transient response if the initial system errors are very large. The system may also become vulnerable in terms of closed-loop stability due to the integral wind-up phenomenon in the presence of control input constraints [Gao & Liao, 2013].

Settling time and overshoot are the two important indices of closed-loop transient performance and a trade-off always exists between them in the presence of the conventional linear sliding surface. To improve both the indices simultaneously, the idea of variable damping ratio of dominant closed-loop poles using a nonlinear sliding surface is one possible solution. Such an idea was first introduced by Lin, Pachter, and Banda [1998] for second-order systems with state-feedback control, and it was further extended to general higher order SISO and MIMO systems by Turner, Postlethwaite, and Walker [2000]; Chen, Lee, Peng, and Venkataraman [2003]; Venkataraman, Peng, and Chen [2003]; and Turner and Postlethwaite [2004] for state-feedback and output-feedback based control laws. Bandyopadhyay and Fulwani [2009] proposed a nonlinear sliding surface based on variable damping ratio to achieve improved performance and robustness for the discrete plant. In another work, Bandyopadhyay, Deepak, Postlethwaithe, and Turner [2010] showed improvement in the transient response of a

discrete-time uncertain SISO linear system with input delay using the nonlinear sliding surface. Abd El Khalick Mohammad, Uchiyama, and Sano [2015] used a nonlinear sliding surface to induce a change in damping ratio from its initial low value to the final high value as the contour error changes from high value to small value and vice versa to improve the machining accuracy of biaxial feed-drive systems. Ripamonti, Orsini, and Resta [2017] applied a nonlinear parabolic sliding surface to rotate the links of a three-link flexible manipulator quickly with reduced vibrations.

To the best of our knowledge, the nonlinear sliding surfaces available in literature have never been applied to the force control of pneumatic actuators exhibiting uncertainties and input delays. Furthermore, the available nonlinear sliding surfaces have been constructed by adding nonlinear functions to the conventional linear sliding surfaces. Such nonlinear sliding surfaces have the problem of reaching phase. Consequently, the sliding mode controllers designed using them do not provide robustness against matched uncertainties until the sliding mode is established.

1.2.2 Tuning of Controller Parameters

The performance of any control application largely depends upon the suitable controller structure and the careful selection of controller parameters. That is why the considerable effort has been made by researchers to come up with different methods to tune controller parameters. These methods range from trial-and-error to more sophisticated ones such as using neural networks, heuristics, and meta-heuristics. Each method has advantages over the others in different control environments and applications.

The most widely used tuning method is probably trial-and-error. Such a method may sometimes give fair results but, due to heavy reliance on the tuner's perception of what is the best possible response, may provide inaccurate conclusions about the capability of the controller in demanding control applications.

Model-based offline tuning methods using heuristics and meta-heuristics have been reported in some studies [Padula & Visioli, 2011; Kim, 2011; Chiha, Liouane, Borne, 2012; Reynoso-Meza, Garcia-Nieto, Sanchis, & Blasco, 2013]. These methods offer great advantages for tuning in applications where a sufficiently adequate model for a range of operating conditions is known, and the iterative system runs for online tuning are time-consuming or very expensive. However, a multiplicity of local solutions has inspired much of this work to use population-based algorithms which often have a prohibitively high numerical cost. Furthermore, the evolutionary algorithms such as genetic algorithms may sometimes converge to arbitrary points when the optimization problem does not provide an easy ascent to global optimum [Wolpert & Macready, 1995]. Also, the decision of selecting an evolutionary algorithm for an optimization problem depends upon the space to be searched for an optimal solution. If that space is well-understood, the use of evolutionary algorithms is generally computationally less efficient [Forrest & Mitchell, 1993]. Luersen and Le Riche [2004] proposed a fixed cost local search optimization which sequentially becomes global. It achieved globalization by probabilistic restarts of the Nelder-Mead's algorithm using spatial probability. The method is particularly useful in tackling multimodal, discontinuous, and constrained optimization problems. But due to the probabilistic nature of restarts, the algorithm exhibits varying accuracy levels when running multiple times for same optimization

problem. With respect to tuning controller parameters, this is not desirable especially in demanding control applications.

The performance of any optimization algorithm in the model-based tuning of controller parameters depends heavily on the adequacy of the mathematical model and the identification of bounds on decision variables within which the sufficient adequacy of model exists. In many applications, un-modeled uncertainties may pose a serious challenge in obtaining sufficiently adequate models. Also, the end-user may find it difficult to accept the essential requirement of knowing the sufficiently adequate model for tuning the controller parameters.

It is reasonable to believe that an improvement in the performance of heuristics or metaheuristics for tuning is expected if they rely on measurements coming directly from actual physical systems and not just their mathematical models. Model-free online tuning methods like extremum seeking [Killingsworth & Krstic, 2006], discrete Fourier transform processing [Fnaiech, Khadraoui, Nounou, Nounou, Guzinski, Abu-Rub, Datta, & Bhattacharyya, 2014], stable adaptation mechanism [Boubakir, Labiod, & Boudjema, 2012], binary search gain-tuning [Tursini, Parasiliti, & Daqing, 2002], chaotic particle swarm approach [dos Santos Coelho & Coelho, 2009], and self-gain tuning method using neural networks [Le, Kang, Suh, & Ro, 2013] have been proposed; however, their effectiveness has mostly been examined for tuning of PID controllers. Furthermore, the basic deterministic extremum seeking algorithm uses sinusoidal perturbations for real-time online tuning. The smaller the amplitude of sinusoidal perturbation, the greater the probability of getting stuck at the local minimum [Liu & Krstic, 2012]. Also, the performance of extremum seeking greatly relies on the cleaner

gradient estimation which needs larger perturbation frequency [Liu & Krstic, 2012]. Therefore, in applications having slower dynamics and amplitude of controlled variable constrained by smaller bounds like pneumatic control systems, the performance of the extremum-seeking algorithm is limited. Oliveira JB, Boaventura-Cunha, Oliveira PM, and Freire [2014] presented online tuning of the sliding mode generalized predictive controller for Van de Vusse reaction system and first-order-plus-dead-time discrete transfer functions commonly associated with chemical processes having extremely slower dynamics. They proposed to tune the continuous component of control law using quadratic programming and the discontinuous component using particle swarm optimization. Particle Swarm Optimization, being a population-based algorithm, has a high numerical cost and online tuning using it may require many iterative system's runs to converge to a solution, which for some applications may be exceedingly time-consuming or simply unaffordable.

1.3 Research Objectives

On the basis of literature reviewed above, this thesis defines the following objectives:

1. To develop a novel globalized local search, multimodal optimization algorithm which should have a lower numerical cost and a greater probability of finding global minimum as compared to existing evolutionary, swarm, and other globalized local search multimodal optimization algorithms.
2. To effectively apply the proposed algorithm for model-based offline and model-free online tuning of robust nonlinear sliding mode controller for a pneumatic control

application with performance already reported after rigorous trial-and-error tuning in an earlier publication. The proposed algorithm-driven offline and online controller tuning should improve the system's performance by a considerable margin.

3. To propose and examine a novel nonlinear integral sliding surface for an improved transient response of a force-controlled pneumatic actuator with long transmission lines. The proposed sliding surface should not have a reaching phase despite initial errors and multiple steps in the desired trajectory and, therefore, should guarantee robustness against matched uncertainties throughout the system response.
4. To design and implement a full order sliding mode force controller based on the proposed nonlinear integral sliding surface on a pneumatic actuator with long transmission lines subjected to an external human force. To facilitate implementation of sliding mode control in MRI environment without using MRI-compatible force sensor and pressure transducers, a suitable method for indirect measurements of chamber pressures should be used.
5. To implement the proposed algorithm driven tuning on the proposed controller to optimize its parameters for the desired system response. The proposed force controller should outperform the one using the linear integral sliding surface in an unbiased comparison to justify its use.

1.4 Thesis Organization

Chapter 2 presents a globalized bounded Nelder-Mead algorithm with deterministic restarts and a linearly growing memory vector and compares it against the

evolutionary, the swarm and the other globalized local search optimization algorithms. Chapter 3 applies the proposed algorithm for the model-based offline tuning of sliding mode controller parameters of a position controlled pneumatic actuator with previously reported performance and shows its effectiveness. Chapter 4 presents a model-free online tuning method based on the proposed algorithm for optimizing the sliding mode controller parameters of the same pneumatic actuator. Chapter 5 describes the schematic diagram of a force-controlled pneumatic actuator with long transmission lines and indirect pressure measurements and derives its dynamic equations. The chapter also proposes a nonlinear integral sliding surface and designs a full order sliding mode force controller for the actuator using the surface. A full order sliding mode control law based on a linear integral sliding surface for the actuator is also derived in the chapter for performance comparison. This chapter establishes the asymptotic stability of the force controller having the proposed sliding surface as well. Chapter 6 evaluates the performance of force controller built upon the proposed sliding surface and compares its performance against the one with a linear integral sliding surface using simulation and experiments. Chapter 7 presents the contributions made by the research as well as some recommendations for future work.

Chapter 2

A Low-cost Multimodal Optimization Algorithm†

2.1 Description of Optimization Algorithm

This chapter proposes a novel low-cost multimodal optimization algorithm. The proposed algorithm globalizes the Guin augmented variant of Nelder-Mead's algorithm sequentially by deterministic restarts, linearly growing memory vector and moving initial simplex. The algorithm exploits the simplicity of search space formed by simple bounds on design variables for deterministic restarts. For better understanding, the Guin augmented variant of Nelder-Mead's algorithm is described in Section 2.1.1 before explaining the proposed deterministic restarts with moving initial simplex in Section 2.1.2.

2.1.1 Guin Augmented Variant of Nelder-Mead's Algorithm

The Nelder-Mead's downhill simplex algorithm [Nelder & Mead, 1965] is a non-linear, derivative-free, unconstrained, local search optimization algorithm. It uses

† A version of this chapter has been published in Butt, K., Rahman, R.A., Sepehri, N., & Filizadeh, S. (2017). Globalized and bounded Nelder-Mead algorithm with deterministic restarts for tuning controller parameters: Method and application. *Optimal Control Applications and Methods, 38(6),* 1042-1055.

$n+1$ vertices $x_1, x_2, \cdots, x_{n+1}$ as initial simplex where n is the number of parameters to be optimized for minimization of the objective function. The possible variant of this algorithm uses reflection, expansion, contraction, and shrinkage to find local minimizer as follows:

1. The algorithm takes the centroid of all points x_0 except x_{n+1} where$f(x_1) \leq f(x_2) \leq \cdots \leq f(x_n) \leq f(x_{n+1})$.
2. It computes the reflected point

   $x_r = x_0 + \alpha(x_0 - x_{n+1})$

   where α is the reflection coefficient.
3. If the reflected point is such that $f(x_r) \leq f(x_{n+1})$, the algorithm computes the expanded point

   $x_e = x_0 + \gamma(x_0 - x_{n+1})$

   where γ is the expansion coefficient.

   If the expanded point is such that $f(x_e) \leq f(x_r)$, the algorithm replaces x_{n+1} by x_e and makes a new simplex. Otherwise, it replaces x_{n+1} by x_r and makes a new simplex.
4. If $f(x_r) > f(x_{n+1})$, the algorithm computes the contracted points

   $x_c = x_0 \pm \rho(x_{n+1} - x_0)$

   where ρ is the contraction coefficient.

   If the better of contracted points is such that $f(x_c) \leq f(x_{n+1})$, the algorithm replaces x_{n+1} by x_c and makes a new simplex.
5. If $f(x_c) > f(x_{n+1})$, the algorithm replaces all points of simplex except x_1 by

   $x_i = x_1 + \sigma(x_i - x_1), \qquad i = \{2, \cdots, n+1\}$

where σ is the shrink coefficient.

For the algorithm to function, the values of reflection, expansion, contraction and shrink coefficients should satisfy the constraints such that $\alpha > 0$, $\gamma > 1$, $\gamma > \alpha$, $0 < \rho < 1$, $0 < \sigma < 1$ [Singer & Nelder, 2009].

Nelder-Mead's algorithm terminates when at least one of small simplex convergence test, function value convergence test, no convergence test becomes true.

To put bounds on optimal gain search by Nelder-Mead's algorithm, variations to the original algorithm are required. Numerous variations have been proposed for this purpose, among which the Guin method [Guin, 1968] stands out due to simplicity and effectiveness to introduce implicit constraints, and easy implementation. The Guin method successfully embeds such constraints into Nelder-Mead's algorithm though it has a probability to fail in rare exceptions especially in case of minimization problems of dimensions greater than four [Floc'h, 2012]. This method, in case of a trial point lying outside the bounds, keeps on taking the midpoints between the centroid and the trial point until the trial point starts respecting the bounds.

2.1.2 Proposed Deterministic Restarts and Moving Initial Simplex

To achieve globalization within the n-dimensional search space formed by simple bounds on design variables, the proposed algorithm identifies the region of interest (**S**) for optimal parameters search as follows:

$$\mathbf{S} = \begin{bmatrix} \mathbf{V_1} \\ \mathbf{V_2} \\ \vdots \\ \mathbf{V_{2^n}} \end{bmatrix} \tag{1}$$

where $\mathbf{V_1}, \mathbf{V_2}, \dots, \mathbf{V_{2^n}}$ are matrices of order $1 \times \mathrm{n}$ and are vertices of n-dimensional search space.

The algorithm defines an allowable number of restarts R. The initial simplex **IS** for the 1st run ($\mathrm{r} = 1$) of Guin augmented variant of Nelder-Mead's algorithm is formed as follows:

$$\mathbf{IS} = (\mathbf{X_c}^{\mathbf{T}} \cdot \mathbf{J_{1,n+1}})^{\mathbf{T}} + \begin{bmatrix} 0 & 0 & 0 \cdots 0 & 0 \\ \propto_1 & 0 & 0 \cdots 0 & 0 \\ 0 & \propto_2 & 0 \cdots 0 & 0 \\ & & \vdots & \\ 0 & 0 & 0 \cdots 0 & \propto_n \end{bmatrix} \tag{2}$$

where $\mathbf{X_c}$ is the centroid of search space and **J** is a matrix consisting of ones only with the subscript showing its order. Also,

$$\propto_i = \begin{cases} -\dfrac{x_{i_{max}} - x_{i_{min}}}{\beta}, & i = 1 \\ \dfrac{x_{i_{max}} - x_{i_{min}}}{\beta}, & i \in \{2,3, \dots, n\} \end{cases} \tag{3}$$

In (3), $x_{i_{max}}$ and $x_{i_{min}}$ are the bounds on the ith parameter to be optimized. $\beta \in \{4.9,5\}$ is the initial simplex size coefficient and determines the size of the initial simplex.

Local minimizer $\mathbf{X_0}$ found by each run ($1 \leq \mathrm{r} < R$) of Guin augmented variant of Nelder-Mead's algorithm is used for constructing initial simplex for the succeeding run as follows:

In case of the centroid of search space lying at the origin, local minimizer $\mathbf{X_0}$ is projected onto 2^n points **P** within the search space.

$$\mathbf{P} = 0.5\mathbf{S} - 0.5(\mathbf{X_0}^{\mathbf{T}} \cdot \mathbf{J_{1,2^n}})^{\mathbf{T}} \tag{4}$$

Equation (4) may cause a violation of bounds on parameter search by projected points if the centroid of search space does not lie at the origin. This makes initial simplex to lie outside the search space resulting in failure of bounds on optimized parameters search.

To solve this problem, the search space is translationally moved to make centroid lie at the origin.

$$\widehat{\mathbf{X}}_{\mathbf{c}} = \mathbf{X}_{\mathbf{c}} + [a_1 \quad a_2 \quad \dots \quad a_n] \tag{5}$$

In (5) $a_1, a_2, \dots, a_n$ are the respective distances between centroid and origin along respective axes of n-dimensional search space.

With new centroid $\widehat{\mathbf{X}}_{\mathbf{c}}$, the search space becomes

$$\hat{\mathbf{S}} = \begin{bmatrix} \widehat{\mathbf{V}}_{\mathbf{1}} \\ \widehat{\mathbf{V}}_{\mathbf{2}} \\ \vdots \\ \widehat{\mathbf{V}}_{\mathbf{2^n}} \end{bmatrix} \tag{6}$$

where

$$\widehat{\mathbf{V}}_{\mathbf{i}} = \mathbf{V}_{\mathbf{i}} + [a_1 \quad a_2 \quad \dots \quad a_n], \qquad i \in \{1,2, \dots, 2^n\} \tag{7}$$

Local minimizer $\mathbf{X_0}$ found in the preceding run becomes $\widehat{\mathbf{X}}_{\mathbf{0}}$.

$$\widehat{\mathbf{X}}_{\mathbf{0}} = \mathbf{X_0} + [a_1 \quad a_2 \quad \dots \quad a_n] \tag{8}$$

Local minimizer is projected onto 2^n points within moved search space as given in (9).

$$\widehat{\mathbf{P}} = 0.5\hat{\mathbf{S}} - 0.5(\widehat{\mathbf{X}}_{\mathbf{0}}{}^{\mathbf{T}} \cdot \mathbf{J}_{\mathbf{1,2^n}})^{\mathbf{T}} \tag{9}$$

where $\widehat{\mathbf{P}}$ is a matrix of order $2^n \times n$.

The projected points are then moved back to the original search space as given in (10).

$$\mathbf{P} = \widehat{\mathbf{P}} - \left(\begin{bmatrix} a_1 \\ a_2 \\ \vdots \\ a_n \end{bmatrix} . \mathbf{J_{1,2^n}} \right)^{\mathbf{T}} \tag{10}$$

The objective function is evaluated on all of these points. Out of these projected points, one is designated as $\mathbf{P_0}$ which becomes an element of linearly growing memory vector **M** and is used for constructing initial simplex for the succeeding run according to following criteria:

For $r = 2$, the one having the minimum value of objective function amongst all projected points is selected as $\mathbf{P_0}$.

For $2 < r \leq R$, the one having the minimum value of objective function amongst all those projected points which are not elements of existing memory vector **M**, is selected as $\mathbf{P_0}$.

This helps algorithm avoid getting stuck at one local minimizer. To construct initial simplex for all succeeding runs, Eq. (2) is used with $\mathbf{X_c}$ replaced by $\mathbf{P_0}$. To make initial simplex respect the bounds, $\propto_i$ is taken as follows for all succeeding runs:

$$\propto_i = \begin{cases} -\dfrac{x_{i_{max}} - x_{i_{min}}}{\beta} & \mathbf{P_0} \text{ exceeds } \mathbf{X_c} \text{ in the ith dimension.} \\ \dfrac{x_{i_{max}} - x_{i_{min}}}{\beta} & \mathbf{X_c} \text{ equals or exceeds } \mathbf{P_0} \text{ in the ith dimension.} \end{cases} \tag{11}$$

This proposed multimodal optimization algorithm keeps on running until the minimum found is less than or equal to the desired minimum. Otherwise, the algorithm terminates when all projected points already exist in memory vector or the defined number of restarts has been executed. In this case, the algorithm selects the best local minimum found so far as a global minimum.

2.2 Performance Evaluation of Proposed Algorithm

The performance of the algorithm in terms of globalization, accuracy and numerical cost has been evaluated using minimization of ten complex multimodal benchmark functions having many local minima within search space. In multimodal optimization, one is not interested primarily in global minimum but rather in minima having values less than a certain value which in the thesis has been defined as the desired minimum. For evaluation of the performance of the algorithm in terms of globalization, the desired minimum has been kept equal to the global minimum with a tolerance of 0.001. The benchmark functions are shown in Table 2.1.

TABLE 2.1 BENCHMARK FUNCTIONS

Function	**Mathematical Form**
Eggholder	$f(x,y) = -(y+47)sin\left(\sqrt{\left\lvert y+\frac{x}{2}+47\right\rvert}\right) - xsin(\sqrt{\lvert x-(y+47\rvert})$
Drop-wave	$f(x,y) = -\frac{1+cos(12\sqrt{x^2+y^2})}{0.5(x^2+y^2)+2}$
Bukin N.6	$f(x,y) = 100\sqrt{\lvert y-0.01x^2\rvert} + 0.01\lvert x+10\rvert$
Holder Table	$f(x,y) = -\left\lvert sin(x)cos(y)exp\left(\left\lvert 1-\frac{\sqrt{x^2+y^2}}{\pi}\right\rvert\right)\right\rvert$
Schwefel	$f(x,y) = 837.9658 - (xsin\sqrt{\lvert x\rvert} + ysin\sqrt{\lvert y\rvert})$
Shubert	$f(x,y) = \left(\sum_{i=1}^{5} icos\big((i+1)x+i\big)\right)\left(\sum_{i=1}^{5} icos\big((i+1)y+i\big)\right)$
Levy N.13	$f(x,y) = sin^2(3\pi x) + (x-1)^2[1+sin^2(3\pi y)] + (y-1)^2[1+sin^2(2\pi y)]$
Ackley	$f(x,y) = -20\exp\left(-0.2\sqrt{\frac{1}{2}(x^2+y^2)}\right) - \exp\left(\frac{1}{2}(\cos(2\pi x)+\cos(2\pi y))\right) + 20 + \exp(1)$
Beale	$f(x,y) = (1.5-x+xy)^2 + (2.25-x+xy^2)^2 + (2.625-x+xy^3)^2$
Goldstein-Price	$f(x,y) = [1+(x+y+1)^2(19-14x+3x^2-14y+6xy+3y^2)]$ $[30+(2x-3y)^2(18-32x+12x^2+48y-36xy+27y^2)]$

The proposed algorithm with deterministic restarts performs satisfactorily on ten complex multimodal optimization benchmarks having many local minima. One of these

functions is shown in Figure 2.1. It achieves the global minimum in all cases. The details are given in Table 2.2.

TABLE 2.2 PERFORMANCE OF PROPOSED ALGORITHM ON MINIMIZATION OF BENCHMARK FUNCTIONS

Function	**Global Minimum**	**Search Space**	**Minimum Found by Algorithm**	**Function Evaluations Used**
Eggholder	-959.6407	$x \in [-512,512]$, $y \in [-512,512]$	$f(512,404.2319) = -959.6407$	1036
Drop-wave	-1	$x \in [-5.12,5.12]$, $y \in [-5.12,5.12]$	$f(0,0) = -1$	365
Bukin N.6	0	$x \in [-15,-5]$, $y \in [-3,3]$	$f(-10.02,1.003) = 0.00017$	596
Holder Table	-19.2085	$x \in [-10,10]$, $y \in [-10,10]$	$f(-8.055,-9.664) = -19.2085$	265
Schwefel	0	$x \in [-500,500]$, $y \in [-500,500]$	$f(420.9688,420.9688) = 0.000025455$	324
Shubert	-186.7309	$x \in [-10,10]$, $y \in [-10,10]$	$f(-1.4251,-0.8003) = -186.7309$	327
Levy N.13	0	$x \in [-10,10]$, $y \in [-10,10]$	$f(1,1) = 0$	269
Ackley	0	$x \in [-32.768,32.768]$, $y \in [-32.768,32.768]$	$f(0,0) = 0$	591
Beale	0	$x \in [-4.5,4.5]$, $y \in [-4.5,4.5]$	$f(3,0.5) = 0$	392
Goldstein-Price	3	$x \in [-2,2]$, $y \in [-2,2]$	$f(0,-1) = 3$	259

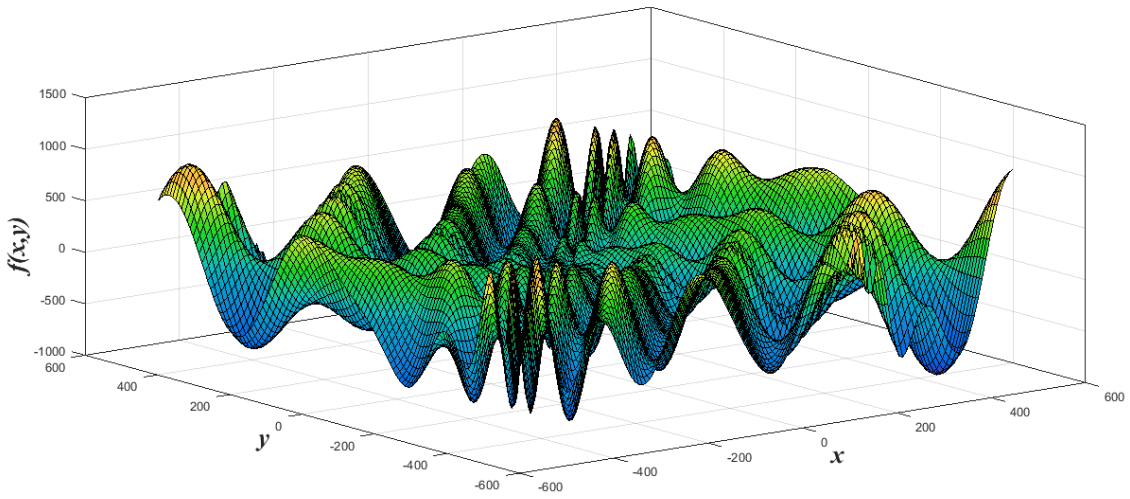

Figure 2.1 Eggholder function

The proposed algorithm tries to avoid the vicinity of already found local minimum using Eqs (4-11) and a linearly growing memory vector without violating the bounds of search space. This prevents the algorithm from getting stuck to the same local minimum and enables it to find the new one. An example is shown in Figure 2.2 in which the proposed algorithm is minimizing the complex multimodal eggholder function to achieve the global minimum. It shows that the algorithm converges to the global minimum using 4 deterministic restarts of Nelder-Mead with moving initial simplex and in all of these four restarts it converges to a different local minimum.

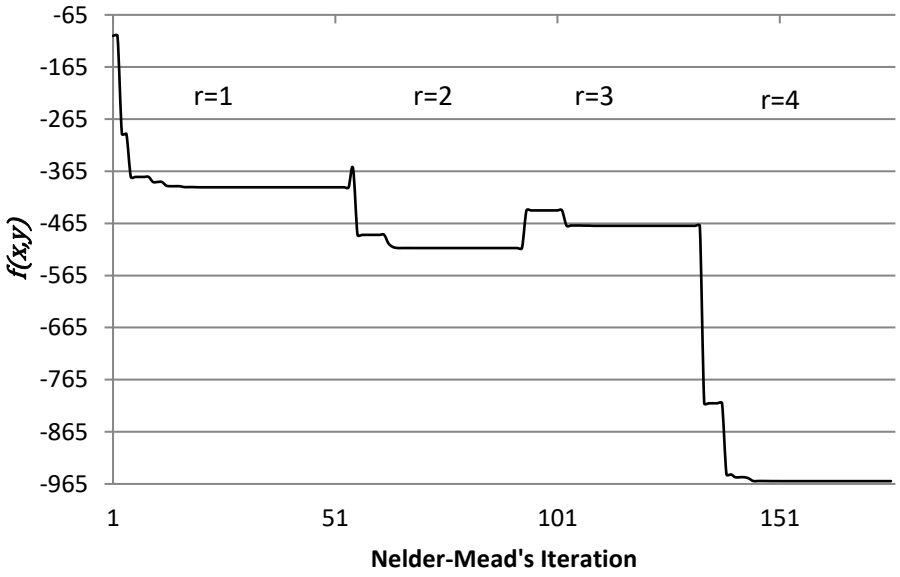

Figure 2.2 Convergence characteristic of proposed algorithm while minimizing the eggholder function

To compare the performance of the algorithm in globalization and numerical cost, Luersen's globalized bounded Nelder-Mead (GBNM) with probabilistic restarts, genetic algorithm (GA) with elitism, and two variants of particle swarm optimization (PSO) i.e. with adaptive inertia weight, and linearly decreasing inertia weight, have been used. The proposed algorithm, because of deterministic restarts, converges to the

global minimum with the same accuracy if run with same algorithm parameters on the same problem multiple times. Luersen's GBNM, GA with elitism and both variants of PSO lack such consistency as shown in Table 2.3. However, variants of PSO compare favorably against GA and Luersen's GBNM in terms of probability of finding global minimum in most of the optimization benchmarks. This encourages the use of PSO with multiple swarm runs to see if they can achieve 100% probability of finding global minimum in case of all multimodal optimization benchmarks used in this thesis. PSO with linearly decreasing inertia weight and multiple swarm runs achieves 100% success in finding global minima but the numerical cost for doing so is higher as compared to the proposed algorithm, as shown in Table 2.4. For the comparisons shown in Tables 2.3 and 2.4, algorithm parameters given in Table 2.5 have been used. All algorithms have been coded in MATLAB scripts.

TABLE 2.3 PERFORMANCE COMPARISON BETWEEN LUERSEN'S GBNM, GA, PSO AND PROPOSED ALGORITHM

Function	**No. of times global minimum with a tolerance of 0.001 was found over 1000 runs**						
	Luersen's GBNM	**GA with Elitism**	**PSO with Adaptive Inertia Weight**	**PSO with Linearly Decreasing Inertia Weight**	**PSO with Adaptive Inertia Weight and Multiple Swarm Runs**	**PSO with Linearly Decreasing Inertia Weight and Multiple Swarm Runs**	**Proposed Algorithm**
Eggholder	184	0	705	556	1000	1000	1000
Drop-wave	38	105	463	588	1000	1000	1000
Bukin N.6	210	0	5	304	46	1000	1000
Holder Table	766	0	893	464	1000	1000	1000
Schwefel	671	0	599	603	1000	1000	1000
Shubert	646	172	829	477	1000	1000	1000
Levy N.13	982	661	993	792	1000	1000	1000
Ackley	980	995	998	678	1000	1000	1000
Beale	1000	734	997	950	1000	1000	1000
Goldstein-Price	1000	612	999	957	1000	1000	1000

TABLE 2.4 PERFORMANCE COMPARISON BETWEEN PSO AND PROPOSED ALGORITHM IN TERMS OF NUMERICAL COST

Functions	**Function evaluations used to reach global minimum with a tolerance of 0.001**	
	PSO with Linearly Decreasing Inertia Weight and Multiple Swarm Runs	**Proposed Algorithm**
Eggholder	5920	1036
Drop-wave	4900	365
Bukin N.6	18820	596
Holder Table	4280	265
Schwefel	9040	324
Shubert	12960	327
Levy N.13	10300	269
Ackley	13560	591
Beale	6020	392
Goldstein-Price	8820	259

As shown in Table 2.3, the genetic algorithm performs poorly on some of the multimodal optimization benchmarks. This is expected as the traditional GA with both mutation and crossover rates are adversely affected by the multimodality of the problem [Kennedy & Spears, 1998]. Furthermore, the performance of the genetic algorithm relies substantially on the tuning of its three main algorithm operators; population size, crossover rate, and mutation rate. Values of these operators are often problem specific for best performance and generalization is not possible which makes use of the genetic algorithm for global optimization somewhat challenging. On the other hand, the proposed algorithm needs only one operator to be tuned and that is the initial simplex size coefficient (β). The proposed algorithm achieves globalization with the small numerical cost for all multimodal optimization benchmarks shown in Table 2.1 with $\beta = 4.9$ except Bukin N.6 for which β is found to be 5 for globalization. This shows that the proposed algorithm provides sufficient generalization for selecting the proper value of its operator β over a range of multimodal optimization problems for globalization with small numerical cost. This makes use of proposed algorithm easier

than the genetic algorithm in handling multimodal optimization problems with simple bounds for globalization.

TABLE 2.5 ALGORITHM PARAMETERS

Parameter Description	Value
For Luersen's GBNM and Proposed Algorithm	
Number of restarts allowed	12
Maximum function evaluations	2500
Reflection coefficient	1
Expansion coefficient	2
Contraction coefficient	0.5
Shrink coefficient	0.5
Small simplex convergence test coefficient	5e-07
Function value convergence test coefficient	1e-09
No convergence test coefficient (function evaluations)	600
For GA with Elitism	
Population size	200
Elite count	2
Generations	100
Crossover rate	0.8
Mutation rate	0.01
Function tolerance	1e-6
Stall generations limit*	50
For PSO with Linearly Decreasing Inertia Weight	
Population size	20
Acceleration factors (C_1, C_2)	2
Max. inertia weight	0.9
Min inertia weight	0.4
Function tolerance	1e-6
Maximum iterations	1000
Stall iterations limit**	500
Velocity clamped	No
Maximum swarm runs allowed in case of multiple swarm runs	12
For PSO with Adaptive Inertia Weight	
Population size	20
Acceleration factors (C_1, C_2)	2
Max. inertia weight	1.1
Min inertia weight	0.1
Function tolerance	1e-6
Maximum iterations	1000
Stall iterations limit**	500
Velocity clamped	No
Maximum swarm runs allowed in case of multiple swarm runs	12

* It is one of the stopping conditions or termination criteria for GA. The algorithm stops when the average relative change in the best fitness function value over maximum stall generations is less than the function tolerance of 1e-6.

** It is one of the stopping conditions or termination criteria for PSO. The algorithm stops when the average relative change in the best fitness function value over maximum stall iterations is less than the function tolerance of 1e-6.

The proposed algorithm outperforms Luersen's GBNM in terms of globalization and repeatability of performance in multimodal optimization problems with simple bounds. In doing so, the proposed algorithm exploits the simplicity of search space formed by simple bounds on design variables and absence of linear or nonlinear constraint inequalities. The effectiveness of the proposed algorithm shows that the simplicity of search space can be used advantageously in handling multimodal optimization problems with substantially increased chances of finding the global optimum and low numerical cost.

2.3 Summary

A globalized and bounded Nelder-Mead algorithm with deterministic restarts and a linearly growing memory vector was proposed. The proposed algorithm achieved globalization sequentially by deterministic restarts and was useful where evolutionary or swarm optimization methods could not be afforded. The algorithm performed very well on minimization of complex multimodal functions with many local minima. Deterministic restarts allowed consistent performance of the algorithm in achieving globalization with lower numerical cost. The algorithm compared favorably against Luersen's GBNM, genetic algorithm, and particle swarm optimization. Consistency in performance and lower numerical cost in solving multimodal optimization problems made the algorithm an excellent choice for time-efficient controller tuning, which also forms a class of multimodal optimization problems.

Chapter 3

Model-based Offline Tuning of Sliding Mode Controller Parameters[‡]

The multimodal optimization algorithm proposed in Chapter 2 is now used for model-based offline tuning of sliding mode controller parameters for a nonlinear system. The system is a servo pneumatic position control application with 4-quadrant loading and its performance has been reported in an earlier published work. The system benefitted from the earlier effort of tuning using trial-and-error made over the years. It has been chosen to find out if the proposed model-based offline tuning holds a significant advantage.

3.1 Servo-Pneumatic Position Control System

The servo-pneumatic position control system is shown in Figure 3.1. The schematic diagram of this system is shown in Figure 3.2. It consists of a 5/3 proportional valve with the pneumatic cylinder as an actuator. The pneumatic cylinder is double-acting single-rod with piston stroke length of 30.3 cm. The piston has a

[‡] A version of this chapter has been published in Butt, K., Rahman, R.A., Sepehri, N., & Filizadeh, S. (2017). Globalized and bounded Nelder-Mead algorithm with deterministic restarts for tuning controller parameters: Method and application. *Optimal Control Applications and Methods, 38(6),* 1042-1055.

diameter of 4cm. The cylinder is coupled with a loading configuration, in which load assists and resists the piston movement alternatingly. For measurement of actuator position, a rotary optical encoder has been attached at the end of connecting beam. Pressure is being recorded by two pressure transducers mounted on each side of the cylinder's chambers. Pressure has been regulated using pressure regulator while pressure fluctuations have been minimized by including an air reservoir into the system. Real-time data acquisition has been ensured by using data acquisition board that works as an interface between the test rig and a target PC. The target PC has been connected to a host PC (experimenter's workstation) through TCP/IP communication protocol. Real-time control software QUARC with QNX Neutrino real-time operating system has been used to execute control algorithm downloaded on target PC. The QUARC has been interfaced with MATLAB Simulink to provide a graphical user interface for the data flow through the data acquisition board.

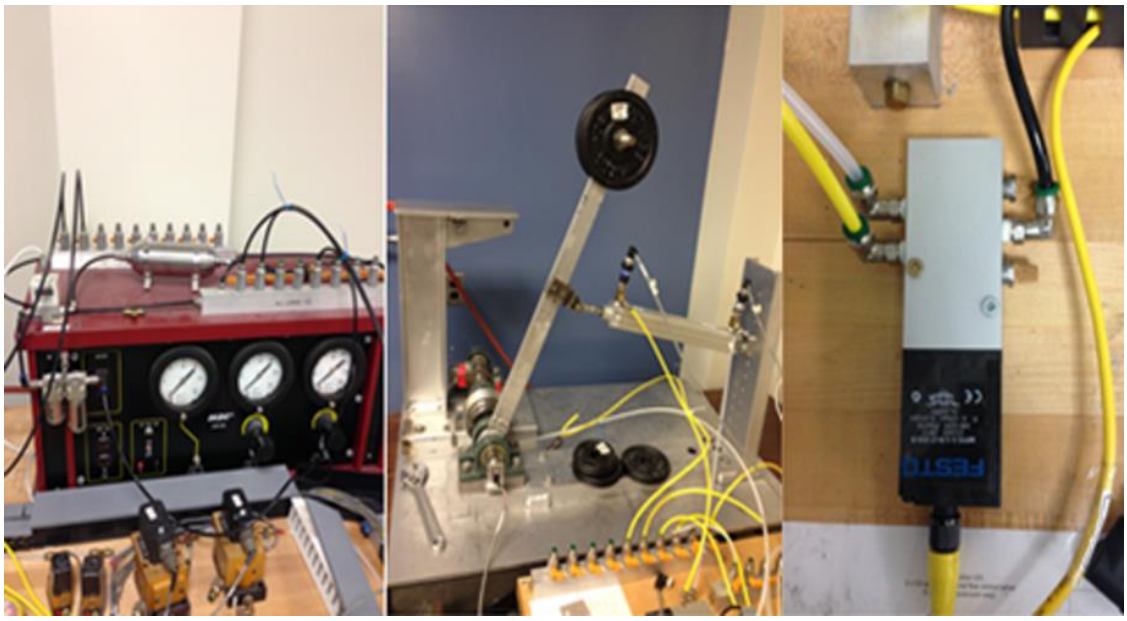

Figure 3.1 Experimental setup

1. Pneumatic cylinder (FESTO DNC-40-303-PPV-A)
2. Position encoder (BOURNS ENSIJ-B28-L00256)
3. 5/3-way proportional directional valve (FESTO MYPE-5-1/8-LF-010-B)
4. Pressure transducer (ASHCROFT T27M0210E200#G)
5. Pressure regulator (SMC ITV1050-31N2CS4-Q)
6. Host PC (MICROSOFT Window operating system)
7. Target PC (QNX Neutrino real-time operating system)
8. DAQ board (QUANSER Q8)

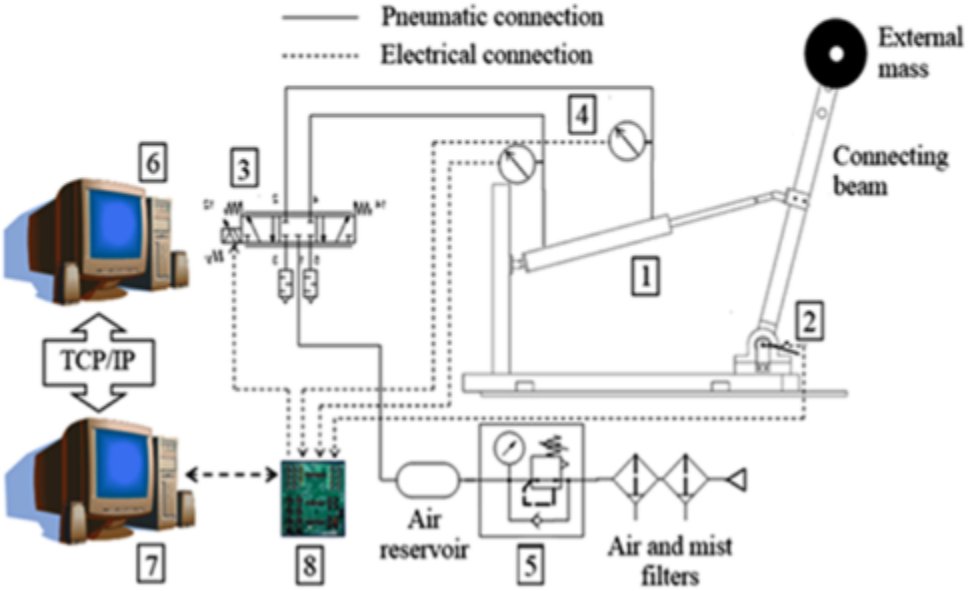

Figure 3.2 Schematic of the experimental setup

3.2 Pneumatic System Model and Control Law

The dynamic equations and the sliding mode control law of the control system have been derived in detail in [Ramhuzaini, He, & Sepehri, 2016] adopting the methodology presented in [Shen, 2010]. Only the final derivations are shown here.

3.2.1 System Dynamics

The state space representation of the system is

$$\dot{x_p} = v_p \tag{12}$$

$$\dot{v_p} = \frac{1}{M}\left(P_1 A_1 - P_2 A_2 - F_f - F_L\right) \tag{13}$$

$$\dot{P_1} = \frac{\gamma RT}{V_{01} + A_1\left(\frac{L}{2} + x_p\right)}\dot{m}_1 - \alpha\frac{\gamma P_1 A_1 v_p}{V_{01} + A_1\left(\frac{L}{2} + x_p\right)} \tag{14}$$

$$\dot{P_2} = \frac{\gamma RT}{V_{02} + A_2\left(\frac{L}{2} - x_p\right)}\dot{m}_2 + \alpha\frac{\gamma P_2 A_2 v_p}{V_{02} + A_2\left(\frac{L}{2} - x_p\right)} \tag{15}$$

$$\dot{m}_1 = A_v \Psi_1(P_u, P_d) \tag{16}$$

$$\dot{m}_2 = -A_v \Psi_2(P_u, P_d) \tag{17}$$

where x_p and v_p are the position and velocity of the actuator respectively. M is the total inertial mass of external load, connecting beam, piston and connecting rod. A_1 and A_2 are the piston effective areas in chambers 1 and 2 of the actuator while P_1 and P_2 are the pressures in chambers 1 and 2. F_f represents friction and F_L is the external load. R is for universal gas constant, γ the ratio of specific heat, and T stands for temperature. V_{01} and V_{02} are the volumes of compressed air trapped in pneumatic tubes between valves and cylinder chambers. L symbolizes length of the piston stroke, and $\dot{m}_1$ and $\dot{m}_2$ are the mass flow rates of compressed air dependent upon valve orifice area, A_v. ψ_1 and ψ_2 decide whether the mass flow rate is in chocked or un-chocked region.

The state space model of the servo pneumatic system can be written in the following canonical form which represents the relationship of the valve orifice area, A_v to the actuator position, x_p.

$$\dddot{x_p} = f(x) + b(x)A_v \tag{18}$$

where $f(x)$ is the dynamic function of the system and is given by:

$$f(x) = -\frac{K}{M}\dot{x_p} - \frac{\left(\dot{F_f} + \dot{F_L}\right)}{M} \tag{19}$$

and $b(x)$ is the control gain function and can be determined by

$$b(x) = \frac{(C_1\Psi_1 + C_2\Psi_2)}{M} \tag{20}$$

In (19) and (20),

$$K = a\gamma\left(\frac{P_1A_1^2}{V_{01} + A_1\left(\frac{L}{2} + x_p\right)}\right) + \left(\frac{P_2A_2^2}{V_{02} + A_2\left(\frac{L}{2} - x_p\right)}\right) \tag{21}$$

$$C_1 = \frac{\gamma RTA_1}{V_{01} + A_1\left(\frac{L}{2} + x_p\right)} \tag{22}$$

$$C_2 = \frac{\gamma RTA_2}{V_{02} + A_2\left(\frac{L}{2} - x_p\right)} \tag{23}$$

The relationship between the valve orifice area and control signal is

$$A_v = wk_vu \tag{24}$$

where k_v is the spool position gain of the proportional control valve and w is the valve orifice area gradient.

3.2.2 Sliding Mode Control Law

The sliding-mode control used for the system under consideration is based on an integral sliding surface proposed in [Shen, Zhang, Barth, & Goldfarb, 2006]. The scheme consists of two components; the equivalent component and the robust component. The equivalent component is somewhat similar to feedback linearizing and the robust component is meant for dealing with model uncertainty. The final control law with the integral sliding surface is:

$$u = \begin{cases} \frac{1}{wk_v}\left(\frac{\dddot{x}_d - \hat{f}(x) - 3\lambda\ddot{e} - 3\lambda^2\dot{e} - \lambda^3 e}{\hat{b}(x)} - \frac{G}{\hat{b}(x)} \cdot \frac{s}{\emptyset}\right), |s| \le \emptyset \\ \frac{1}{wk_v}\frac{\dddot{x}_d - \hat{f}(x) - 3\lambda\ddot{e} - 3\lambda^2\dot{e} - \lambda^3 e}{\hat{b}(x)} - \frac{G}{\hat{b}(x)} sgn(s), |s| > \emptyset \end{cases} \quad (25)$$

where e is position error and x_d is the desired position.

The convergence of the system trajectory to the sliding surface with the rate of η is guaranteed if the value of G in Eq. (25) satisfies the following inequality:

$$G \ge \beta(F + \eta) + (\beta - 1)\left|\hat{b}(x)\hat{A}_{v,eq}\right|$$

where F is a boundary function that limits the estimation error on $f(\boldsymbol{x})$ and β is the gain margin of the designed controller, $\hat{b}(\boldsymbol{x})$ is the estimated control gain while $\hat{A}_{v,eq}$ is the equivalent control component.

3.3 Objective Function

The optimization algorithm is used for model-based offline tuning of two SMC parameters, Robustness (G) and Control Bandwidth (λ) with constant boundary layer thickness ($\emptyset$), for accurate and smooth position control of the pneumatic actuator. An objective function consisting of a linear combination of weighted root mean square value of tracking errors and time derivatives of acceleration (jerk) is used. The weighted approach converts the multi-objective function into a single objective function for application of the proposed globalized local search algorithm for controller tuning. The proposed algorithm is based on a variant of Nelder-Mead's algorithm, which cannot handle a vectorized multi-objective function.

$$f(\mathcal{E}_{rms}, j_{rms}, t)|_{(G,\lambda,\emptyset)} = w_1\mathcal{E}_{rms} + w_2 j_{rms} \quad (26)$$

where $w_1 > 0$ and $w_2 > 0$ are the weights of root mean square tracking error $\mathcal{E}_{rms}$ and root mean square value of jerk j_{rms}, respectively such that $w_1 + w_2 = 1$.

$$\mathcal{E}_{rms} = \sqrt{\frac{{\mathcal{E}_1}^2 + {\mathcal{E}_2}^2 + \cdots {\mathcal{E}_N}^2}{N}} \tag{27}$$

In (27) $\mathcal{E}_1, \mathcal{E}_2 \cdots \mathcal{E}_N$ are the samples of error in the piston position of the pneumatic cylinder used in the servo pneumatic system. N is the number of samples used to determine root mean square tracking error.

$$j_{rms} = \sqrt{\frac{{j_1}^2 + {j_2}^2 + \cdots {j_N}^2}{N}} \tag{28}$$

where $j_1, j_2 \cdots j_N$ are the samples of the 1st time derivative of piston acceleration.

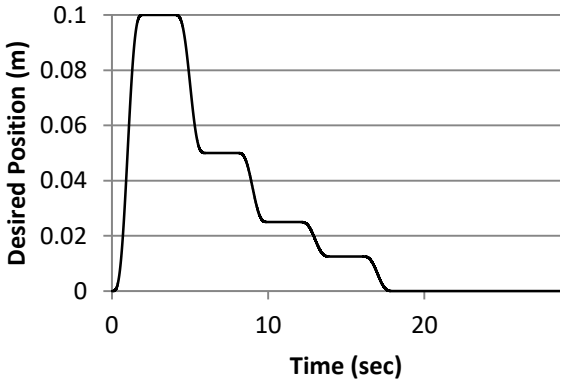

Figure 3.3 Multiple step polynomials

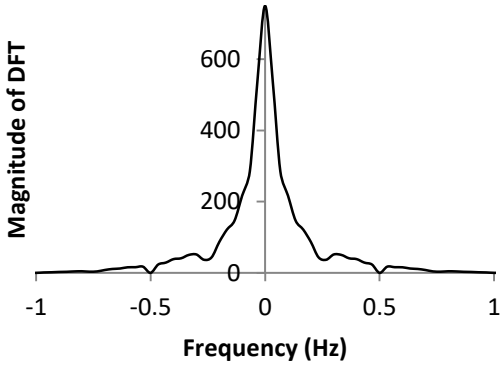

Figure 3.4 Discrete Fourier transform (DFT) of multiple step polynomials

$\mathcal{E}_{rms}$ and j_{rms} are computed from the system's simulated responses when it is made to track multiple step polynomials shown in Figure 3.3 as a test signal. Multiple step polynomials have been structured as a reference because they require tracking as well as regulation in position control. Furthermore, they contain frequency components of significant amplitude up to 0.5 Hz as shown in Figure 3.4. Therefore, a controller

tuned using such multiple step polynomials should give optimal performance in tracking sinusoids (up to 0.5 Hz) as well.

3.4 Tuning Setup and Process

The process loop of the model-based offline tuning of SMC parameters for the servo pneumatic position control system described in Section 3.1 is shown in Figure 3.5. The process loop is setup using an optimization algorithm described in Chapter 2, the master code, and the simulation model of the system. The simulation model consists of the servo pneumatic model of the system discussed in Section 3.2 with the system parameters given in Table 3.1.

TABLE 3.1 PNEUMATIC SYSTEM PARAMETERS

Parameter	Description	Value	Unit
P_s	Supply pressure	0.6	MPa
P_{atm}	Atmosphere pressure	0.1	MPa
M	Mass of total load on the piston	16	kg
L	Piston stroke	0.3	m
A_1	Piston annulus area – side 1	0.00126	m^2
A_2	Piston annulus area – side 2	0.00106	m^2
T	Temperature of air	300	K
α	Pressure-volume work correction factor	1.2	-
C_d	Valve coefficient of discharge	0.18	-
w	Valve orifice area gradient	$22.6x10^{-5}$	m^2/m
K_v	Valve spool position gain	$0.25x10^{-3}$	m/V
P_{cr}	Valve critical pressure ratio	0.528	-
F_s	Static friction	38.5	N
F_c	Coulomb friction	32.9	N

The optimization algorithm controls the simulation model with the help of a master code and steers the system towards optimal controller gains using the results from logically guided iterative runs of the model. The master code runs the simulation model for a closed-loop operation of tracking the test signal shown in Figure 3.3 on the request of the optimization algorithm and computes the objective function. It uses the

controller parameters determined by the algorithm for the iterative run and hands over the resulting value of the objective function to the algorithm for the next logical decision.

In order to find the optimal controller gains, the algorithm minimizes the objective function with the desired minimum set equal to zero and solves the optimization problem, which can be written in mathematical form as

$$\underset{G,\lambda,\emptyset}{\text{minimize}}(w_1\mathcal{E}_{rms} + w_2 j_{rms})$$

subject to:

$$0 \leq G \leq 250;$$
$$0 \leq \lambda \leq 15;$$
$$\emptyset = 10.$$

where the bounds on G, λ and $\emptyset$ define the search space for the optimization algorithm.

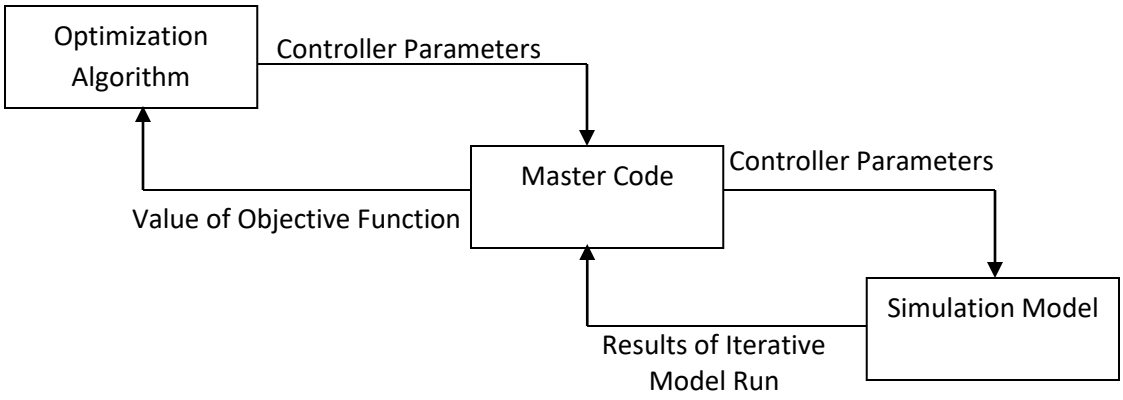

Figure 3.5 Process loop of the model-based offline tuning

The algorithm, the master code, the objective function and the simulation model all are coded in MATLAB for improved compatibility. Once the optimal controller parameters are found by the offline tuning, they are then used to run the actual servo pneumatic position control system. The proposed technique of tuning SMC parameters aims at the desired performance for both multiple step polynomials and sinusoidal

inputs. The experiments have therefore been designed to verify the proposed technique's usefulness in both cases with different weights for accuracy and smoothness in the proposed objective function.

3.5 Tuning Results and Discussion

Application of the proposed optimization algorithm for tuning sliding mode controller parameters for a servo pneumatic position control discussed in Sections 3.1 and 3.2 is a multimodal optimization problem having many local minima within the region of interest. Figure 3.6 shows the zoomed view of the objective function given in Section 3.3, which shows that the function, indeed, has many local minima within the search space. The proposed algorithm because of its capability to achieve satisfactory globalization within the region of interest for multimodal optimization problems with simple bounds is an excellent choice for such applications.

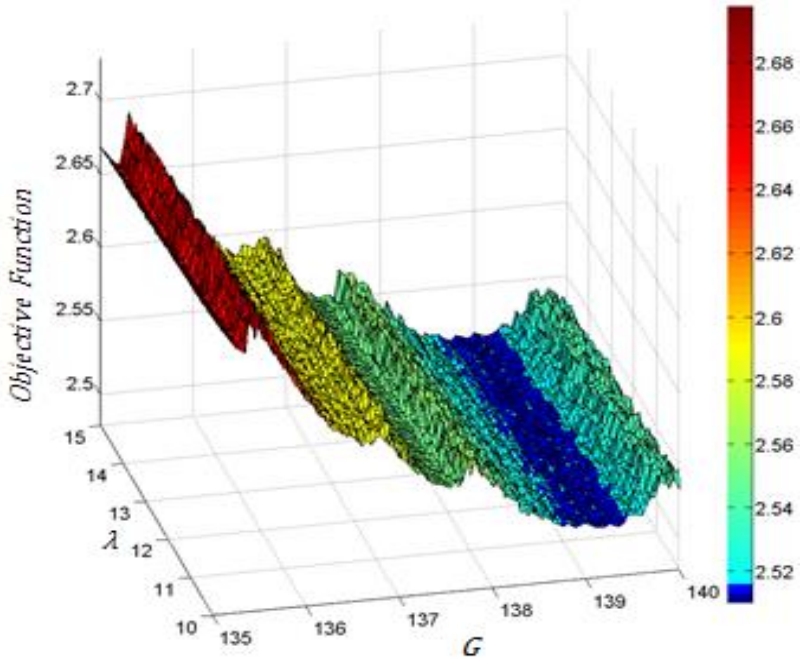

Figure 3.6 Objective function for tuning SMC parameters with w_1=0.99, w_2=0.01

Experimental results shown in Figures 3.7, 3.8 and 3.9 indicate that the servo pneumatic system tuned using proposed algorithm performs as desired and the optimal parameters found by the algorithm with increased priority for smoothness effectively reduce jerk and vice versa. Simulation and experimental results are in total agreement in the trend of system performance at parameters optimized for different levels of priorities (weights) for accuracy and smoothness as shown in Table 3.2.

TABLE 3.2 SYSTEM PERFORMANCE WITH SMC PARAMETERS TUNED OFFLINE USING THE PROPOSED ALGORITHM

Input	**Weights**		**Optimal Parameters Found**		**Results**			
	w_1	w_2	G (m/s^3)	λ (rad/s)	**Simulation**		**Experiment**	
					$\mathcal{E}_{rms}$ (mm)	j_{rms} (N/sec)	$\mathcal{E}_{rms}$ (mm)	j_{rms} (N/ms)
Sinusoid (0.1 Hz)	0.99	0.01	138.8762	14.1056	0.88	212.487	2.42	20.38
	0.95	0.05	180.5481	10.4591	1.01	205.230	3.77	19.59
	0.85	0.15	135.6433	10.0025	1.18	202.898	4.83	19.44
	0.75	0.25	4.9935	13.2101	2.00	201.124	6.05	19.42
Multiple Step Polynomials (MSP)	0.99	0.01	138.8762	14.1056	0.45	206.586	1.56	9.39
	0.95	0.05	180.5481	10.4591	0.54	204.055	1.96	8.51
	0.85	0.15	135.6433	10.0025	0.65	203.034	3.00	7.58
	0.75	0.25	4.9935	13.2101	0.84	202.029	3.95	7.25

The effective use of the proposed algorithm for simulation-based controller tuning depends on the sufficient adequacy of the system model. The results reveal that taking at least major system dynamics into account makes the model sufficiently adequate for such tuning method. Increase in experimental root mean square error and decrease in jerk along with those in simulation reflects that the system model used is sufficiently adequate to follow the behavior of real-life system within the region of interest. Though magnitudes of performance indices are different in simulation and the actual system due to modeling uncertainties, the proposed method remains effective due to similar trend of change in their magnitudes on changing controller gains.

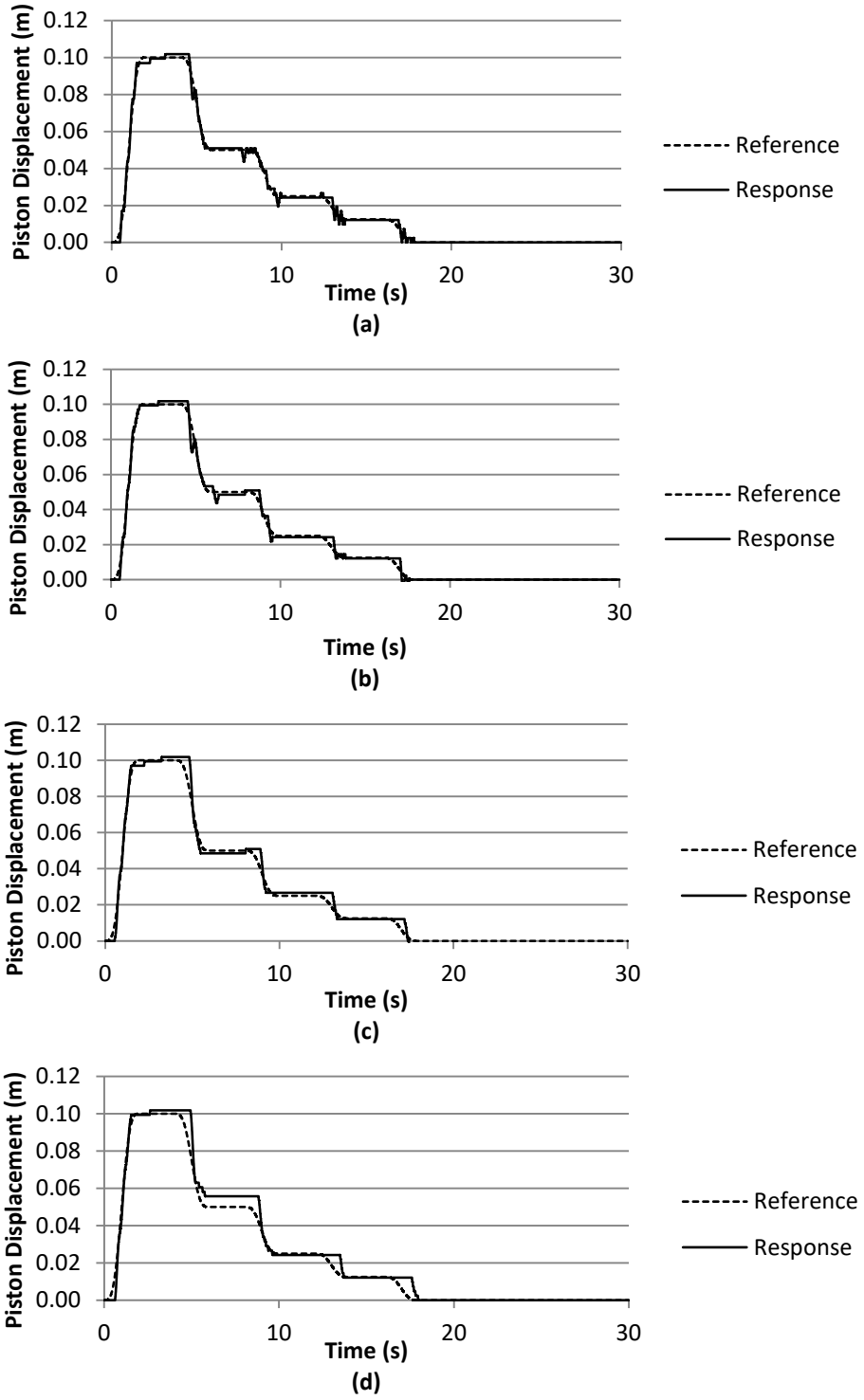

Figure 3.7 Experimental results of multiple step polynomials tracking with optimized SMC at (a) w_1=0.99, w_2=0.01 (b) w_1=0.95, w_2=0.05 (c) w_1=0.85, w_2=0.15 (d) w_1=0.75, w_2=0.25

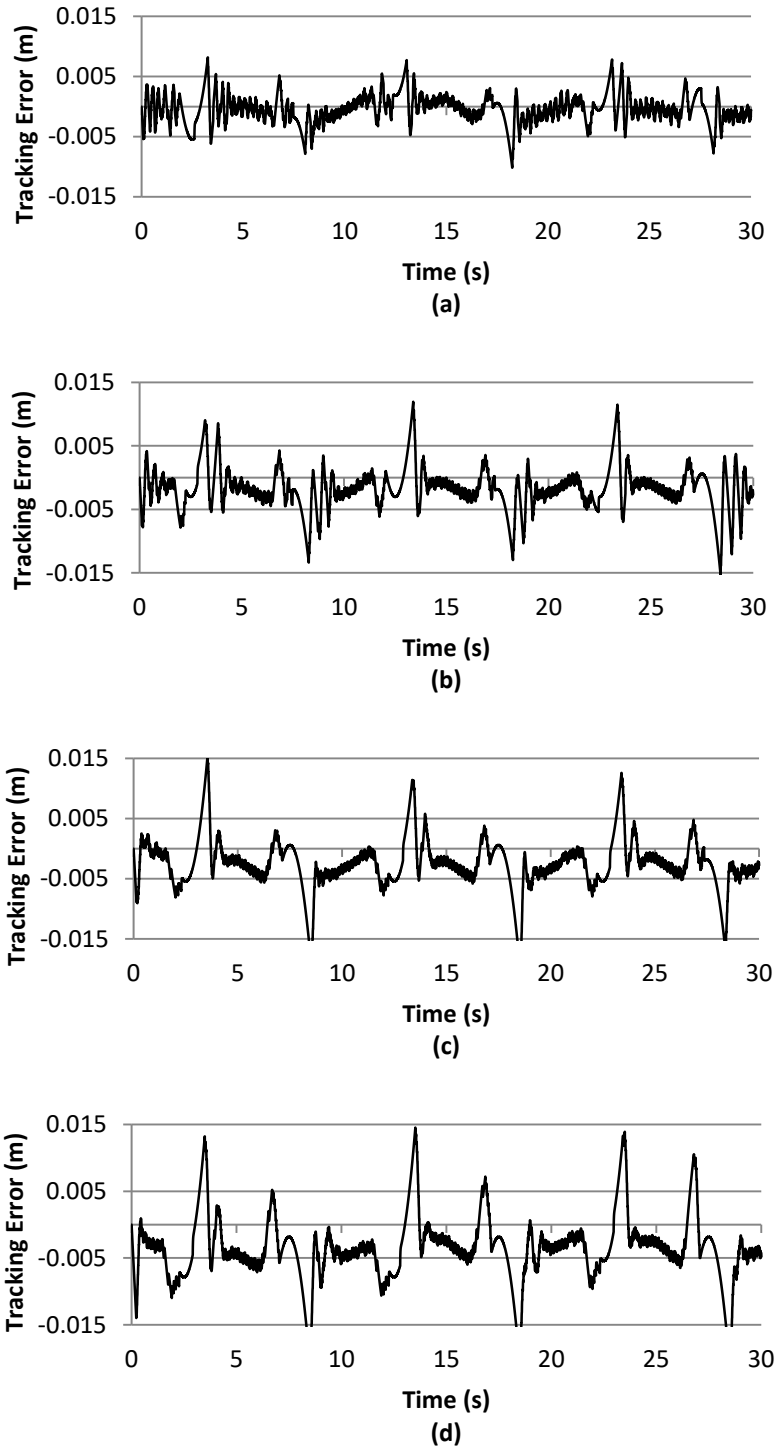

Figure 3.8 Experimental results of 0.1Hz sinusoidal tracking with optimized SMC at (a) w_1=0.99, w_2=0.01 (b) w_1=0.95, w_2=0.05 (c) w_1=0.85, w_2=0.15 (d) w_1=0.75, w_2=0.25

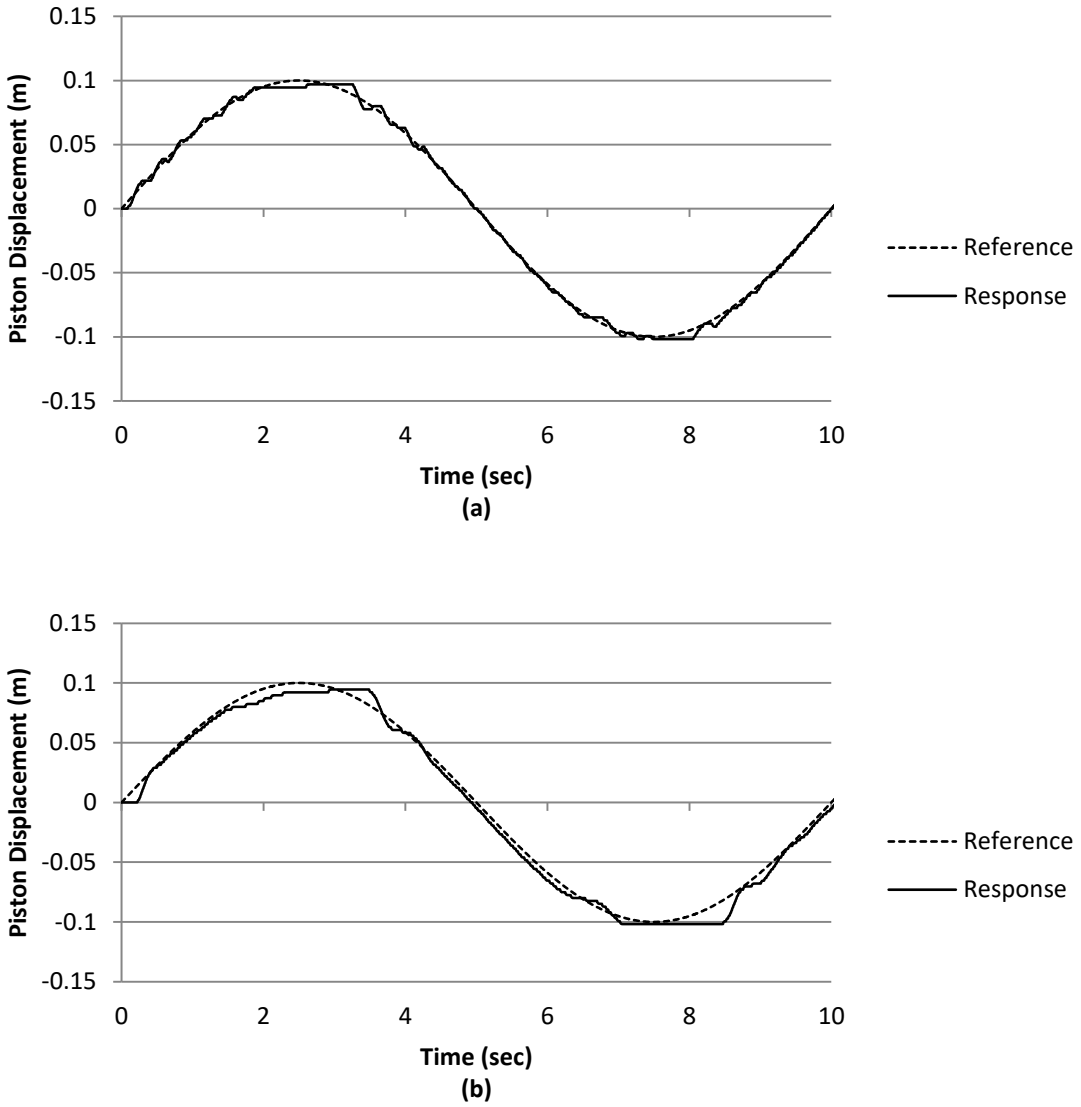

Figure 3.9 Experimental results of 0.1Hz sinusoidal tracking with optimized SMC at (a) w_1=0.99, w_2=0.01 (b) w_1=0.75, w_2=0.25

It can be conveniently misunderstood by looking at the experimental and simulation trend of tracking error and smoothness that increasing the tracking error reduces the jerk and some sort of inverse proportionality relationship exists between them. It should be noted that this trend is merely because of weights of respective parameters to be optimized in the multi-objective function. Otherwise finding a point

having higher tracking error does not automatically guarantee less jerk and vice versa. In the region of interest, there are some points at which both the error and jerk values are high, but such a point cannot become a local/global minimizer of the continuous aggregated objective function of error and jerk. Therefore, the algorithm never converges on them.

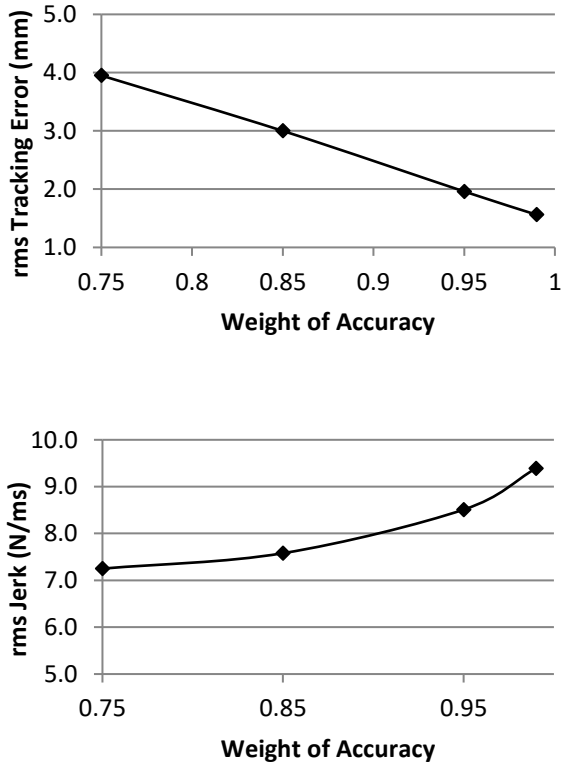

Figure 3.10 Experimental values of tracking error and jerk in multiple step polynomials tracking with optimal parameters found using different weights for optimization

To ensure greater accuracy in tracking, controller parameters should be such that the controller becomes sensitive to even smaller deviation from sliding surface and should take minimum time to bring the system back to it. In case of constant boundary layer thickness ($\emptyset$), as is the case in this thesis, robustness parameter (G) should be large to cause effective chattering with an adequate value of control bandwidth (λ) to

minimize the time taken by the system to come back to the sliding surface. This enhances jerk and therefore smoothness of tracking deteriorates. If the weight of accuracy (w_1) in multi-objective function is reduced resulting in greater weight for smoothness (w_2), the algorithm finds the optimal values of parameters at which the controller reduces its sensitivity towards error. This prevents smoothness from deteriorating and thus creates an important trade-off strategy for optimization. However, such a compromise is reasonable only until the priority level (weight) for accuracy is reduced from 100% to 85%. Beyond this limit, compromising error does not increase smoothness significantly as shown in Figure 3.10. So, the variation of weights in objective function should essentially be bounded.

TABLE 3.3 COMPARISON OF SYSTEM PERFORMANCES WITH SMC PARAMETERS TUNED USING PROPOSED TUNING METHOD AND MANUAL ONLINE TUNING BASED ON TRIAL AND ERROR IN TRACKING SINUSOIDAL AND MULTIPLE STEP POLYNOMIALS TRAJECTORIES WITH SAME SMOOTHNESS

Input	**Manual Online Tuning**				**Proposed Tuning Method**				**%age Improvement in Accuracy**
	Parameters		**Experimental Results**		**Parameters**		**Experimental Results**		
	G **(m/s³)**	λ **(rad/s)**	$\mathcal{E}_{rms}$ **(mm)**	j_{rms} **(N/ms)**	G **(m/s³)**	λ **(rad/s)**	$\mathcal{E}_{rms}$ **(mm)**	j_{rms} **(N/ms)**	
Sinusoid 0.1 Hz	100	10	5.30	19.61	180.5481	10.4591	3.77	19.59	28.9
Multiple Step Polynomials (MSP)	100	10	3.39	8.48	180.5481	10.4591	1.96	8.51	42.2

To further test the usefulness of proposed method for tuning controller parameters, the results are compared with the performance of same servo pneumatic system with sliding-mode controller parameters tuned using manual online tuning based on trial-and-error reported in [Ramhuzaini, He, & Sepehri, 2016]. Apart from saving the enormous amount of time and effort for tuning, the proposed method improves the

system response accuracy by 28.9% in sinusoidal tracking and by 42.2% in tracking multiple step polynomials with almost same smoothness. The comparison is shown in Table 3.3, Figure 3.11 and Figure 3.12.

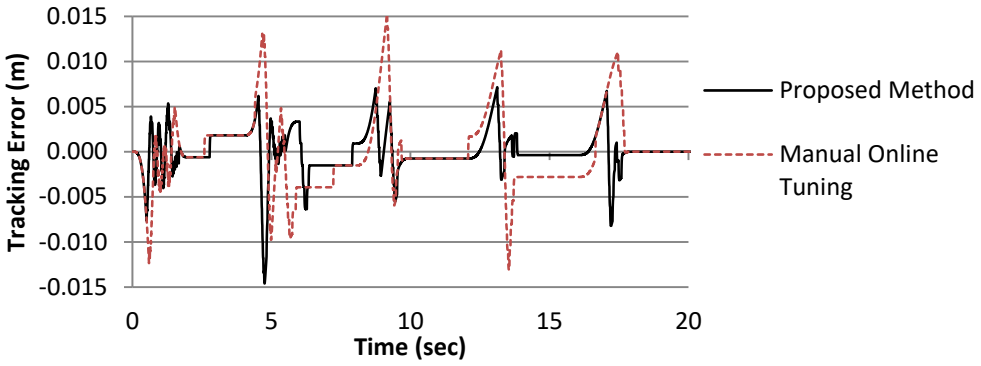

Figure 3.11 Comparison of performances of servo pneumatic system with SMC parameters tuned using manual online tuning and proposed tuning method while tracking multiple step polynomials trajectory with same smoothness

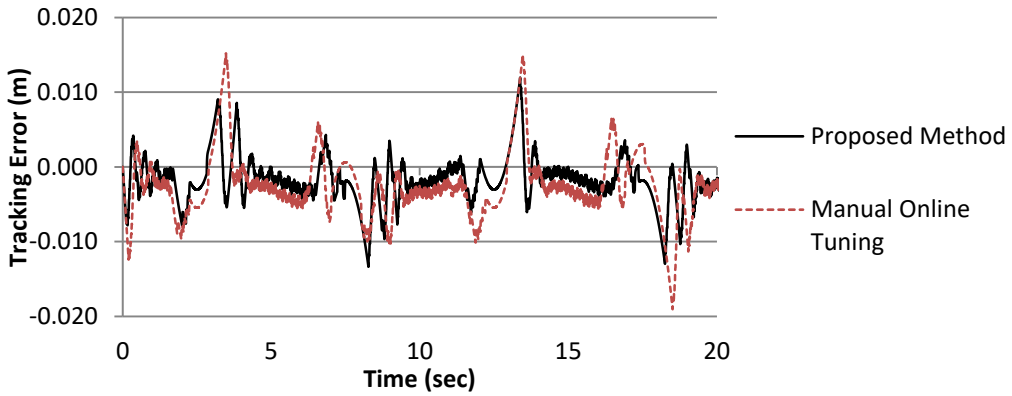

Figure 3.12 Comparison of performances of servo pneumatic system with SMC parameters tuned using manual online tuning and proposed tuning method while tracking sinusoid (0.1Hz) with same smoothness

3.6 Summary

The globalized and bounded Nelder-Mead algorithm with deterministic restarts proposed in Chapter 2 was applied to the model-based offline tuning of sliding mode

controller parameters for a servo pneumatic position control system with 4-quadrant loading. The model-based offline tuning based on the proposed algorithm outperformed the rigorous manual online tuning of the controller for the same application done for an earlier published work in terms of desired performance. The proposed model-based offline tuning method did not require a perfect model as the results revealed that it could function very well for a sufficiently adequate model with the most dominant of the system dynamics taken into account.

Chapter 4

Model-free Online Tuning of Sliding Mode Controller Parameters[4]

The model-based offline tuning presented in Chapter 3 requires a sufficiently adequate system model, which in some applications, is difficult to attain. Moreover, it is not generally appreciated as an essential requirement for controller tuning by the end-user like industry. An improvement in performance of optimization algorithm for tuning is expected if it relies on measurements coming directly from an actual physical system and not just its mathematical model. Therefore, in this chapter, the optimization algorithm called GBNM with deterministic restarts proposed in Chapter 2 is applied for tuning of controller parameters using direct online measurements of responses. The algorithm is used for tuning of sliding mode controller parameters for the same servo pneumatic system that has been used in Chapter 3. This is done to facilitate the comparison between two tuning approaches.

[4] A version of this chapter has been published in Butt, K., & Sepehri, N. (2018). Model-free online tuning of controller parameters using a globalized local search algorithm. *Optimal Control Applications and Methods*, 39(5), 1750-1765.

4.1 Tuning Setup and Process

To setup the proposed model-free online tuning, the position control system is augmented by the optimization algorithm, a master code and an executable code. The optimization algorithm executes the logically guided iterative runs of the position control system with the help of master and executable codes. The optimization algorithm and both the master and executable codes are developed in MATLAB environment for improved compatibility. The process loop of tuning is shown in Figure 4.1.

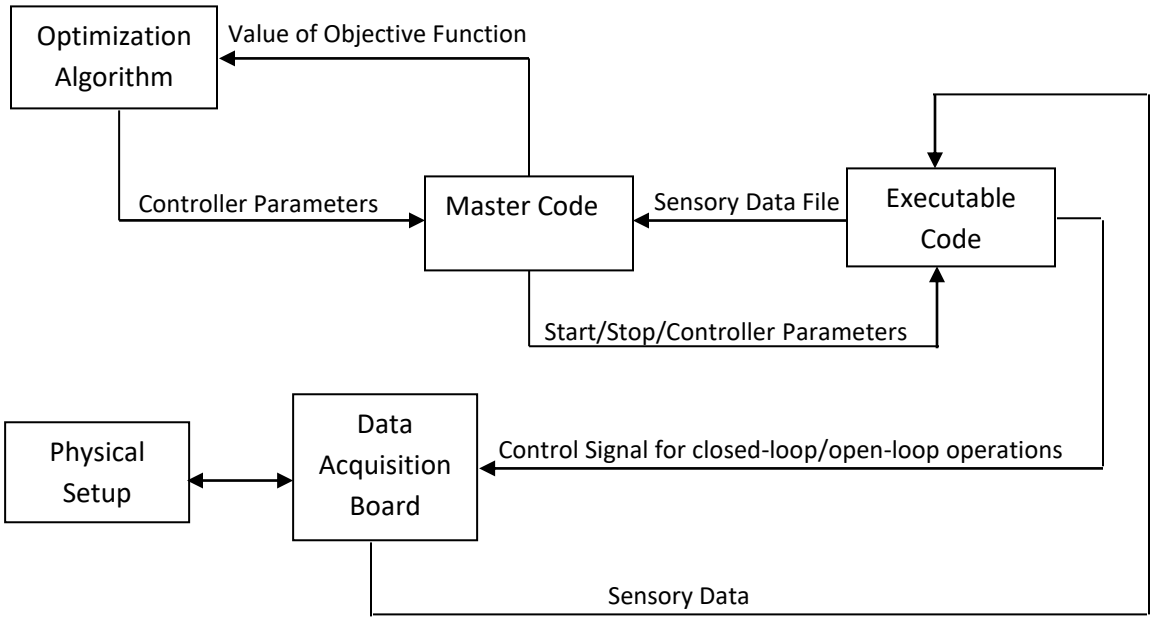

Figure 4.1 Process loop of the proposed model-free online tuning

A repeating sequence of operations is required to be carried out on the physical setup to implement the process loop of online tuning. The sequence is modeled as a Simulink diagram which resides in the host PC of the system. During build on the target process, QUARC compiles the Simulink diagram as an executable code and downloads

it onto the target PC of the system using TCP/IP. The executable code makes use of QUARC Hardware-In-Loop and Stream Application Programming Interfaces to read/write the Quanser Q8 data acquisition board interfaced with the target PC and physical setup. The data acquisition board implements the operations on the physical setup as and when instructed by the code.

A master code is developed as a MATLAB script and it also resides in the host PC of the system. The code is programmed to control the periodic execution of executable code on the target PC and to act as an interface between the optimization algorithm and the executable code. It reads the sensory data file written by the executable code and evaluates the objective function using the data. Based on the value of objective function provided by the master code, the optimization algorithm returns the logically determined set of controller parameters to the master code for succeeding tuning cycle. The master code writes the updated controller parameters to the executable code for implementation.

TABLE 4.1 OPERATIONS CARRIED OUT BY THE OPTIMIZATION ALGORITHM AND MASTER AND EXECUTABLE CODES TO IMPLEMENT THE PROCESS LOOP OF ONLINE TUNING

No.	**Operation**	**Duration (s)**
1.	Start the executable code	--------
2.	No operation	4
3.	Piston to extend to initial position for an iterative system run	3
4.	Piston to a standstill	3
5.	Iterative system run	20
6.	Piston to retract to idle position	3
7.	No operation	8
No.	**Operation**	**Duration (s)**
8.	Stop the executable code	--------
9.	Writing sensory data obtained from iterative system run to a file	10
	Evaluating the cost function	
	Updating the controller parameters for succeeding tuning iteration	
	Total Duration	51

The operations carried out by the optimization algorithm and the master and executable codes along with their duration are shown in Table 4.1 in the order they occur.

The tuning process minimizes the multi-objective cost function detailed in Section 3.3 using the optimization algorithm parameters given in Table 4.2. The process solves the optimization problem, which can be written in mathematical form as

$$\underset{G,\lambda,\emptyset}{\text{minimize}}(w_1\mathcal{E}_{rms} + w_2 j_{rms})$$

subject to:

$$0 \leq G \leq 250;$$

$$0 \leq \lambda \leq 15;$$

$$\emptyset = 10.$$

TABLE 4.2 PARAMETERS OF OPTIMIZATION ALGORITHM FOR ONINE TUNING

Parameter Description	Value
Number of deterministic restarts allowed	6
Maximum function evaluations	480
Reflection coefficient	1
Expansion coefficient	2
Contraction coefficient	0.5
Shrink coefficient	0.5
Initial simplex size coefficient	5
Small simplex convergence test coefficient	4e-03
Function value convergence test coefficient	5e-04
No convergence test coefficient (function evaluations)	80
Duration of one iterative system run	20 s

The bounds on G, λ and $\emptyset$ define the search space for the optimization algorithm. Here $\mathcal{E}_{rms}$ taken in mm and j_{rms} taken in dm/s^3 are computed from the system's actual response when the system is made to track a multiple step polynomials trajectory shown in Figure 3.3 for 20s referred to as iterative system run in this chapter. As explained in Chapter 3, multiple step polynomials trajectory is chosen as a reference for iterative system run, because it requires tracking as well as regulation. Moreover, the

multiple step polynomials trajectory has frequency components of significant amplitude up to 0.5 Hz. Therefore, a controller tuned using multiple step polynomials should give optimal performance in regulation as well as tracking sinusoids (up to 0.5 Hz).

4.2 Tuning Results and Discussion

The globalized bounded Nelder-Mead algorithm with deterministic restarts and a linearly growing memory vector is a multimodal optimization algorithm. It can handle multimodal optimization problems having many local minima such as controller tuning. It avoids the vicinity of the local minimum already found and tries to explore the new ones. The convergence characteristic of the algorithm while tuning the sliding mode controller parameters online for the servo pneumatic position control application is shown in Figure 4.2. The convergence characteristic shows that the algorithm finds a new local minimum of the cost function in each deterministic restart and successfully avoids getting stuck at the same local minimum.

The globalization of the algorithm improves by increasing the number of deterministic restarts allowed. With one restart allowed, the algorithm becomes a plain Guin augmented variant of Nelder-Mead, which is a local search algorithm. Such a local search algorithm may merely converge to a local minimum, which in the case of any multimodal optimization problem like controller tuning, may not be the better one. Table 4.3 compares the performance of the proposed online tuning method with the algorithm having one and six deterministic restarts allowed for the online tuning of SMC parameters. The performance of the proposed online tuning method in terms of

meeting the tuning objectives i.e. minimizing the cost function improved up to 10.5% by increasing the number of deterministic restarts from one to six.

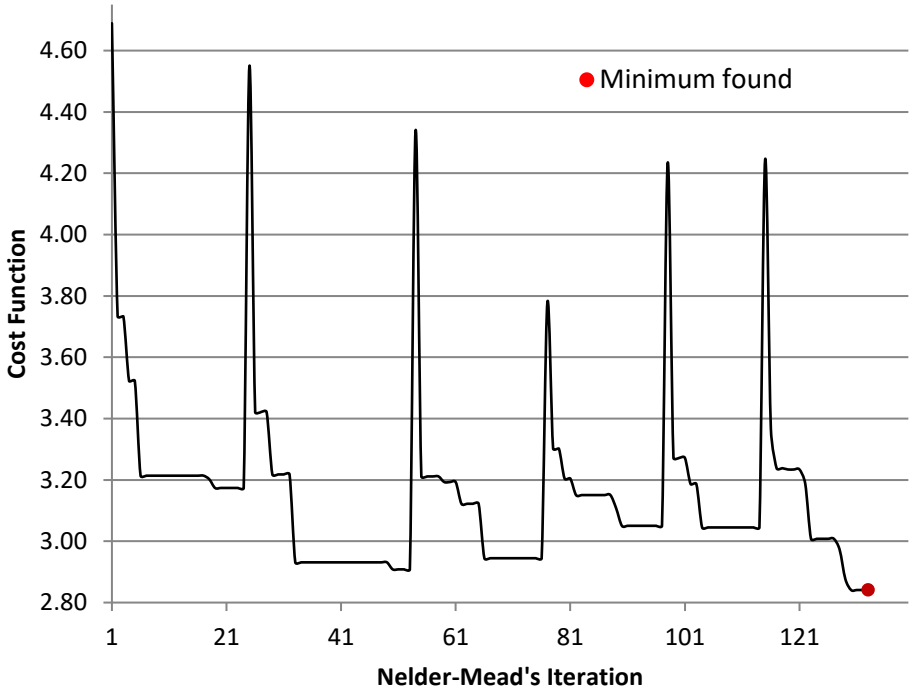

Figure 4.2 Convergence characteristic of the globalized bounded Nelder-Mead algorithm with six deterministic restarts during online tuning of sliding mode controller parameters at w_1=0.90, w_2=0.10

TABLE 4.3 COMPARISON OF PERFORMANCE OF ONLINE TUNING ALGORITHM HAVING ONE DETERMINISTIC RESTART AGAINST THE ONE WITH SIX RESTARTS

Weights		**Minimized value of the cost function**		**Improvement in performance**
Accuracy (w_1)	**Smoothness (w_2)**	**Algorithm with 1 deterministic restart allowed**	**Algorithm with 6 deterministic restarts allowed**	
0.99	0.01	1.7877	1.7877	0%
0.90	0.10	3.1737	2.8410	10.5%
0.80	0.20	3.9930	3.9329	1.5%

The introduction of breaks and resetting the system to its idle position between iterative system runs for online tuning increases the time taken for the process to complete. This is difficult to avoid without exactly knowing the convergence aspects of

the optimization algorithm with respect to system stability. Although SMC guarantees convergence to the sliding surface when robustness and control bandwidth parameters satisfy the known condition given in Section 3.2.2, incorporating this condition introduces nonlinear constraint inequality to the optimization problem, which makes the search space lose its simplicity. This is detrimental to the online tuning method proposed in this work as the optimization algorithm exploits the simplicity of the search space for its deterministic restarts and computational efficiency.

Application of the globalized bounded Nelder-Mead algorithm with deterministic restarts for online tuning requires some adjustments to the algorithm. To construct the initial simplex for the succeeding run of the Guin augmented variant of Nelder-Mead's algorithm, it is ensured that the projected points should not match with not only the already existing points in the memory vector but also with any point lying close to those points by a Euclidian norm of less than 1e-3. The reason is that the response of the servo pneumatic position control application happens to be almost identical for a set of gains too close to each other and they do not have to be exactly similar for the same response. Therefore, for effective multimodal optimization and to eliminate the chances of getting stuck at one local minimizer, each initial simplex should avoid any already used initial simplex by a fair distance within the search space.

The Nelder-Mead's algorithm updates the simplex after each run using reflection, expansion, contraction (inside and outside) and shrinking. For reflection, expansion, and contraction, the algorithm must evaluate the objective function on reflected, expanded and contracted points. For shrinking, however, the points can be achieved without computing the cost function. This option, if adopted, negatively

affects the time efficiency of online tuning, as in this case, the algorithm has to compute the cost function on all points of the updated simplex before sorting the points of the updated simplex out for the succeeding run. This substantially increases the numerical cost of the algorithm, as the algorithm re-evaluates cost function at reflected, expanded or contracted points which it has already done while deciding on them. Therefore, this thesis suggests that the algorithm should compute the cost function at points arising because of shrinking as well so that the algorithm does not have to do cost function evaluations before sorting in each run. This helps avoid the re-evaluation of an already evaluated cost function at reflected, expanded or contracted points and thus decreases the number of system iterative runs required for online tuning by up to 50%.

The accuracy and jerk are conflicting objectives when SMC is tuned with constant boundary layer thickness for the servo pneumatic control application. To ensure increased accuracy, the robustness parameter (G) of SMC is required to induce effective chattering to bring the system back to the sliding surface as soon as possible. This requires the robustness parameter (G) to be large with an adequate value of control bandwidth (λ) which may enhance jerk and thus may cause deterioration in smoothness. If the weight for accuracy in aggregated multi-objective cost function is decreased, the tuning method finds such controller parameters at which SMC becomes less sensitive to limited loss of accuracy and does not chatter. This improves smoothness and thus makes the important trade-off for an optimal controller parameters search.

Experimental results shown in Figures 4.3, 4.4 and Table 4.4 indicate that the proposed online tuning method successfully tunes the sliding mode controller for the servo pneumatic position control according to the level of priorities set for accuracy and

smoothness. The optimal controller parameters found by the method with more priority for smoothness effectively reduce jerk and vice versa.

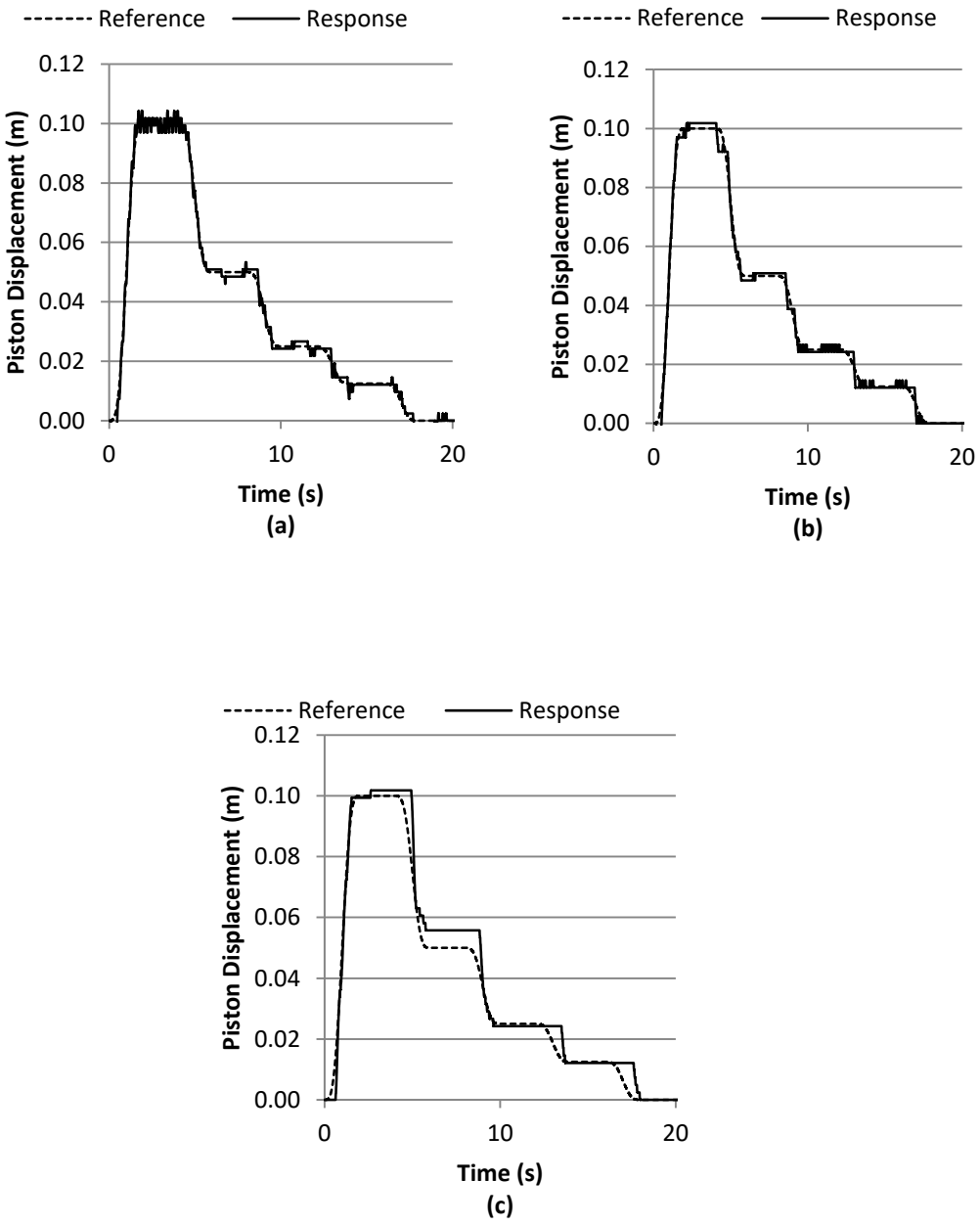

Figure 4.3 System performance in tracking a multiple step polynomials trajectory with SMC tuned online at (a) w_1=0.99, w_2=0.01 (b) w_1=0.90, w_2=0.10 (c) w_1=0.80, w_2=0.2

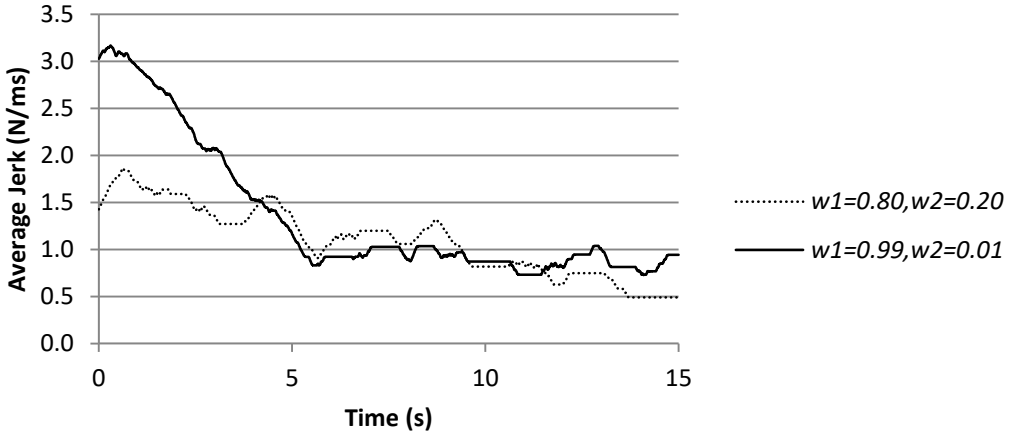

Figure 4.4 Comparison of rolling average of jerk in the system with SMC tuned online at w_1=0.99, w_2=0.01 and w_1=0.80, w_2=0.20 while tracking multiple step polynomials

The performance of the system with gains found using the online tuning method has also been examined for tracking sinusoids. The system shows a similar performance trend as in the case of multiple step polynomials according to the level of priorities set for accuracy and smoothness. Figures 4.5, 4.6 and Table 4.4 show the results of 0.05Hz sinusoidal tracking.

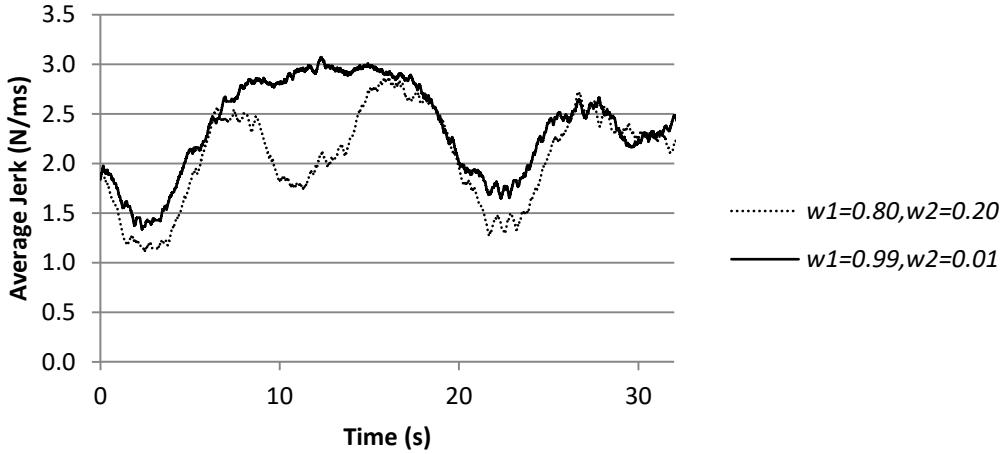

Figure 4.5 Comparison of rolling average of jerk in the system with SMC tuned online at w_1=0.99, w_2=0.01 and w_1=0.80, w_2=0.20 while tracking a sinusoid (0.05 Hz)

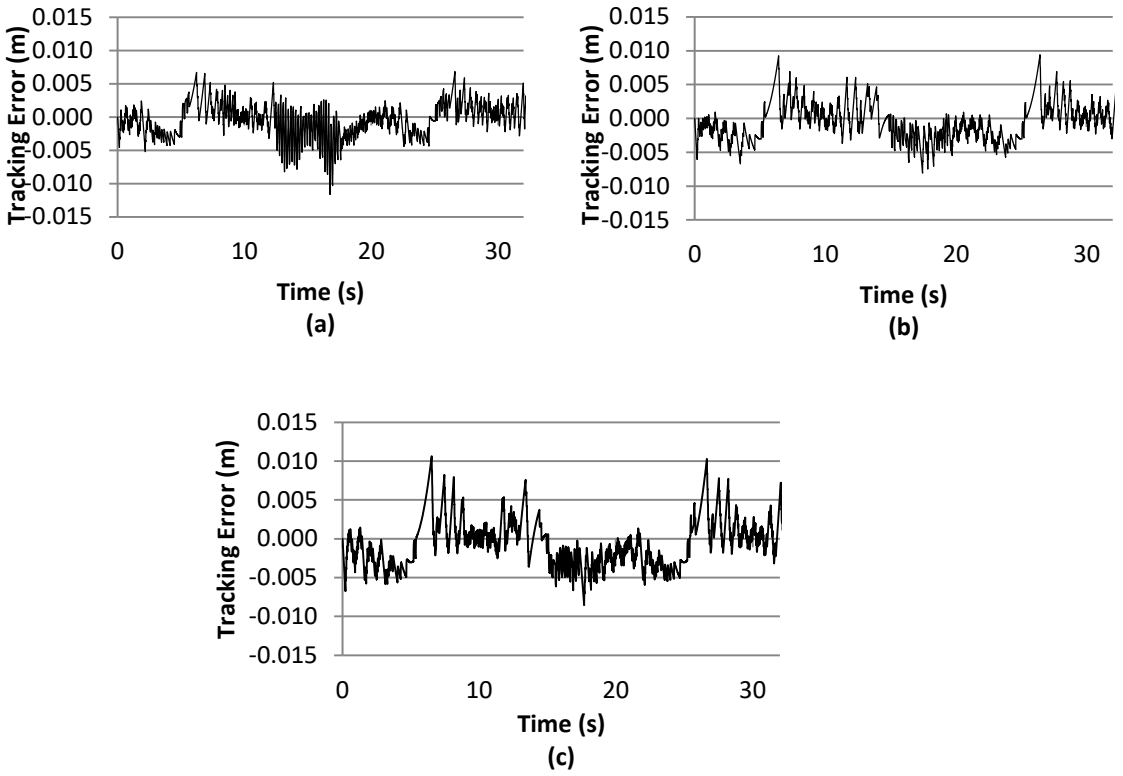

Figure 4.6 System performance in 0.05Hz sinusoidal tracking with SMC tuned online at (a) w_1=0.99, w_2=0.01 (b) w_1=0.90, w_2=0.10 (c) w_1=0.80, w_2=0.20

TABLE 4.4 SYSTEM PERFORMANCE WITH SMC PARAMETERS TUNED USING PROPOSED ONLINE TUNING METHOD

Input	Weights		Optimal Parameters Found		Results	
	Accuracy (w_1)	Smoothness (w_2)	Robustness G (m/s^3)	Control Bandwidth λ (rad/s)	rms Tracking Error (mm)	rms Jerk (N/ms)
Multiple step polynomials	0.99	0.01	223.27	11.65	1.65	2.41
	0.90	0.10	140.27	12.21	1.81	1.94
	0.80	0.20	65.31	14.28	1.96	1.89
Sinusoid (0.05 Hz)	0.99	0.01	223.27	11.65	2.51	3.62
	0.90	0.10	140.27	12.21	2.93	3.44
	0.80	0.20	65.31	14.28	3.28	3.15

Table 4.5 compares the results of the proposed model-free online tuning using globalized bounded Nelder-Mead with deterministic restarts against the model-based offline tuning proposed in Chapter 3 using the same algorithm coded in MATLAB, 2.4GHz Core i7 processor, and 8GB RAM. To compare the performance of both tuning

approaches, the optimal controller parameters found by both of them have been used to run the actual servo pneumatic position control system to determine the cost function given in Section 3.3. The algorithm parameters in both cases are kept as given in Table 4.2. The system shows improved performance with the controller parameters found using the proposed online tuning method, especially at higher weights for accuracy. This is due to the fact that in online tuning, the algorithm's decision making relies on measurements coming from the actual system and not its mathematical model. The actual physical system has a higher jerk as compared to its mathematical model because of air compressibility and other un-modeled uncertainties. In model-based offline tuning, the reduced value of jerk makes the algorithm resort to comparatively higher gains in the quest for greater accuracy, whereas in online tuning, the higher value of jerk makes the algorithm avoid such a region where the jerk is high enough to damage the highly prioritized term, the system accuracy. Furthermore, even a sufficiently adequate mathematical model can only guarantee a similar trend in system response parameters but can never guarantee a similar rate of change of system response parameters on changing operating conditions. Therefore, any fixed cost online tuning should compare favorably against model-based offline tuning of the same numerical cost. It should be noted that the model-based offline tuning is much faster than the model-free online tuning. The reason is that the model-based offline tuning uses iterative runs of system's mathematical model, whereas the proposed model-free online tuning uses tuning iterations of 55s in duration, shown in Table 4.1, consisting of iterative runs of the actual system. It is therefore advisable to use the proposed model-free online tuning only when the sufficiently adequate model is not available, and/or the

priority level of accuracy is very high. In the absence of these conditions, the model-based offline tuning is a better option. As the proposed model-free online tuning method is completely autonomous and does not require human intervention at all, the system can be left on its own for online tuning without human supervision.

TABLE 4.5 COMPARISON OF SYSTEM PERFORMANCE WITH SMC PARAMETERS TUNED USING MODEL-BASED OFFLINE TUNING AND PROPOSED ONLINE TUNING METHOD

Weights		**Model-based offline tuning**				**Model-free online tuning**				**Improvement in performance (%)**
w_1	w_2	**Optimal Parameters**		**Minimized value of the cost function**	**Time taken for tuning (h)**	**Optimal Parameters**		**Minimized value of the cost function**	**Time taken for tuning (h)**	
		G (m/s^3)	λ (rad/s)			G (m/s^3)	λ (rad/s)			
0.99	0.01	200.17	14.92	2.27	0.014	223.27	11.65	1.79	4.064	21.2
0.90	0.10	145.60	11.46	2.95	0.019	140.27	12.21	2.84	4.064	3.7
0.80	0.20	107.52	11.92	4.03	0.015	65.31	14.28	3.93	3.605	2.5

4.3 Summary

A method for model-free online tuning of controller parameters was proposed. The proposed method did not require a mathematical model of the system and therefore could be used for applications where knowledge of adequate mathematical model was difficult, and the system iterative runs were risk-free and not costly. The method made use of real-time iterative runs of actual physical system guided by computational intelligence for finding optimal controller parameters. The method found optimal controller parameters for system performance according to priorities of performance specifications set by defining weights in an aggregate multi-objective cost function. The proposed method performed very well in tuning controller parameters for the desired performance. It exploited the improved globalization and the lower numerical cost of the globalized bounded Nelder-Mead algorithm with deterministic restarts and a linearly

growing memory vector for time-efficient online controller tuning. The proposed online tuning method compared favorably against model-based offline tuning in terms of finding the optimal controller parameters at a fixed cost because of relying on measurements coming from an actual physical system and not just its mathematical model.

Chapter 5

Force-controlled Pneumatic Actuator with Long Transmission Lines and a Nonlinear Integral Sliding Surface [5]

After proposing time-efficient offline and online tuning methods and establishing their effectiveness for an unbiased comparison of controllers, this chapter investigates the actuating force control of a pneumatic actuator with long transmission lines and indirect pressure measurements. First, the chapter describes the schematic diagram of the actuator and derives its dynamic equations. Next, the chapter proposes a nonlinear integral sliding surface and presents the design of a full order sliding mode controller using the surface for an improved transient response of the actuator. The chapter also establishes the asymptotic stability of the controller built upon the proposed sliding surface.

[5] A version of this chapter has been included in Butt, K., & Sepehri, N. (2018). A nonlinear integral sliding surface to improve the transient response of a force-controlled pneumatic actuator with long transmission lines. Manuscript submitted for publication.

5.1 Schematic of the System

The schematic diagram of a force-controlled pneumatic actuator with long transmission lines and indirect pressure measurements is shown in Figure 5.1.

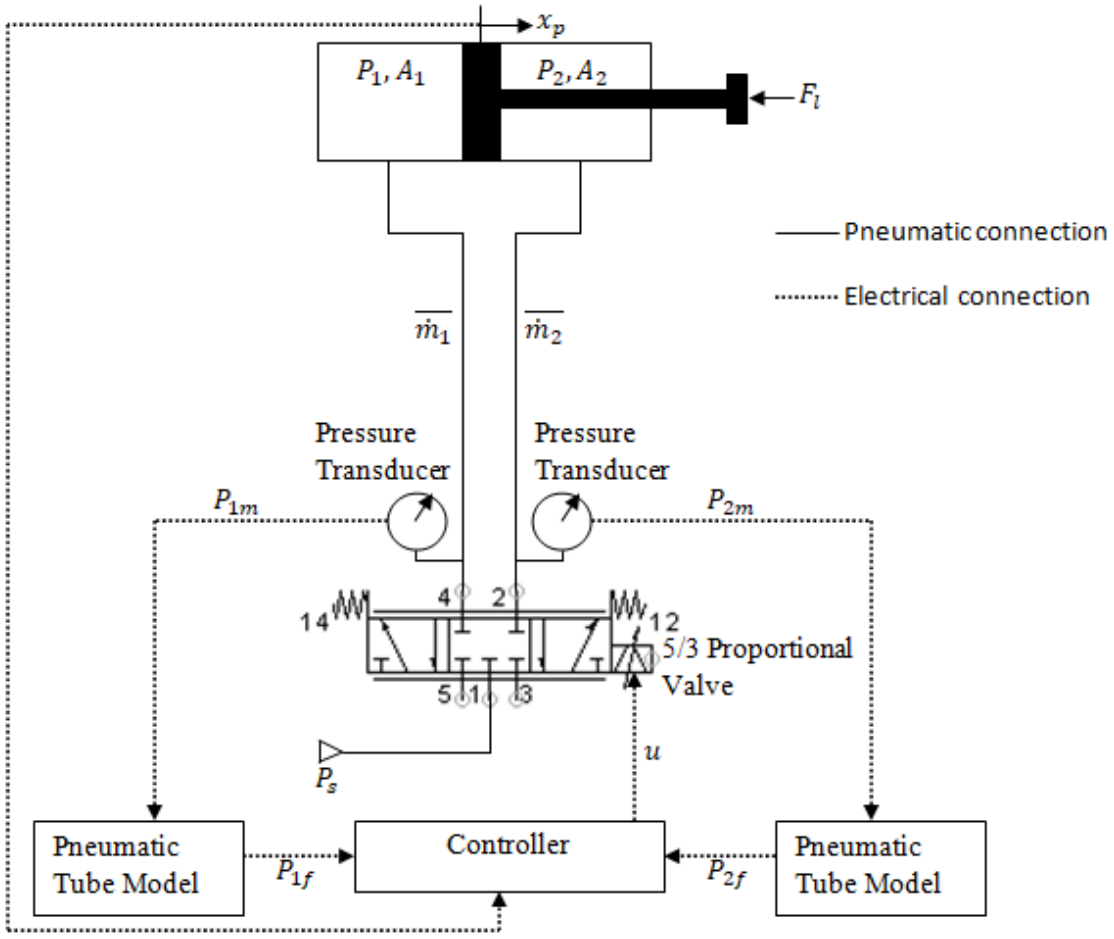

Figure 5.1 Schematic of force control application

The actuator consists of a single rod, double acting pneumatic cylinder subject to an external load including friction which acts as a disturbance. The cylinder chambers are charged and discharged using a 5/3 mass flow rate proportional valve connected to the cylinder using long pneumatic tubes of same length and diameter. The pressure transducers are installed at the valve output ports that are connected to the cylinder

chambers. The readings from pressure transducers are used to estimate chamber pressures of the cylinder using a first order transfer function with time delay model of connecting pneumatic tubes. Estimated chamber pressures and real-time piston displacement measurements are then taken as feedback for the implementation of force control on the pneumatic actuator.

5.2 System Dynamics

In the derivations given below, the overhead bar on the symbol represents a time delay of T_D in the corresponding parameter. This time delay is referred to as input delay in this thesis and is equal to the time taken by the acoustic wave to travel the long pneumatic tubes connecting valve and cylinder. It can be determined by the following equation [Richer & Hurmuzlu, 2000a]:

$$T_D = \frac{L_T}{C_{sd}} \tag{29}$$

where L_T is the length of the pneumatic tube, and C_{sd} is the speed of sound.

The piston-load dynamics is described by the following differential equation:

$$(m_p + m_l)\ddot{x}_p = P_1 A_1 - P_2 A_2 - P_a A_r - F_l \tag{30}$$

where m_p is the total mass of piston-rod assembly and attached accessories; m_l is the inertial mass associated with the external load; P_1 and P_2 are the chamber pressures; A_1 and A_2 are the effective piston areas; A_r is the area of the piston rod; P_a is the atmospheric pressure; F_l is the disturbance describing the effects of all external loads including friction.

The pressures in the chambers of pneumatic cylinder change because of compressible air flows in and out of the chambers, and the extension and retraction of the piston. The contribution of compressed air flow in and out of the chambers in changing chamber pressures is attenuated and time delayed. The attenuation and time delay are the effects of pneumatic tubes connecting valve and cylinder. Neglecting the air leakage through seals of the piston, piston rod, and valve, the cylinder pressure dynamics can be represented by:

$$\dot{P}_1 = \frac{\gamma RT}{V_1} \emptyset_1 \overline{m_{v,1}} - \alpha \frac{P_1 A_1}{V_1} \dot{x}_p \tag{31}$$

$$\dot{P}_2 = \frac{\gamma RT}{V_2} \emptyset_2 \overline{m_{v,2}} + \alpha \frac{P_2 A_2}{V_2} \dot{x}_p \tag{32}$$

where γ is the ratio of specific heats; R is the universal gas constant; T is the temperature of the compressed air; α is the pressure-volume work correction factor; $\emptyset_1$ and $\emptyset_2$ are the attenuation coefficients; $\overline{m_{v,1}}$ and $\overline{m_{v,2}}$ are the time-delayed mass flow rates in and out of the cylinder chambers through the valve; x_p is the piston displacement. Also

$$V_1 = V_{01} + A_1 \left(\frac{L}{2} + x_p \right) \tag{33}$$

$$V_2 = V_{02} + A_2 \left(\frac{L}{2} - x_p \right) \tag{34}$$

where V_{01} and V_{02} are the volumes of air at the end of the stroke, in connection ports and in connecting pneumatic tubes; L is the piston stroke length. x_p is zero when the piston is in the middle of the stroke length.

The attenuation coefficients represent the decrease in airflow in and out of the cylinder chambers through the valve. This decrease in air flow is induced by the

pressure drop along the connecting pneumatic tubes [Richer & Hurmuzlu, 2000a]. The attenuation coefficients can be determined by the following equation:

$$\emptyset_i(i = 1,2) = \exp\left(-\frac{RTR_T L_T}{2PC_{sd}}\right) \tag{35}$$

where R_T is the resistance of connecting pneumatic tube which can be determined by [Richer & Hurmuzlu, 2000a]

$$R_T = \begin{cases} 32\dfrac{\mu}{D^2} & \text{(fully developed laminar flow)} \\ 0.158\dfrac{\mu}{D^2}Re^{3/4} & \text{(wholly turbulent flow)} \end{cases} \tag{36}$$

where μ is the dynamic viscosity of air; D is the inner diameter of connecting pneumatic tube; *Re* is the Reynold's number.

Also, in (35)

$$P = \begin{cases} P_i(i = 1,2) & \text{(charging)} \\ P_a & \text{(discharging)} \end{cases} \tag{37}$$

The time-delayed mass flow rates of the compressed air in and out of the cylinder chambers are

$$\overline{m_{v,1}} = \overline{A_{v,1}}\psi_1\left(P_{u,1}, P_{d,1}\right) \tag{38}$$

$$\overline{m_{v,2}} = \overline{A_{v,2}}\psi_2\left(P_{u,2}, P_{d,2}\right) \tag{39}$$

where $\overline{A_{v,1}}$ and $\overline{A_{v,2}}$ are the time-delayed valve effective orifice areas; ψ_1 and ψ_2 are the flow functions.

The flow functions $\psi_i(i = 1,2)$ are given by

$$\psi_i(P_{u,i}, P_{d,i})$$

$$= \begin{cases} \dfrac{C_d P_{u,i}}{\sqrt{T}} \sqrt{\dfrac{\gamma}{R}\left(\dfrac{2}{\gamma+1}\right)^{\frac{\gamma+1}{\gamma-1}}} & \dfrac{P_{d,i}}{P_{u,i}} \le P_{cr} \text{ (chocked)} \\ \dfrac{C_d P_{u,i}}{\sqrt{T}} \left(\dfrac{P_{d,i}}{P_{u,i}}\right)^{\frac{1}{\gamma}} \sqrt{\dfrac{2\gamma}{R(\gamma-1)}} \sqrt{1-\left(\dfrac{P_{d,i}}{P_{u,i}}\right)^{\frac{\gamma-1}{\gamma}}} & \dfrac{P_{d,i}}{P_{u,i}} > P_{cr} \text{(unchocked)} \end{cases} \quad (40)$$

where C_d is the valve discharge coefficient; $P_{u,1}$ and $P_{u,2}$ are the valve upstream pressures; $P_{d,1}$ and $P_{d,2}$ are the valve downstream pressures; P_{cr} is the critical pressure ratio that differentiates between the chocked and unchecked flow regimes.

The control valve is a 5/3 proportional directional valve. Therefore, the effective orifice areas $A_{v,i}(i = 1,2)$ that are connected to the cylinder chambers are

$$A_{v,1} = -A_{v,2} = A_v \quad (41)$$

which implies

$$\overline{A_{v,1}} = -\overline{A_{v,2}} = \overline{A_v} \quad (42)$$

Using (42) in (38) and (39) and then inserting the resulting equations in (31) and (32), we see that the positive orifice area corresponds to charging of chamber 1 and discharging of chamber 2 whereas the negative orifice area corresponds to charging of chamber 2 and discharging of chamber 1. Therefore, the valve upstream and downstream pressures corresponding to both cylinder chambers under positive and negative orifice areas are

$$P_{u,1} = \begin{cases} P_s & \overline{A_v} \ge 0 \\ \overline{P_1} & \overline{A_v} < 0 \end{cases} \quad (43)$$

$$P_{u,2} = \begin{cases} \overline{P_2} & \overline{A_v} \ge 0 \\ P_s & \overline{A_v} < 0 \end{cases} \quad (44)$$

and

$$P_{d,1} = \begin{cases} \overline{P_1} & \overline{A_v} \geq 0 \\ P_a & \overline{A_v} < 0 \end{cases} \tag{45}$$

$$P_{d,2} = \begin{cases} P_a & \overline{A_v} \geq 0 \\ \overline{P_2} & \overline{A_v} < 0 \end{cases} \tag{46}$$

where P_s is the supply pressure; $\overline{P_1}$ and $\overline{P_2}$ are the time-delayed chamber pressures.

The actuating force is

$$F_a = P_1 A_1 - P_2 A_2 - P_a A_r \tag{47}$$

Neglecting spool inertia being very small, the valve dynamics can be sufficiently represented by

$$\dot{x}_s = -\frac{1}{\tau_v} x_s + \frac{K_v}{\tau_v} u_1 \tag{48}$$

where x_s is spool displacement, τ_v is valve response time, u_1 is control input, and K_v is spool position gain.

Equation (48) implies

$$\dot{\overline{x_s}} = -\frac{1}{\tau_v} \overline{x_s} + \frac{K_v}{\tau_v} \overline{u_1} \tag{49}$$

where $\overline{x_s}$ is time-delayed spool displacement.

For input delay compensation,

$$u = \overline{u_1} \tag{50}$$

Using (50) in (49)

$$\dot{\overline{x_s}} = -\frac{1}{\tau_v} \overline{x_s} + \frac{K_v}{\tau_v} u \tag{51}$$

The relationship between the valve effective orifice area A_v and spool displacement is

$$A_v = wx_s \tag{52}$$

where w is the valve orifice area gradient.

Equation (52) implies

$$\overline{A_v} = w\bar{x}_s \tag{53}$$

The pressure transducers are installed at the valve output ports connected to the cylinder chambers by long pneumatic tubes. The dynamics of these pneumatic tubes can be sufficiently represented by an approximate transfer function with time delay model as follows:

$$H_1(s) = \frac{K(s+a)}{s+b} e^{-T_D s} \tag{54}$$

The transfer function given in (54) relates the estimated chamber pressures to the pressures measured by distant pressure transducers as follows:

$$\frac{P_{if}}{P_{im}} (i = 1,2) = H_1(s) \tag{55}$$

where P_{1f} and P_{2f} are estimated chamber pressures, and P_{1m} and P_{2m} are measured pressures.

The force feedback using estimated chamber pressures to implement force control is

$$F_{af} = P_{1f}A_1 - P_{2f}A_2 - P_a A_r \tag{56}$$

Given an accurate pneumatic tube model within range of operating conditions, we should expect to have

$$P_{1f} = P_1 \tag{57}$$

$$P_{2f} = P_2 \tag{58}$$

Using (38) and (57) in (31), and (39) and (58) in (32), we have

$$\dot{P}_{1f} = \frac{\gamma RT}{V_1} \emptyset_1 \overline{A_{v,1}} \psi_1 \left(P_{u,1}, P_{d,1}\right) - \alpha \frac{P_{1f} A_1}{V_1} \dot{x}_p \tag{59}$$

$$\dot{P}_{2f} = \frac{\gamma RT}{V_2} \emptyset_2 \overline{A_{v,2}} \psi_2 \left(P_{u,2}, P_{d,2}\right) + \alpha \frac{P_{2f} A_2}{V_2} \dot{x}_p \tag{60}$$

Differentiating (56) twice to get

$$\ddot{F}_{af} = \ddot{P}_{1f} A_1 - \ddot{P}_{2f} A_2 \tag{61}$$

Differentiating (59) and (60) to get

$$\ddot{P}_{1f} = \frac{1}{V_1}\left[-(1+\alpha)\dot{x}_p \dot{P}_{1f} A_1 - \alpha \ddot{x}_p P_{1f} A_1 + \gamma RT \emptyset_1 \left(\psi_1 \dot{\overline{A_{v,1}}} + \dot{\psi}_1 \overline{A_{v,1}}\right)\right] \tag{62}$$

$$\ddot{P}_{2f} = \frac{1}{V_2}\left[(1+\alpha)\dot{x}_p \dot{P}_{2f} A_2 + \alpha \ddot{x}_p P_{2f} A_2 + \gamma RT \emptyset_2 \left(\psi_2 \dot{\overline{A_{v,2}}} + \dot{\psi}_2 \overline{A_{v,2}}\right)\right] \tag{63}$$

In (62) and (63), $\dot{\psi}_1$ and $\dot{\psi}_2$ are the time-derivatives of flow functions and can be determined by the following equations with $i = 1,2$:

$$\dot{\psi}_i(P_s, \overline{P_{if}})$$

$$= \begin{cases} 0 & , \dfrac{\overline{P_{if}}}{P_s} \leq P_{cr} \text{ (chocked)} \\ B_1 \left[\dfrac{\gamma - 1}{2\sqrt{1 - \left(\dfrac{\overline{P_{if}}}{P_s}\right)^{\frac{\gamma-1}{\gamma}}}} - \left(\dfrac{\overline{P_{if}}}{P_s}\right)^{\frac{1-\gamma}{\gamma}} \sqrt{1 - \left(\dfrac{\overline{P_{if}}}{P_s}\right)^{\frac{\gamma-1}{\gamma}}} \right] \dot{\overline{P_{if}}}, & \dfrac{\overline{P_{if}}}{P_s} > P_{cr} \text{(unchocked)} \end{cases} \tag{64}$$

$$\dot{\psi}_i(\overline{P_{if}}, P_a)$$

$$= \begin{cases} B_2 \cdot \dot{\overline{P_{if}}} & , \dfrac{P_a}{\overline{P_{if}}} \le P_{cr} \text{ (chocked)} \\ B_3 \left[\dfrac{P_a}{2\overline{P_{if}} \sqrt{1 - \left(\dfrac{P_a}{\overline{P_{if}}} \right)^{\frac{\gamma-1}{\gamma}}}} + \dfrac{P_a}{\overline{P_{if}}} \sqrt{1 - \left(\dfrac{P_a}{\overline{P_{if}}} \right)^{\frac{\gamma-1}{\gamma}}} \right] \dot{\overline{P_{if}}}, \dfrac{P_a}{\overline{P_{if}}} > P_{cr} \text{(unchocked)} \end{cases} \tag{65}$$

where $\overline{P_{if}} (i = 1,2)$ are the delayed estimated chamber pressures. Also

$$B_1 = -C_d \sqrt{\frac{2}{\gamma RT(\gamma - 1)}} \tag{66}$$

$$B_2 = \frac{C_d}{\sqrt{T}} \sqrt{\frac{\gamma}{R} \left(\frac{2}{\gamma + 1} \right)^{\frac{\gamma+1}{\gamma-1}}} \tag{67}$$

$$B_3 = C_d \sqrt{\frac{2(\gamma - 1)}{\gamma RT}} \tag{68}$$

Inserting (62) and (63) into (61), and considering (42),

$$\begin{aligned} \ddot{F}_{af} = &-\alpha \dddot{x}_p \left(\frac{P_{1f} {A_1}^2}{V_1} + \frac{P_{2f} {A_2}^2}{V_2} \right) - \ddot{x}_p (1 + \alpha) \left(\frac{\dot{P}_{1f} {A_1}^2}{V_1} + \frac{\dot{P}_{2f} {A_2}^2}{V_2} \right) \\ &+ \gamma RT \left(\frac{A_1 \emptyset_1 \psi_1}{V_1} + \frac{A_2 \emptyset_2 \psi_2}{V_2} \right) \dot{\overline{A_v}} + \gamma RT \left(\frac{A_1 \emptyset_1 \dot{\psi}_1}{V_1} + \frac{A_2 \emptyset_2 \dot{\psi}_2}{V_2} \right) \overline{A_v} \end{aligned} \tag{69}$$

Introducing K_1, K_2, C_1 and C_2 to simplify (69),

$$\ddot{F}_{af} = -K_1 \dddot{x}_p - K_2 \ddot{x}_p (1 + \alpha) + (C_1 \psi_1 + C_2 \psi_2) \dot{\overline{A_v}} + \left(C_1 \dot{\psi}_1 + C_2 \dot{\psi}_2 \right) \overline{A_v} \tag{70}$$

where

$$C_1 = \gamma RT \frac{A_1}{V_1} \emptyset_1 \tag{71}$$

$$C_2 = \gamma RT \frac{A_2}{V_2} \emptyset_2 \tag{72}$$

$$K_1 = \alpha \left(\frac{P_{1f} {A_1}^2}{V_1} + \frac{P_{2f} {A_2}^2}{V_2} \right) \tag{73}$$

$$K_2 = \left(\frac{\dot{P}_{1f} {A_1}^2}{V_1} + \frac{\dot{P}_{2f} {A_2}^2}{V_2} \right) \tag{74}$$

Introducing terms D_1 and D_2 for simplification, we get

$$\ddot{F}_{af} = -K_1 \dddot{x}_p - K_2 \ddot{x}_p (1 + \alpha) + D_1 \dot{\overline{A_v}} + D_2 \overline{A_v} \tag{75}$$

where

$$D_1 = C_1 \psi_1 + C_2 \psi_2 \tag{76}$$

$$D_2 = C_1 \dot{\psi}_1 + C_2 \dot{\psi}_2 \tag{77}$$

Differentiating (53)

$$\dot{\overline{A_v}} = w \dot{\bar{x}}_s \tag{78}$$

Using (51), (53) and (78), system dynamics given in (75) can alternatively be written as

$$\ddot{F}_{af} = -K_1 \dddot{x}_p - K_2 \ddot{x}_p (1 + \alpha) - \left(\frac{D_1}{\tau_v} - D_2 \right) w \bar{x}_s + \frac{w K_v D_1}{\tau_v} u \tag{79}$$

System dynamics given in (79) can be re-written as

$$\ddot{F}_{af} = f\left(x_p, P_{1f}, P_{2f}, \overline{P_{1f}}, \overline{P_{2f}}, \bar{x}_s\right) + b(x_p, P_{1f}, P_{2f}, \overline{P_{1f}}, \overline{P_{2f}}) u \tag{80}$$

where $f\left(x_p, P_{1f}, P_{2f}, \overline{P_{1f}}, \overline{P_{2f}}, \bar{x}_s\right)$ is the dynamic function of the system and is given by

$$f\left(x_p, P_{1f}, P_{2f}, \overline{P_{1f}}, \overline{P_{2f}}, \bar{x}_s\right) = -K_1 \dddot{x}_p - K_2 \ddot{x}_p (1 + \alpha) - \left(\frac{D_1}{\tau_v} - D_2 \right) w \bar{x}_s \tag{81}$$

and $b(x_p, P_{1f}, P_{2f}, \overline{P_{1f}}, \overline{P_{2f}})$ is the control gain function which is

$$b(x_p, P_{1f}, P_{2f}, \overline{P_{1f}}, \overline{P_{2f}}) = \frac{w K_v D_1}{\tau_v} \tag{82}$$

Equation (82) shows that the actuator described in Section 5.1 is a second order system.

5.3 Linear and Proposed Nonlinear Integral Sliding Surfaces

Unlike conventional linear sliding surface, the linear integral sliding surface [Slotine & Li, 1991] does not have a problem of reaching phase in case of initial errors. Therefore, the controller built upon the linear integral sliding surface offers robustness against matched uncertainties from the beginning of the system response. For a second order system like the one under consideration, the surface can be defined as S_1 in state-space $\mathbb{R}^n$ by the scalar equation $s_1 = 0$, where

$$s_1 = \dot{e} + 2\lambda e + \lambda^2 \int e\, dt - \dot{e}(0) - 2\lambda e(0) \tag{83}$$

In (83), λ is a strictly positive constant and is called controller bandwidth, and e is the tracking error in the controlled variable. Indeed, $s_1 \equiv 0$ represents a linear integro-differential equation whose solution yields

$$e(t) = (e(0) + [\lambda e(0) + \dot{e}(0)]t)\exp(-\lambda t) \tag{84}$$

Equation (84) shows the following:

- For zero initial conditions, $s_1 \equiv 0$ has a unique solution, $e \equiv 0$.
- For non-zero initial conditions, $s_1 \equiv 0$ has a solution which converges to $e \equiv 0$ after transient in finite time t for practical purposes depending upon λ.

Therefore, the problem of keeping $e \equiv 0$ is equivalent to that of holding on to the surface S_1 for all $t > 0$.

To track the integral sliding surface i.e. $s_1 = 0$, the controller must enforce a relationship:

$$\dot{e} = -2\lambda e - \lambda^2 \int e\, dt + \dot{e}(0) + 2\lambda e(0) \tag{85}$$

From (85), it is clear that the change of error enforced by the controller has a greater weight of accumulated errors than the error itself for any value of λ greater than 2, which may cause the system to overshoot in case of large initial transient errors. To solve this problem, the controller bandwidth can be reduced. However, this will result in an exceedingly slow system response with long rise and settling times. Furthermore, for a desired trajectory having multiple steps, linear integral sliding surface having a scalar s_1 given in (83) is not sufficient to eliminate the reaching phase. At the onset of each step, the reaching phase exists and the controller loses robustness against matched uncertainties until the sliding mode is established again. To ensure robustness against matched uncertainties throughout the system response despite multiple steps in the desired trajectory, the surface needs a slight modification in which scalar s_1 gets updated at the onset of each step (nth) and is given by

$$s_1 = \dot{e} + 2\lambda e + \lambda^2 \int e\, dt - \dot{e}(0) - 2\lambda e(0) - 2\lambda \sum_{i=1}^{n} e(t_i)\,, \quad n = 1,2,3, \ldots \tag{86}$$

where t_i is the time at which the ith step in the desired trajectory begins.

For a system tracking the desired trajectory accurately before the onset of ith step,

$$e(t_i) = y_d(t_i^{-}) - y_d(t_i^{+}) \tag{87}$$

where y_d is any desired trajectory.

To eliminate overshoot in case of large initial errors and multiple steps in the desired trajectory, this thesis proposes a novel nonlinear integral sliding surface. The proposed sliding surface can be constructed by adding a nonlinear function of the error to the linear integral sliding surface given in (86). The nonlinear function gets updated at the onset of each step (nth) in the desired trajectory and is given by

$$\mathrm{h}(e) = \mathrm{f}(e) - \mathrm{f}\big(e(0)\big) - \sum_{i=1}^{n} \mathrm{f}(e(t_i)), \qquad n = 1,2,3,\ldots \tag{88}$$

where

$$\mathrm{f}(e) = \begin{cases} \frac{c_1}{2}e + \frac{c_1 c_2}{2\pi} sin\left(\frac{\pi e}{c_2}\right), & |e| \le c_2 \\ \frac{c_1 c_2}{2}, & e > c_2 \\ -\frac{c_1 c_2}{2}, & e < -c_2 \end{cases} \tag{89}$$

In (89), c_1 and c_2 are strictly positive design parameters. The plot of $\mathrm{f}(e)$ is shown in Figure 5.2.

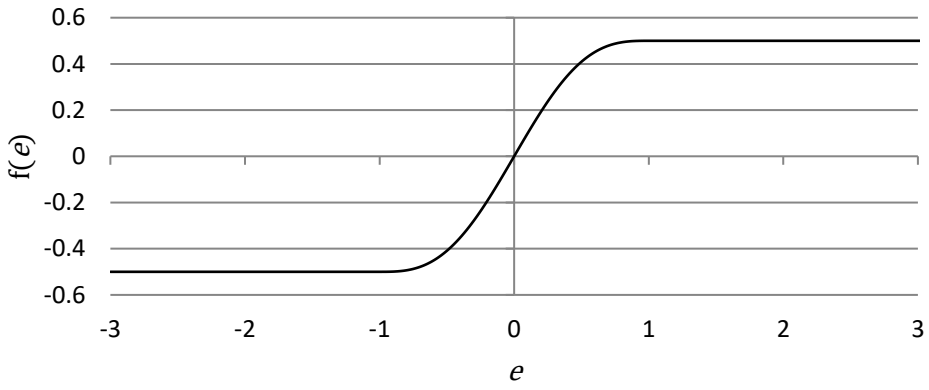

Figure 5.2 Nonlinear function f(e) for proposed nonlinear integral sliding surface ($c_1 = c_2 = 1$)

For a second order system, the proposed surface can be represented as S_2 in state-space $\mathbb{R}^n$ by the scalar equation $s_2 = 0$, where s_2 gets updated at the onset of each step (nth) in the desired trajectory and is given by

$$s_2 = \dot{e} + 2\lambda e + \lambda^2 \int e\, dt - \dot{e}(0) - 2\lambda e(0) - 2\lambda \sum_{i=1}^{n} e(t_i) + \mathrm{h}(e), \qquad n = 1,2,3,\ldots \tag{90}$$

Inserting (88) into (90), we have

$$s_2 = \dot{e} + 2\lambda e + \lambda^2 \int e\, dt - \dot{e}(0) - 2\lambda e(0) - 2\lambda \sum_{i=1}^{n} e(t_i) + \mathrm{f}(e) - \mathrm{f}(e(0)) - \sum_{i=1}^{n} \mathrm{f}(e(t_{i)}), \qquad n = 1,2,3,\ldots \tag{91}$$

From (91), it is clear that the proposed surface does not have a reaching phase despite initial errors and multiple steps in the desired trajectory. Therefore, the robustness against matched uncertainties is guaranteed throughout the system response.

To keep on tracking $s_2 = 0$, the controller must enforce the following sliding mode dynamics:

$$\dot{s}_2 = 0 \tag{92}$$

where $\dot{s}_2$ can be determined by taking the time derivative of (91) as follows:

$$\dot{s}_2 = \ddot{e} + \left(2\lambda + \frac{\partial \mathrm{f}}{\partial e}\right)\dot{e} + \lambda^2 e \tag{93}$$

which shows that the proposed nonlinear integral sliding surface introduces a nonlinear function of error to the weight of the derivative component in the sliding mode dynamics enforced by the controller. This nonlinear function can be determined by taking the partial derivative of (89) with respect to error as follows:

$$\frac{\partial \mathrm{f}}{\partial e} = \begin{cases} \frac{c_1}{2} + \frac{c_1}{2} cos\left(\frac{\pi e}{c_2}\right), & |e| \leq c_2 \\ 0, & |e| > c_2 \end{cases} \tag{94}$$

Equation (94) shows that the nonlinear function introduced by the proposed sliding surface to the weight of the derivative component in sliding mode dynamics is zero for errors larger than c_2 on both sides of the desired trajectory. It makes the on-surface dynamics behave similar to those of linear integral sliding surface. For transient errors less than c_2 on both sides of the desired trajectory, the nonlinear function introduced to the weight of the derivative component increases as the transient error approaches smaller values and vice versa. In other words, the controller offers variable damping during the system response that changes from low to high as the transient error approaches small values and vice versa. This feature of the proposed nonlinear integral sliding surface can be exploited to improve the transient response of the system i.e. no overshoot while maintaining good rise and settling times. The nonlinear function introduced to the weight of the derivative component responsible for offering variable damping during the transient response is shown in Figure 5.3.

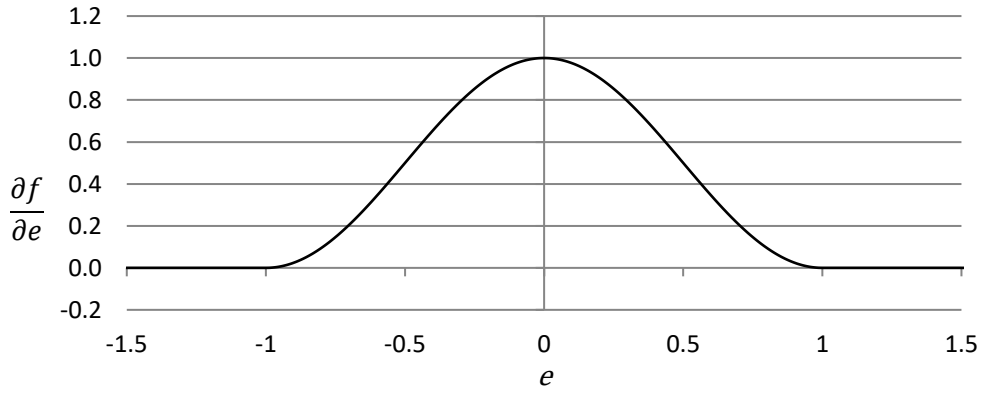

Figure 5.3 Nonlinear function introduced to the weight of the derivative component in sliding mode dynamics by the proposed nonlinear integral sliding surface for variable damping during the system response ($c_1 = c_2 = 1$)

To verify the characteristics of the proposed nonlinear integral sliding surface of having no reaching phase and providing robustness throughout the system response despite initial errors and multiple steps in the desired trajectory, we consider the following second-order system subjected to a nonlinear disturbance in the control input channel:

$$a\ddot{y}(t) + b\dot{y}(t) + cy(t) = u(t) + msiny(t) \tag{95}$$

where $a = 1, b = 3, c = 2, m = 0.1$, and u is the control input.

The system initial conditions are $y(0) = 0.1, \dot{y}(0) = 0.05$. The desired trajectory of $y(t)$ has multiple steps and is shown in Figure 5.4. In state-space form, the system can be represented by

$$\dot{x}_1(t) = \dot{y}(t) = x_2(t) \tag{96}$$

$$\dot{x}_2(t) = \ddot{y}(t) = -\frac{c}{a}x_1(t) - \frac{b}{a}x_2(t) + \frac{1}{a}\Big(u(t) + msin\big(x_1(t)\big)\Big) \tag{97}$$

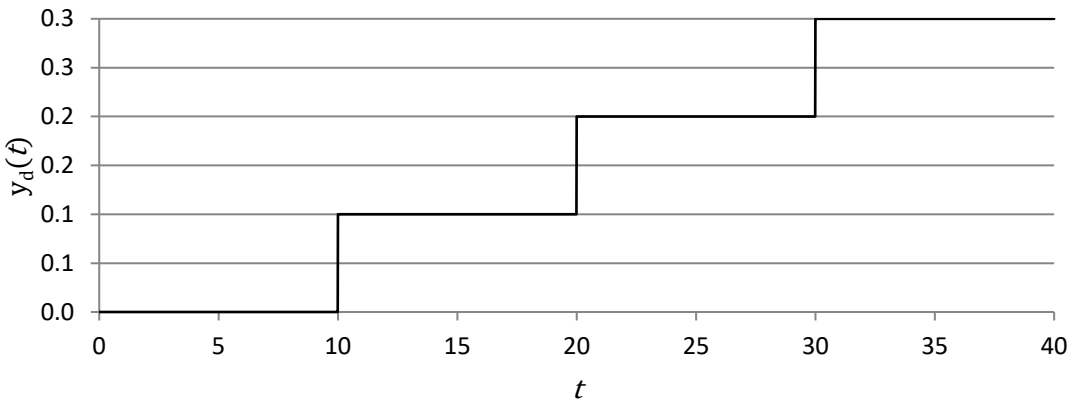

Figure 5.4 Desired trajectory for $y(t)$

For $c_2 < e(0) = 0.1$, equation (91) becomes

$$s_2 = \begin{cases} \dot{e} + 2\lambda e + \lambda^2 \int e\,dt - 0.05 - 0.2\lambda + \mathrm{f}(e) - \mathrm{f}(0.1), & 0 \le t < 10 \\ \dot{e} + 2\lambda e + \lambda^2 \int e\,dt - 0.05 + \mathrm{f}(e), & 10 \le t < 20 \\ \dot{e} + 2\lambda e + \lambda^2 \int e\,dt - 0.05 + 0.2\lambda + \mathrm{f}(e) + \mathrm{f}(0.1), & 20 \le t < 30 \\ \dot{e} + 2\lambda e + \lambda^2 \int e\,dt - 0.05 + 0.4\lambda + \mathrm{f}(e) + 2\mathrm{f}(0.1), & 30 \le t \le 40 \end{cases} \quad (98)$$

Taking time derivative of (98), we have

$$\dot{s}_2 = \ddot{e} + \left(2\lambda + \frac{\partial \mathrm{f}}{\partial e}\right)\dot{e} + \lambda^2 e = \ddot{y} + \left(2\lambda + \frac{\partial \mathrm{f}}{\partial e}\right)\dot{y} + \lambda^2 e \quad (99)$$

Inserting (97) into (99) and ignoring the disturbance in the control input channel,

$$\dot{s}_2 = -\frac{c}{a}x_1 - \frac{b}{a}x_2 + \frac{1}{a}u + \left(2\lambda + \frac{\partial \mathrm{f}}{\partial e}\right)\dot{y} + \lambda^2 e \quad (100)$$

Substituting (100) in (92), we obtain

$$u = \frac{c}{a}x_1 + \frac{b}{a}x_2 - \left(2\lambda + \frac{\partial \mathrm{f}}{\partial e}\right)\dot{y} - \lambda^2 e \quad (101)$$

To compensate for modeling uncertainties, the robust component can be introduced to the control input as follows:

$$u = \begin{cases} \frac{c}{a}x_1 + \frac{b}{a}x_2 - \left(2\lambda + \frac{\partial \mathrm{f}}{\partial e}\right)\dot{y} - \lambda^2 e - G \cdot \frac{s_2}{\varphi} & |s_2| \le \varphi \\ \frac{c}{a}x_1 + \frac{b}{a}x_2 - \left(2\lambda + \frac{\partial \mathrm{f}}{\partial e}\right)\dot{y} - \lambda^2 e - G.sgn(s_2) & |s_2| > \varphi \end{cases} \quad (102)$$

where G is the robustness parameter, and φ is the boundary layer thickness.

Simulation results of the second-order system represented in (95) while tracking $y(t)$ are shown in Figure 5.5. The results reveal that the proposed sliding surface does not have a reaching phase despite initial errors and multiple steps in the desired trajectory. The controller designed using the proposed sliding surface offers robustness

to matched uncertainty throughout the system response. The effect of a nonlinear disturbance in control input channel is completely eliminated.

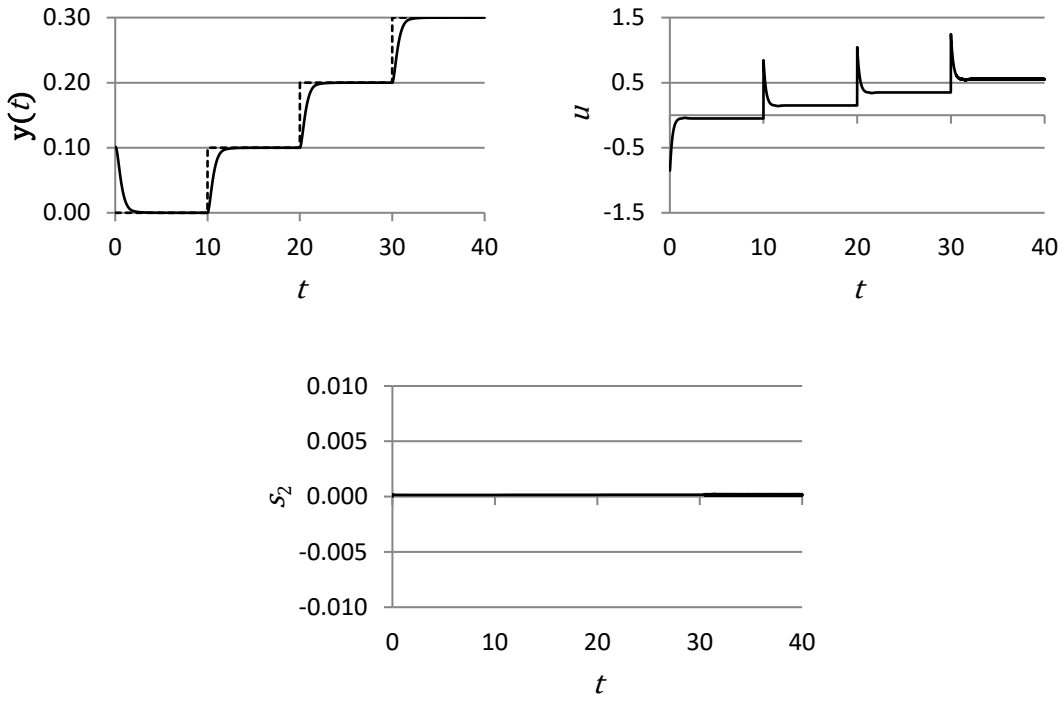

Figure 5.5 Simulation results of the second-order system while tracking y(t) with sliding mode controller based on the proposed nonlinear integral sliding surface ($G = 0.05, \lambda = 3, c_1 = 2, c_2 = 0.01, \varphi = 0.0001$)

5.4 Control Laws

This section derives the control laws based on linear and proposed nonlinear integral sliding surfaces for the actuator described in Sections 5.1 and 5.2.

To make sure that all system states converge to equilibrium, we set $\dot{s}_1$ and $\dot{s}_2$ equal to zero which yields

$$\ddot{e} + (2\lambda + c_1)\dot{e} + \lambda^2 e = 0 \tag{103}$$

$$\ddot{e} + \left(2\lambda + \frac{\partial \mathrm{f}}{\partial e}\right)\dot{e} + \lambda^2 e = 0 \tag{104}$$

The error is

$$e = F_{af} - F_r \tag{105}$$

where F_r is the desired actuating force, and F_{af} is the actual actuating force.

Inserting (105) into (103) and (104), we have

$$\ddot{F}_{af} - \ddot{F}_r + 2\lambda\dot{e} + \lambda^2 e = 0 \tag{106}$$

$$\ddot{F}_{af} - \ddot{F}_r + \left(2\lambda + \frac{\partial \mathrm{f}}{\partial e}\right)\dot{e} + \lambda^2 e = 0 \tag{107}$$

Substituting (79) in (106) and (107), we obtain the equivalent components of sliding mode control laws based on the linear integral sliding surface (LISS) and the proposed nonlinear integral sliding surface (NLISS) as follows:

$$u_{eq\_LISS} = \frac{\tau_v}{wK_vD_1}\left[\ddot{F}_r + K_1\dddot{x}_p + K_2\ddot{x}_p(1+\alpha) + \left(\frac{D_1}{\tau_v} - D_2\right)w\dot{\bar{x}}_s - 2\lambda\dot{e} - \lambda^2 e\right] \tag{108}$$

$$\begin{aligned} u_{eq\_NLISS} = \frac{\tau_v}{wK_vD_1}\Bigg[&\ddot{F}_r + K_1\dddot{x}_p + K_2\ddot{x}_p(1+\alpha) + \left(\frac{D_1}{\tau_v} - D_2\right)w\dot{\bar{x}}_s \\ &- \left(2\lambda + \frac{\partial \mathrm{f}}{\partial e}\right)\dot{e} - \lambda^2 e\Bigg] \end{aligned} \tag{109}$$

To compensate for the modeling uncertainties, the robust component of the control signal is now introduced as follows:

$$u_{LISS} = \begin{cases} \frac{\tau_v}{wK_vD_1}\left(\ddot{F}_r + K_1\dddot{x}_p + K_2\ddot{x}_p(1+\alpha) + \left(\frac{D_1}{\tau_v} - D_2\right)w\dot{\bar{x}}_s - 2\lambda\dot{e} - \lambda^2 e - G\cdot\frac{s_1}{\varphi}\right) & |s_1| \le \varphi \\ \frac{\tau_v}{wK_vD_1}\left(\ddot{F}_r + K_1\dddot{x}_p + K_2\ddot{x}_p(1+\alpha) + \left(\frac{D_1}{\tau_v} - D_2\right)w\dot{\bar{x}}_s - 2\lambda\dot{e} - \lambda^2 e - G.sgn(s_1)\right) & |s_1| > \varphi \end{cases} \tag{110}$$

$$u_{NLISS} = \begin{cases} \frac{\tau_v}{wK_vD_1}\left(\ddot{F}_r + K_1\dddot{x}_p + K_2\ddot{x}_p(1+\alpha) + \left(\frac{D_1}{\tau_v} - D_2\right)w\dot{\bar{x}}_s - \left(2\lambda + \frac{\partial \mathrm{f}}{\partial e}\right)\dot{e} - \lambda^2 e - G\cdot\frac{s_2}{\varphi}\right) & |s_2| \le \varphi \\ \frac{\tau_v}{wK_vD_1}\left(\ddot{F}_r + K_1\dddot{x}_p + K_2\ddot{x}_p(1+\alpha) + \left(\frac{D_1}{\tau_v} - D_2\right)w\dot{\bar{x}}_s - \left(2\lambda + \frac{\partial \mathrm{f}}{\partial e}\right)\dot{e} - \lambda^2 e - G.sgn(s_2)\right) & |s_2| > \varphi \end{cases} \tag{111}$$

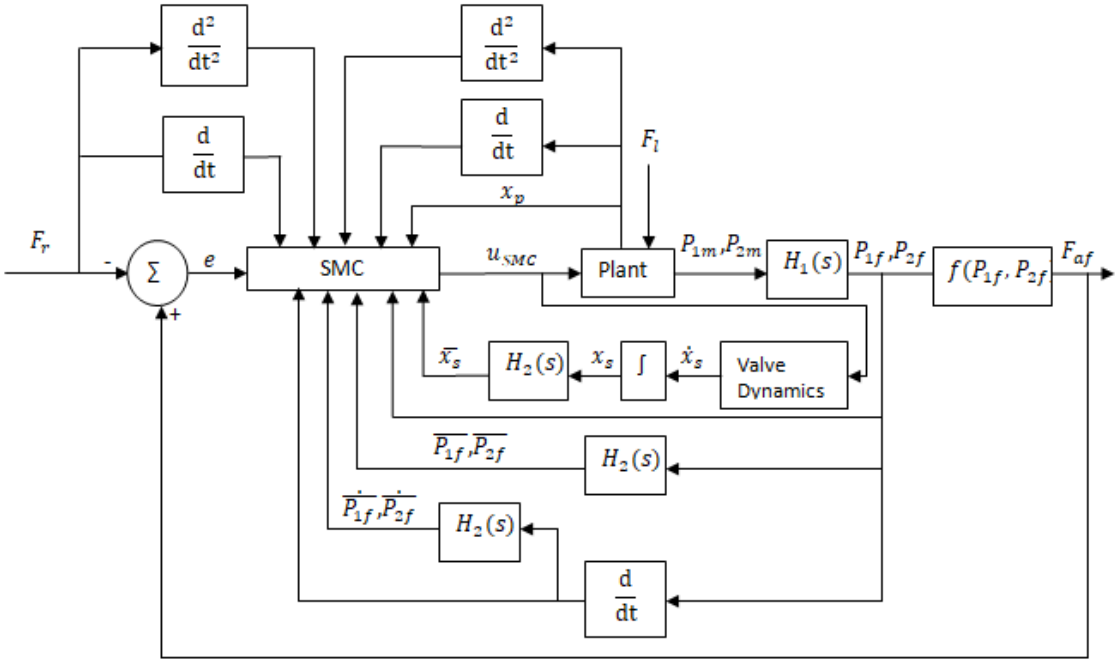

Figure 5.6 Schematic for implementation of sliding mode controllers based on linear and proposed nonlinear integral sliding surfaces

The sliding mode control laws presented in (110) and (111) have both delayed and undelayed estimated chamber pressure terms and their derivatives. The delayed estimated chamber pressure terms and their derivatives are contributed by flow functions and can be determined by passing the estimated chamber pressures and their derivatives through a filter having a transfer function

$$H_2(s) = \frac{1}{\frac{T_D{}^2}{2}s^2 + T_D s + 1} \tag{112}$$

The delayed spool displacement term present in control laws cannot be measured. Therefore, the spool displacement is computed using numerical integration and then time-delayed with the help of (112) for use in control laws. To facilitate understanding, the schematic for implementation of sliding mode controllers based on linear and proposed nonlinear integral sliding surfaces is shown in Figure 5.6.

5.5 Stability Analysis

This section examines the stability of the proposed modified integral sliding mode control using the Lyapunov stability criterion.

The dynamic function $f\left(x_p, P_{1f}, P_{2f}, \overline{P_{1f}}, \overline{P_{2f}}, \bar{x_s}\right)$ can be estimated as $\hat{f}\left(x_p, P_{1f}, P_{2f}, \overline{P_{1f}}, \overline{P_{2f}}, \bar{x_s}\right)$ and the estimation error is bounded such that

$$\left|\hat{f} - f\right| \leq F \tag{113}$$

Furthermore, the control gain $b\left(x_p, P_{1f}, P_{2f}, \overline{P_{1f}}, \overline{P_{2f}}\right)$ is bounded such that

$$0 < b_{min} \leq b \leq b_{max} \tag{114}$$

It is reasonable to choose estimated control gain $\hat{b}\left(x_p, P_{1f}, P_{2f}, \overline{P_{1f}}, \overline{P_{2f}}\right)$ to be the geometric mean of above-mentioned bounds i.e.,

$$\hat{b} = \sqrt{b_{max} b_{min}} \tag{115}$$

Bounds given in (114) can also be written as

$$\beta^{-1} \leq \frac{b}{\hat{b}} \leq \beta \tag{116}$$

where

$$\beta = \sqrt{\frac{b_{max}}{b_{min}}} \tag{117}$$

Choosing the Lyapunov function candidate

$$V = \frac{1}{2} {s_2}^2 \tag{118}$$

Taking time derivative of (118),

$$\dot{V} = s_2 \dot{s_2} \tag{119}$$

Substituting (105) in (93), we have

$$\dot{s}_2 = \ddot{F}_{af} - \ddot{F}_r + \left(2\lambda + \frac{\partial \mathrm{f}}{\partial e}\right)\dot{e} + \lambda^2 e \tag{120}$$

Inserting (80) in (120), we obtain

$$\dot{s}_2 = f + bu - \ddot{F}_r + \left(2\lambda + \frac{\partial \mathrm{f}}{\partial e}\right)\dot{e} + \lambda^2 e \tag{121}$$

Substituting (81) and (82) into (109) results in

$$u_{eq} = \frac{1}{\hat{b}}\left(\ddot{F}_r - \hat{f} - \left(2\lambda + \frac{\partial \mathrm{f}}{\partial e}\right)\dot{e} - \lambda^2 e\right) \tag{122}$$

Substituting (81), (82) and (109) in (112), we have

$$u = u_{eq} - \frac{G}{\hat{b}} sgn(s_2) \tag{123}$$

Substituting (122) in (123) and putting the result in (121), we obtain

$$\dot{s_2} = \left(f - \frac{b}{\hat{b}}\hat{f}\right) + \left(1 - \frac{b}{\hat{b}}\right)\left(-\ddot{F}_r + \left(2\lambda + \frac{\partial \mathrm{f}}{\partial e}\right)\dot{e} + \lambda^2 e\right) - \frac{b}{\hat{b}} G sgn(s_2) \tag{124}$$

Substituting (124) in (119) results in

$$\dot{V} = \left[\left(f - \frac{b}{\hat{b}}\hat{f}\right) + \left(1 - \frac{b}{\hat{b}}\right)\left(-\ddot{F}_r + \left(2\lambda + \frac{\partial \mathrm{f}}{\partial e}\right)\dot{e} + \lambda^2 e\right)\right] s_2 - \frac{b}{\hat{b}} G|s_2| \tag{125}$$

For $\dot{V}$ to be negative definite, the following inequality must hold:

$$G \geq \left|\left(\frac{\hat{b}}{b} f - \hat{f}\right) + \left(\frac{\hat{b}}{b} - 1\right)\left(-\ddot{F}_r + \left(2\lambda + \frac{\partial \mathrm{f}}{\partial e}\right)\dot{e} + \lambda^2 e\right)\right| + \frac{\hat{b}}{b}\eta \tag{126}$$

where η is strictly positive.

Since

$$f = \hat{f} + \left(f - \hat{f}\right) \tag{127}$$

Inequality (126) may be re-written as

$$G \geq \frac{\hat{b}}{b}\left(f - \hat{f}\right) + \frac{\hat{b}}{b}\eta + \left|\left(\frac{\hat{b}}{b} - 1\right)\right|\left|\hat{f} - \ddot{F}_r + \left(2\lambda + \frac{\partial \mathrm{f}}{\partial e}\right)\dot{e} + \lambda^2 e\right| \tag{128}$$

Substituting (122) in (128), we obtain

$$G \geq \frac{\hat{b}}{b}\left(f - \hat{f}\right) + \frac{\hat{b}}{b}\eta + \left|\left(\frac{\hat{b}}{b} - 1\right)\right| \left|\hat{b}u_{eq}\right| \tag{129}$$

Considering (113) and (116), inequality (129) can also be written as

$$G \geq \beta(F + \eta) + |(\beta - 1)|\left|\hat{b}u_{eq}\right| \tag{130}$$

Subject to inequality (130) satisfied, we have

$$\dot{V} \leq -\eta|S_1| \tag{131}$$

Inequality (131) shows that the sliding mode controller based on proposed nonlinear integral sliding surface is asymptotically stable as long as (130) is true.

5.6 Summary

System dynamics of a force-controlled pneumatic actuator with long transmission lines and indirect pressure measurements were presented, which showed that the actuator was a second-order, nonlinear system with input delay. The pneumatic tube was modeled as a first-order, linear transfer function with time delay to facilitate indirect measurements of cylinder pressures. For an improved transient response of the actuator, a nonlinear integral sliding surface was proposed. The proposed sliding surface was designed to enable sliding mode controller to offer variable damping during the system response. The surface was a linear integral sliding surface augmented by a nonlinear function of tracking error and did not have a reaching phase in case of initial errors and even when there were multiple steps in the desired trajectory. A full order sliding mode controller was designed for the actuator using the proposed nonlinear integral sliding surface. The controller had asymptotic stability for bounded uncertainties in control gain and system dynamic functions provided that a condition on

robustness parameter shown in (130) is satisfied. A sliding mode control law based on the linear integral sliding surface was also derived for the actuator for comparison.

Chapter 6

Performance Evaluation[6]

This chapter examines the performance of full order sliding mode controller based on the proposed nonlinear integral sliding surface for force control of a pneumatic actuator with long transmission lines and indirect pressure measurements, using simulation as well as experiments.

6.1 Simulation Studies

In simulation studies, system dynamics described in Section 5.2, sliding mode control laws explained in Section 5.4, and system parameters shown in Table 6.2 are used. Sliding mode control laws presented in (110-111) indicate that some parameters of the controllers need tuning for desired system responses. It is well- established that the performance of controllers depends heavily on values chosen for such parameters. Therefore, for comparing the performance of controllers in these simulation studies, such controller parameters are optimized using a low-cost globalized multimodal optimization algorithm called GBNM with deterministic restarts explained in Chapter 2

[6] A version of this chapter has been included in Butt, K., & Sepehri, N. (2018). A nonlinear integral sliding surface to improve the transient response of a force-controlled pneumatic actuator with long transmission lines. Manuscript submitted for publication.

as follows:

The algorithm controls the simulating model and steers the controller towards optimal parameters using the results from its logically guided iterative runs. To optimize the controller parameters for an improved transient response of the system with minimum possible overshoot and rise and settling times, the algorithm minimizes the following aggregated multi-objective function with bounds on controller parameters given in Table 6.1.

$$f(e)|_{(Controller\ Parameters)} = \int_0^T |e|\, dt + |e|_{t=t_p} \tag{132}$$

where T is the time span of the iterative run, and t_p is the time at which the maximum absolute of actual actuating force exists.

The 1st term of the objective function minimizes the rise and settling times while the 2nd term penalizes the overshoot in system response. The bounds on controller parameters define the search space for optimization and they are used as the convergence aspects of the algorithm with respect to system stability are not known. The parameters required to compute objective function are obtained from the system's simulated response when it is made to track bipolar square pulses shown in Figure 6.1 for 6 seconds. Bipolar square pulses are used as a test signal because the thesis focuses on the improvement of the transient response of the system when initial errors are large and there are multiple steps in the desired trajectory. The piston position is kept fixed during the iterative run of the simulating model for tuning to eliminate the uncertainty in external load which may misguide the optimization algorithm by causing the inconsistency in results on the same set of controller parameters. The optimized

parameters of both the controllers obtained using the tuning process, are listed in Table 6.1. These controllers' parameters are used for simulations presented in this chapter.

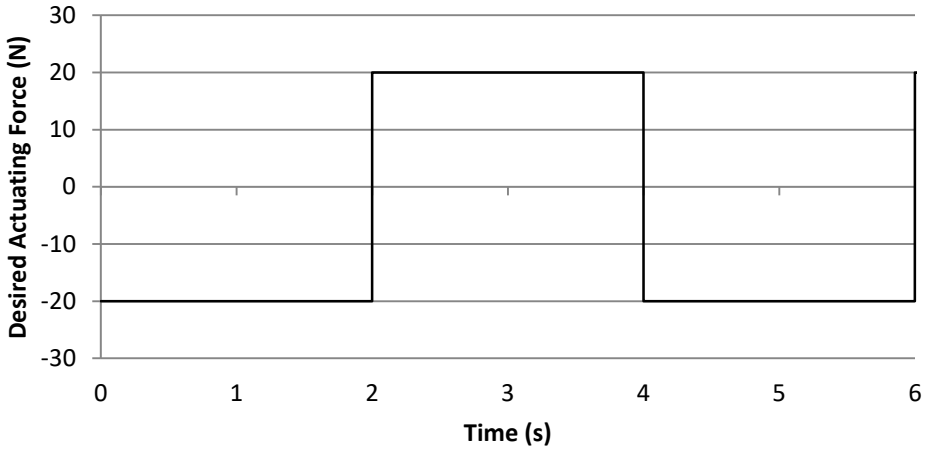

Figure 6.1 Test signal

TABLE 6.1 BOUNDS ON CONTROLLERS' PARAMETERS AND THEIR OPTIMIZED VALUES (SIMULATIONS)

Parameter	**Description**	**Bounds**		**Optimized Value**	**Unit**
		Minimum	**Maximum**		
LISS					
G	Robustness parameter	0	200	114.6567	N/s^2
λ	Controller bandwidth parameter	0	100	40.7603	rad/s
φ	Boundary layer thickness	10	10	10	N/s
NLISS					
G	Robustness parameter	0	200	184.886	N/s^2
λ	Controller bandwidth parameter	0	100	69.4918	rad/s
φ	Boundary layer thickness	10	10	10	N/s
c_1	Design parameter for proposed nonlinear integral sliding surface	0	500	206.696	rad/s
c_2	Design parameter for proposed nonlinear integral sliding surface	0	40	39.2847	N

The simulated system responses under the sliding mode controllers based on linear and proposed nonlinear integral sliding surfaces are shown in Figure 6.2. The system response under the controller based on linear integral sliding surface overshoots and has long settling time. On the other hand, it has absolutely no overshoot under the

controller based on the proposed nonlinear integral sliding surface. The system's rise times are almost identical in both cases.

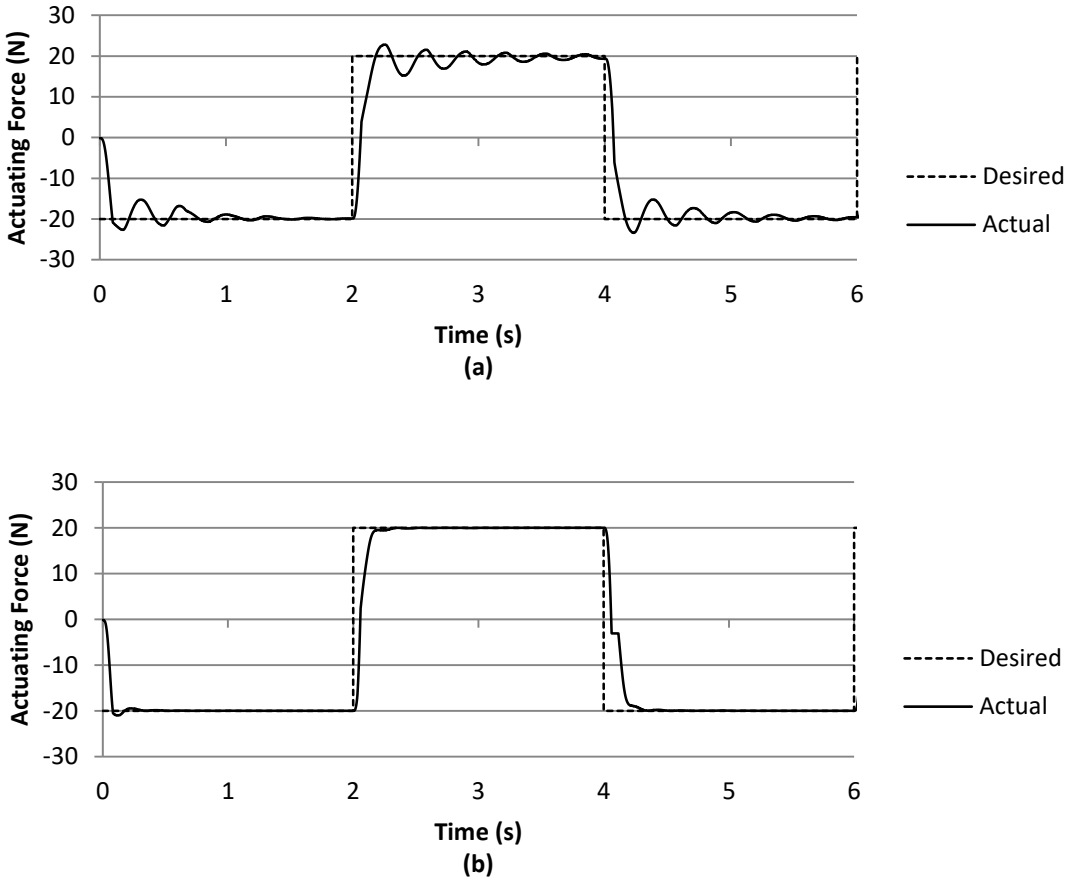

Figure 6.2 Simulation results of actuating force control using (a) LISS and (b) NLISS

Tracking errors in the system responses under the controllers examined in this chapter are also shown in Figure 6.3. The system does not approach steady state under the controller based on the linear integral sliding surface because of long settling time while under the controller based on the proposed nonlinear integral sliding surface, it approaches steady state with zero steady-state error.

The control signals and valve spool displacements for system responses shown in Figure 6.2 are presented in Figures 6.4 and 6.5, respectively. The control signals have

some spikes of +5V or -5V. These spikes occur when system requires large spool velocities to keep tracking the desired trajectory.

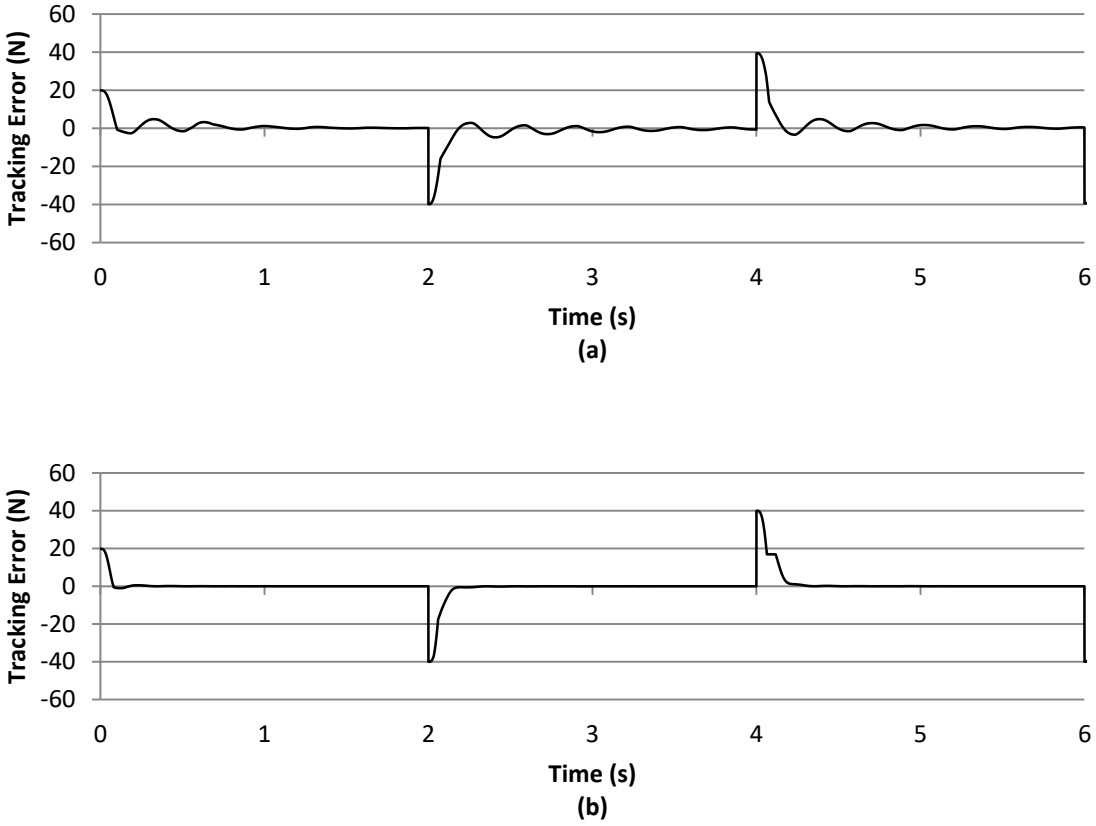

Figure 6.3 Tracking errors under (a) LISS and (b) NLISS (simulations)

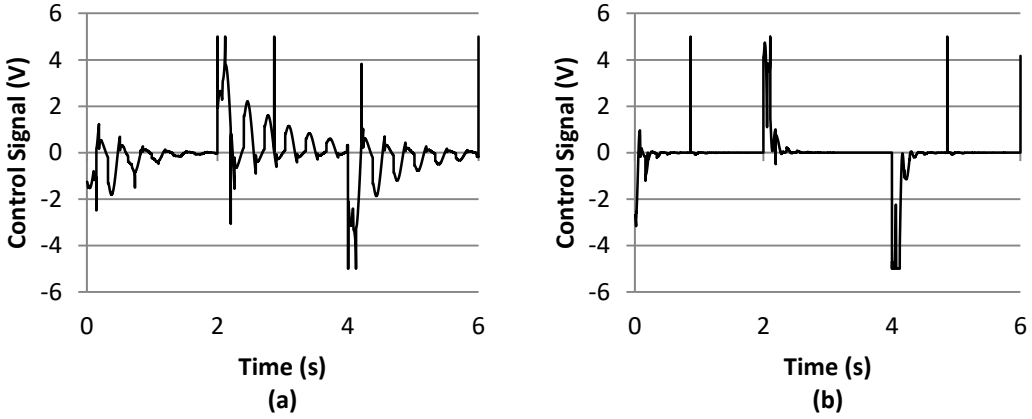

Figure 6.4 Control signals of (a) LISS and (b) NLISS (simulations)

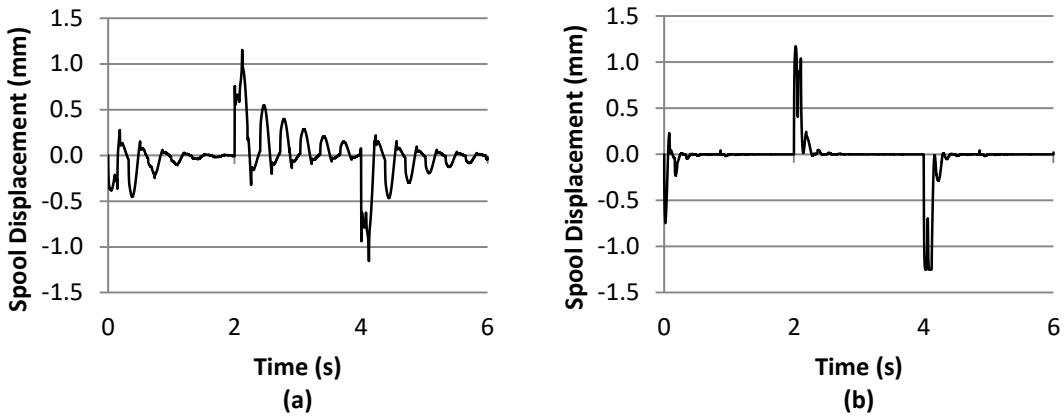

Figure 6.5 Valve spool displacements under (a) LISS and (b) NLISS (simulations)

6.2 Experimental Validation

6.2.1 Experimental Setup

To evaluate the performance of the controllers based on the linear and proposed nonlinear integral sliding surfaces, a purpose-built experimental setup shown in Figure 6.6 is developed. The schematic of the setup is shown in Figure 6.7. The parameters of the setup are listed in Table 6.2.

The setup contains a prototype MRI-compatible pneumatic gripper shown in Figure 6.8. The frame of the gripper is made of acrylic for MRI-compatibility and consists of machined plates for mounting other parts. The gripper provides support to the human grip through a fixed and a moving handle. A single rod, double acting, MRI-compatible cylinder is attached to the frame on one end and to the moving handle on the other end. The cylinder has anti-stiction properties and provides exceedingly low dynamic friction relatively independent on the velocity in the absence of side forces on the piston. To eliminate misalignment and the possibility of side forces on the piston, a

nonmagnetic misalignment coupler made of brass is provided between cylinder's rod and the moving handle. The coupler can compensate for misalignments up to 5°. The moving handle is mounted on a precision, frictionless, non-magnetic slide through an acrylic interface. The slide is fixed to the base plate of the frame. To eliminate the chances of piston banging against the glass bore of the cylinder, and to support the translational movement of the piston, a plate consisting of restriction guide for the moving handle is provided at the top of the frame. The fixed handle is mounted on the base plate and it passes through a hole in the plate having restriction guide. The plate having restriction guide also serves as a station on which wrist of the human subject rests during the device operation. The cylinder is connected to the 5/3 mass flow rate proportional valve having feedback pressure transducers at its outlets through 9m long pneumatic tubes of 2.184mm inner diameter. To estimate chamber pressures using readings from feedback pressure transducers, an approximate linear transfer function with time delay model of the pneumatic tube shown in (54) is used. The model has gain K, a pole b and a zero a. Using the MATLAB system identification toolbox, values of K, a and b are found to be 0.15, 63.12 and 9.86, respectively for a 9m long pneumatic tube of 2.184mm inner diameter. The setup contains monitoring pressure transducers, which are mounted on the cylinder with the help of very short pneumatic tubes. Measurements from these transducers are only used for presenting the outcome of experiments and are never used as feedback for control purposes. An air compressor along with air and mist filters, an electro-pneumatic regulator and an air reservoir is used to supply clean, dry, compressed and regulated air with minimized pressure fluctuations to the pneumatic components of the setup. To measure piton displacement,

an MRI-compatible, linear, optical, position sensor is mounted on the interface between the slide and the moving handle. The optical sensor uses a stretched optical film passing through it to generate an optical signal on piston movement. The film is stretched using acrylic clamps mounted on the base plate. The position sensor is connected to an optical-to-electrical module through a 10m long fiber optic cable to convert the optical signal into an electrical signal for feedback.

Figure 6.6 Experimental setup

The setup contains a data acquisition board that works as an interface between the pneumatic actuator and a target PC. The pressure transducers are connected to the analog input ports of the data acquisition board while the position sensor is connected to one of its encoder input ports. The command valve and the electro-pneumatic regulator are connected to the analog output ports of the board. The data acquisition board

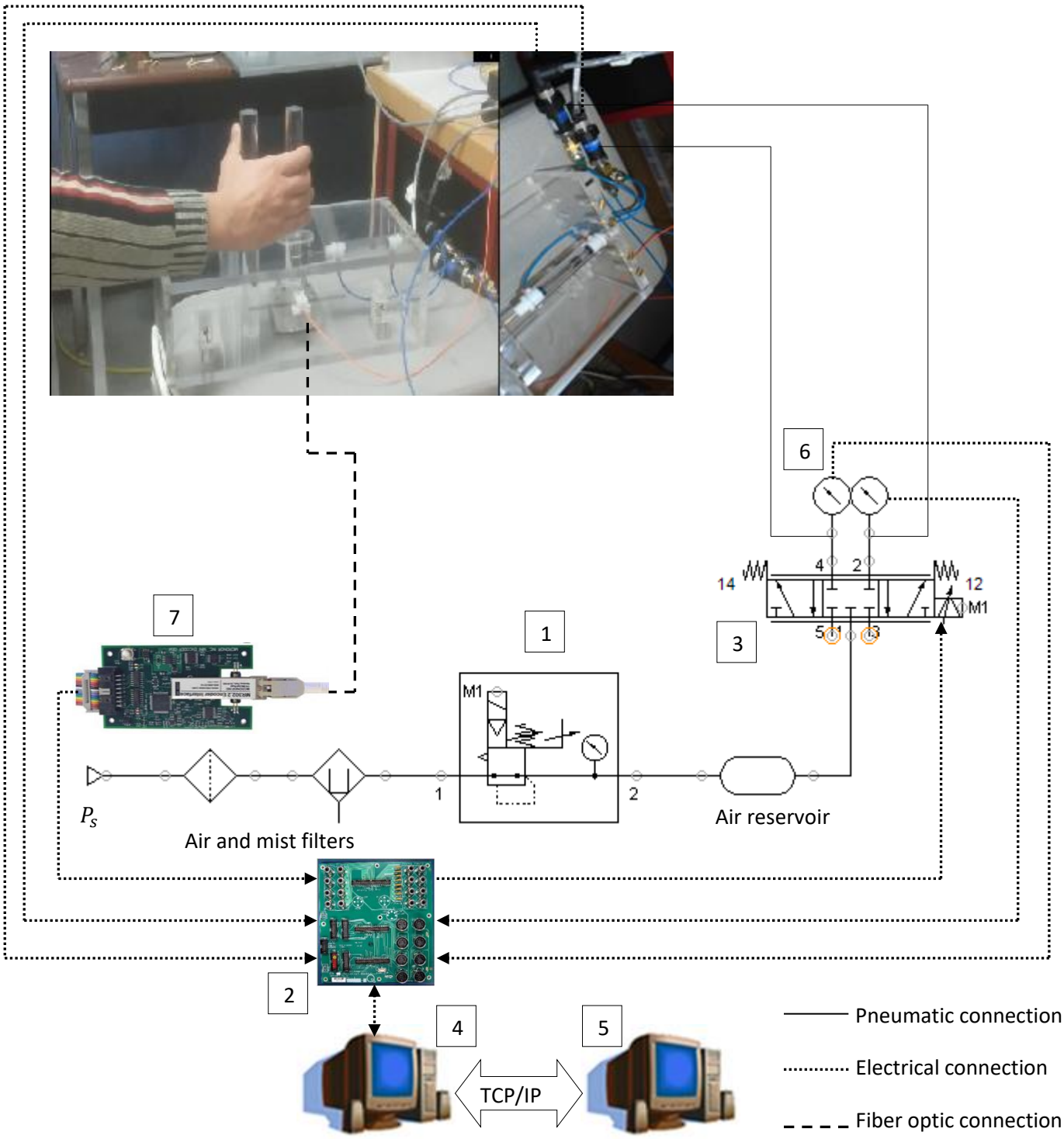

1 Pressure Regulator (SMC ITV1050-31N2CS4-Q)
2 Data Acquisition Board (QUANSER Q8)
3 5/3 Proportional Directional Valve (FESTO MYPE-5-1/8-LF-010-B)
4 Target PC (QNX Neutrino Real-Time Operating System)
5 Host PC (MICROSOFT Window Operating System)
6 Feedback Pressure Transducer (ASHCROFT T27M0210E200#G)
7 Optical to Electrical Module (MICRONOR MR302-2)

Figure 6.7 Schematic of the experimental setup

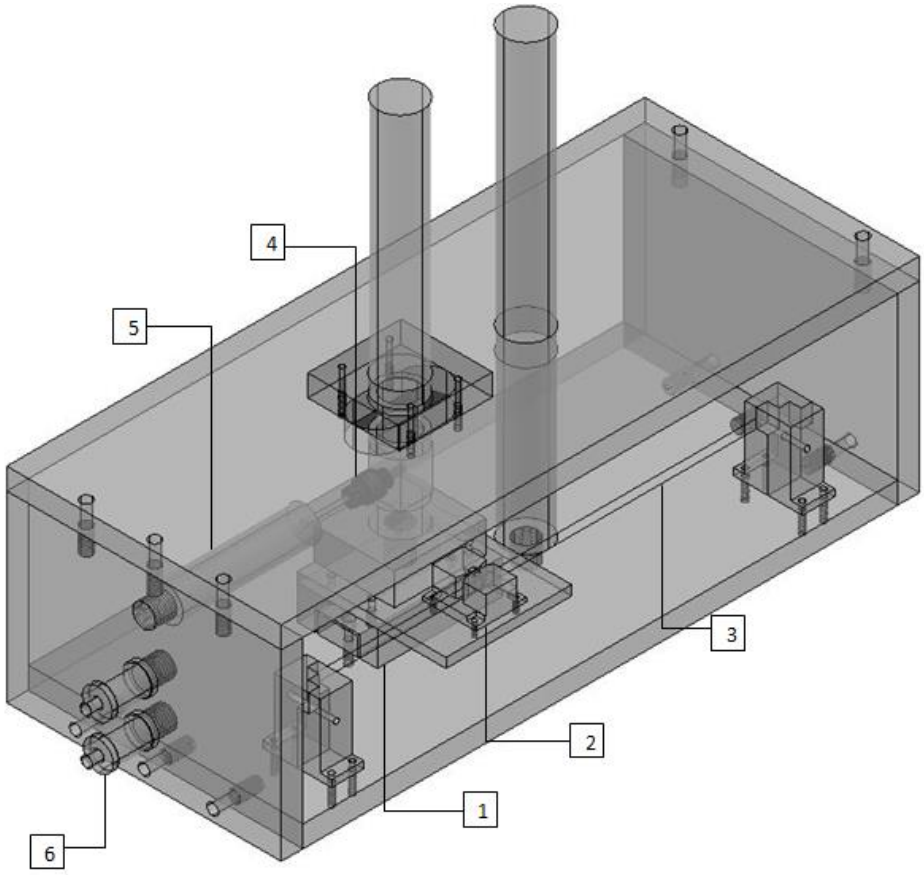

1 Frictionless Non-Magnetic Precision Slide (DELTRON S2-1.5-NMS)
2 MRI-Safe Linear Position Encoder (MICRONOR MR303-B400C10)
3 Incremental Encoder Film Strips (MICRONOR TD5334)
4 Brass Misalignment Coupler (with the specifications of McMASTER-CARR 7334K1)
5 MRI-Safe Anti-Stiction Pneumatic Cylinder (AIRPEL AC 13270-4)
6 Monitoring Pressure Transducer (ASHCROFT T27M0210E200#G)

Figure 6.8 Prototype pneumatic gripper

establishes a connection with the target PC through a PCI board. The target PC is connected to a host PC (experimenter's workstation) through TCP/IP communication protocol. The setup uses real-time control software QUARC with QNX Neutrino real-time operating system to execute control algorithm downloaded on the target PC. The QUARC toolbox in MATLAB Simulink is used to provide Graphical User Interface (GUI) for the data flow through the data acquisition board and also to provide a

platform for the optimization algorithm written in MATLAB script to implement online optimization of controller parameters. During online tuning, an acrylic mount surrounding the moving handle and fixed to the restriction plate is used to inhibit the piston movement. For normal operation, this mount is removed to allow piston movement during force control.

TABLE 6.2 PARAMETERS OF THE EXPERIMENTAL SETUP

Parameter	Description	Value	Unit
P_s	Supply pressure	0.5	MPa
P_{atm}	Atmosphere pressure	0.1	MPa
m_p	Total mass of piston-rod assembly and attached accessories	0.5	kg
L	Piston stroke	0.05	m
A_1	Piston annulus area – side 1	67.7e-6	m^2
A_2	Piston annulus area – side 2	60.0e-6	m^2
T	Temperature of air	300	K
α	Pressure-volume work correction factor	1.2	-
C_d	Valve coefficient of discharge	0.18	-
w	Valve orifice area gradient	22.6e-3	m^2/m
K_v	Valve spool position gain	0.25e-3	m/V
τ_v	Valve response time	4.2e-3	s
P_{cr}	Valve critical pressure ratio	0.528	-
L_T	Length of connecting pneumatic tubes	9	m
D	Inner diameter of connecting pneumatic tubes	2.184e-3	m
D_o	Outer diameter of connecting pneumatic tubes	3.175e-3	m

6.2.2 Results

To validate simulation results, the performance of the controller based on the proposed nonlinear integral sliding surface is evaluated and compared against the one based on linear integral sliding surface. In this experimental analysis, the controller parameters are optimized online for the desired system response in an effort for improved tuning. The tuning process used for experiments is exactly similar to the one used earlier as described in Section 6.1 with an exception. It uses the algorithm-controlled, logically-guided iterative runs of the actual physical system and not the

simulating model. Except for that, the process uses exactly the same optimization algorithm, bounds on controller parameters, objective function, and test signal. The details of the online tuning setup required for this algorithm-guided online tuning have been given earlier in Chapter 4. Piston position is kept fixed during the system's iterative runs for online tuning. The optimized controller parameters obtained through online tuning are shown in Table 6.3.

TABLE 6.3 BOUNDS ON CONTROLLER PARAMETERS AND THEIR ONLINE OPTIMIZED VALUES (EXPERIMENTS)

Parameter	**Description**	**Bounds**		**Optimized Value**	**Unit**
		Minimum	**Maximum**		
LISS					
G	Robustness parameter	0	200	13.9063	N/s^2
λ	Controller bandwidth parameter	0	100	12.5394	rad/s
φ	Boundary layer thickness	10	10	10	N/s
NLISS					
G	Robustness parameter	0	200	111.7921	N/s^2
λ	Controller bandwidth parameter	0	100	64.4264	rad/s
φ	Boundary layer thickness	10	10	10	N/s
c_1	Design parameter for proposed nonlinear integral sliding surface	0	500	497.7558	rad/s
c_2	Design parameter for proposed nonlinear integral sliding surface	0	40	39.704	N

The system responses obtained in experiments under the controllers based on linear and proposed nonlinear integral sliding surfaces are shown in Figure 6.9. The system under the controller based on the linear integral sliding surface has a maximum overshoot of 25.65% with a settling time of 1.17s (5% criterion) in tracking a bipolar square pulse train of 20N amplitude at a rate of 30 pulses per minute. On the other hand, the system shows almost no overshoot with an average settling time of 0.29s (5% criterion) under the controller based on the proposed nonlinear integral sliding surface in tracking the same force trajectory. The average system rise times (90%) are almost identical in both cases with 0.28s under the controller based on linear integral sliding

surface and that of 0.27s under the one based on the proposed nonlinear integral sliding surface.

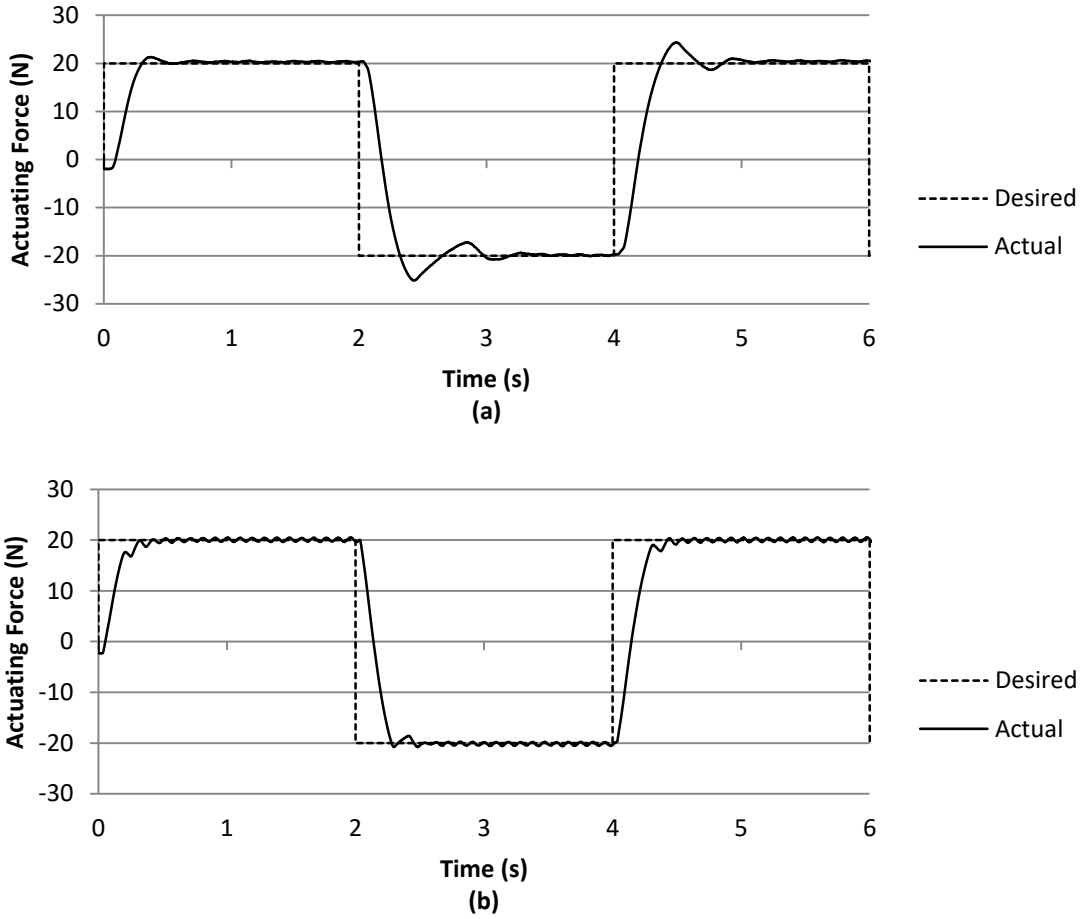

Figure 6.9 Experimental results of actuating force control using (a) LISS and (b) NLISS

The tracking errors in the system responses under the force controllers examined in this chapter are shown in Figure 6.10, which indicate that the system approaches a steady state with zero steady-state error in both cases.

The control signals and valve spool displacements under the controllers based on linear and proposed nonlinear integral sliding surfaces are shown in Figures 6.11 and 6.12, respectively. There are some spikes of +5V and -5V in control signal with the proposed nonlinear integral sliding surface. As discussed earlier in simulation studies,

these spikes occur when system requires large spool velocities to keep tracking the desired trajectory for instance on the reversal of the direction of system response. This also shows that the controller based on the proposed sliding surface can afford larger spool velocities for lower rise and settling times without producing any overshoot which is not possible with linear integral sliding surface. The plots of spool displacements show that under both controllers, the amplitudes of valve chattering are extremely attenuated.

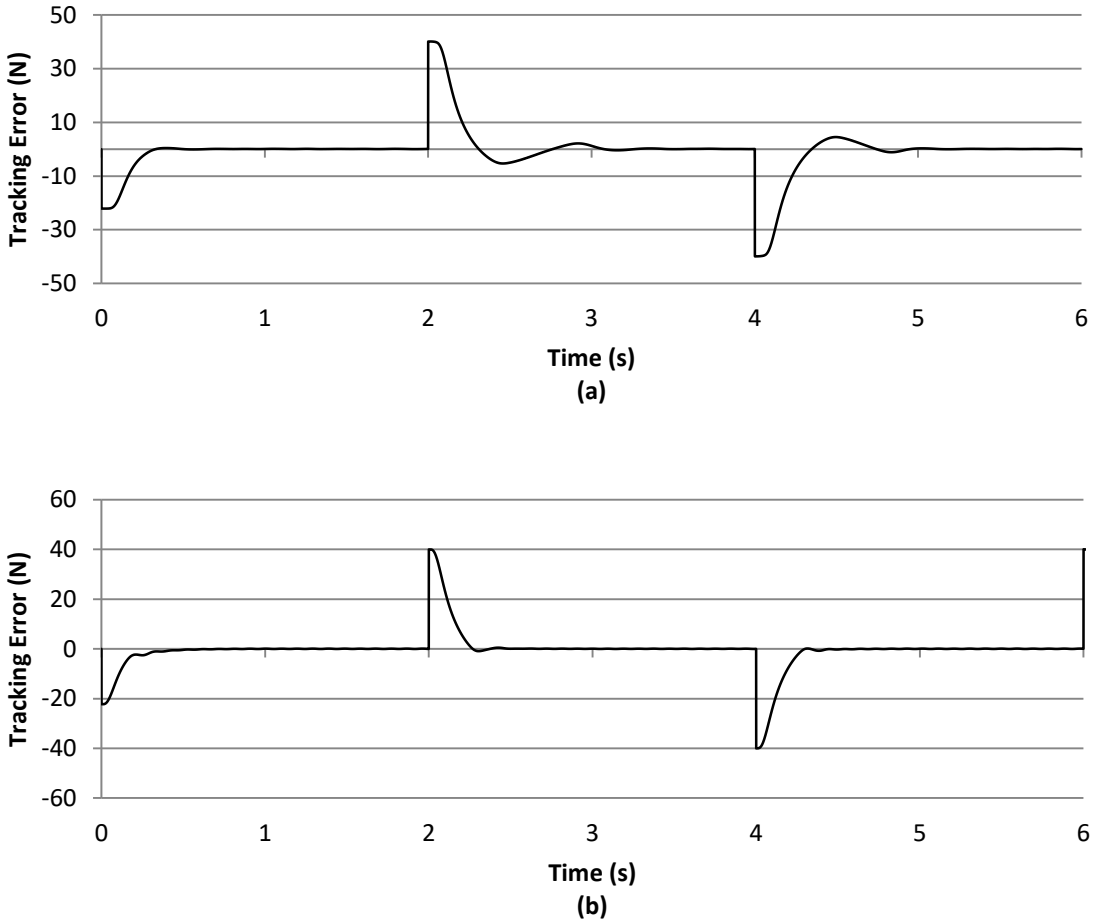

Figure 6.10 Tracking errors under (a) LISS and (b) NLISS (experiments)

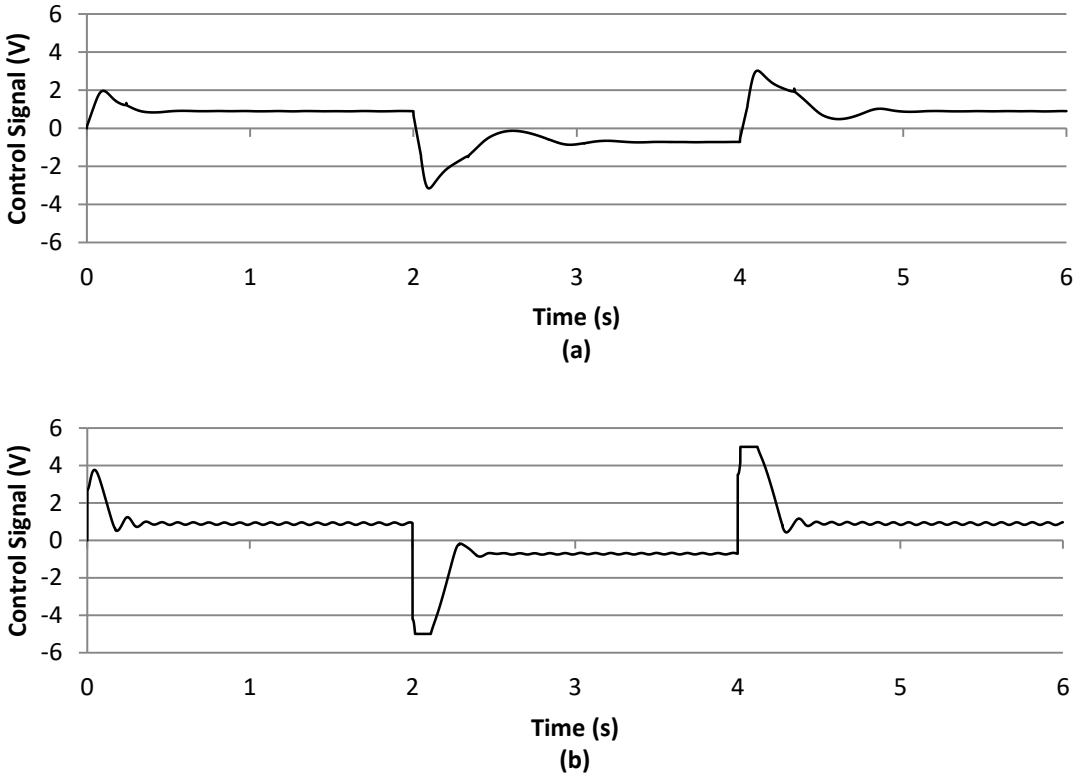

Figure 6.11 Control signals of (a) LISS and (b) NLISS (experiments)

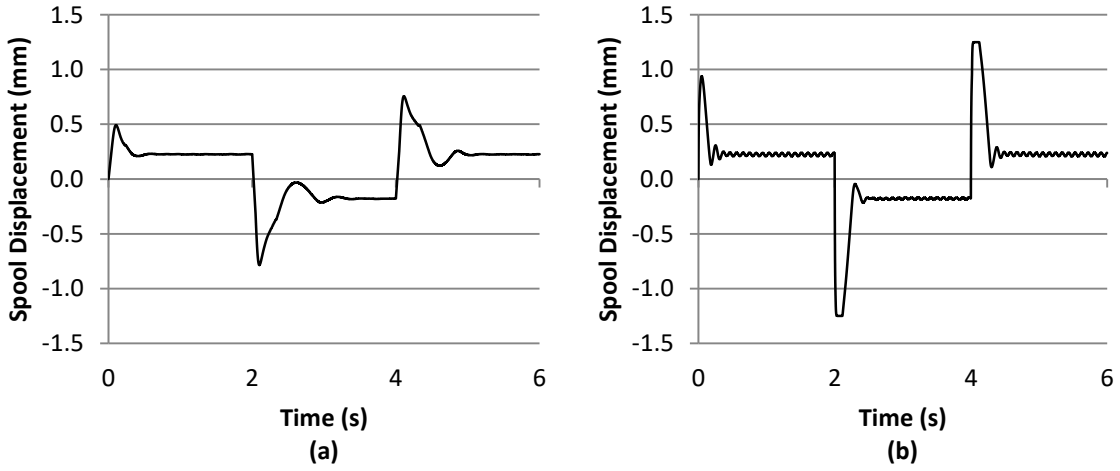

Figure 6.12 Valve spool displacements under (a) LISS and (b) NLISS (experiments)

The measurements of cylinder pressures obtained using distant pressure transducers connected to the pneumatic cylinder using long transmission lines are compared against the actual cylinder pressures in Figure 6.13. As expected, the feedback pressure measurements are time-shifted and lead-compensated with respect to

the actual cylinder pressures. Figure 6.14 shows that the first order linear transfer function with time delay model of pneumatic tube determined using system identification for indirect measurements of cylinder pressures performs very well. It estimates the pressure measurements with reasonable accuracy and thus helps implement a high-performance force control on the actuator without using force sensor or direct pressure measurements.

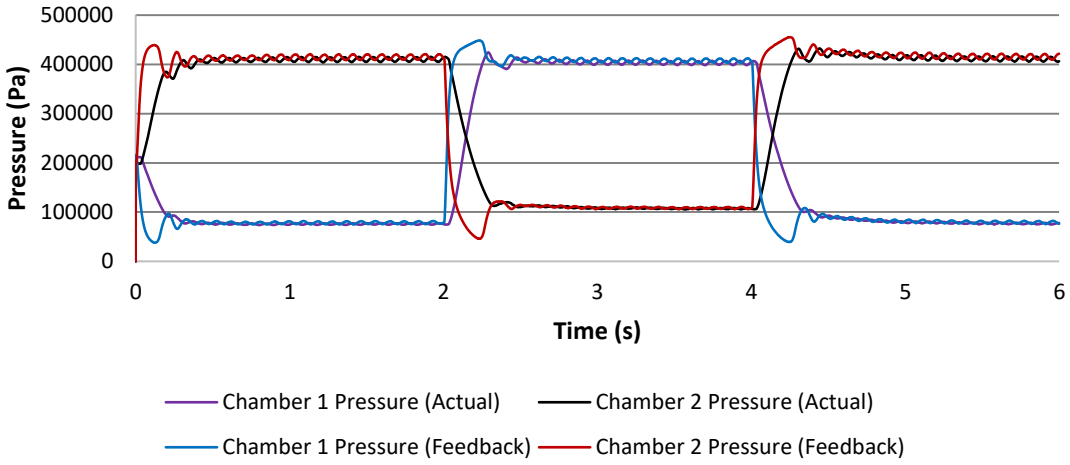

Figure 6.13 Cylinder pressures during force control under NLISS (experiments)

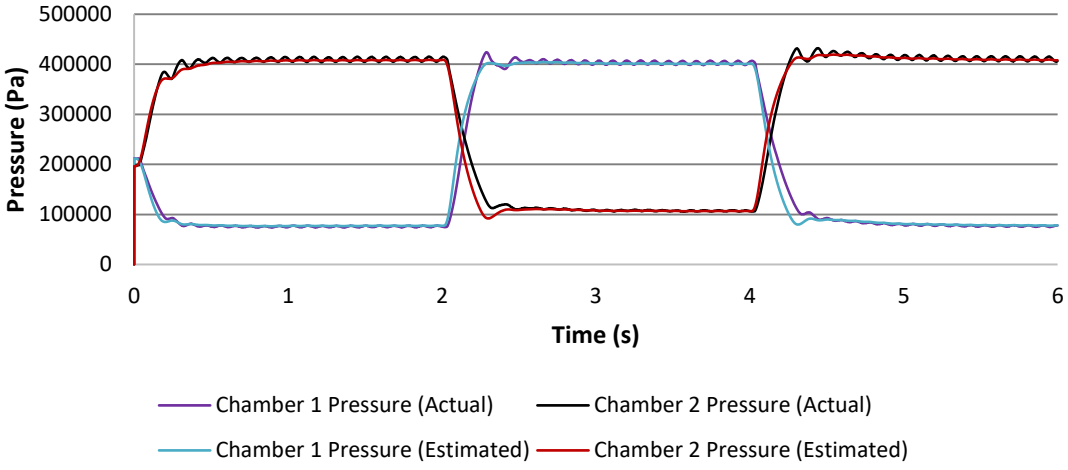

Figure 6.14 Estimation of cylinder pressures by the approximate pneumatic tube model during force control under NLISS (experiments)

The -3dB bandwidth of the force-controlled pneumatic actuator with 9m long transmission lines under the controller with the proposed NLISS at optimized controller parameters is 2.85Hz. It has been measured by changing the frequency of the input sinusoid to the control system in the range of 1-3Hz with the increment of 0.05Hz and observing the amplitude of the output. Figure 6.15 shows the frequency response of the control system at 2.85Hz.

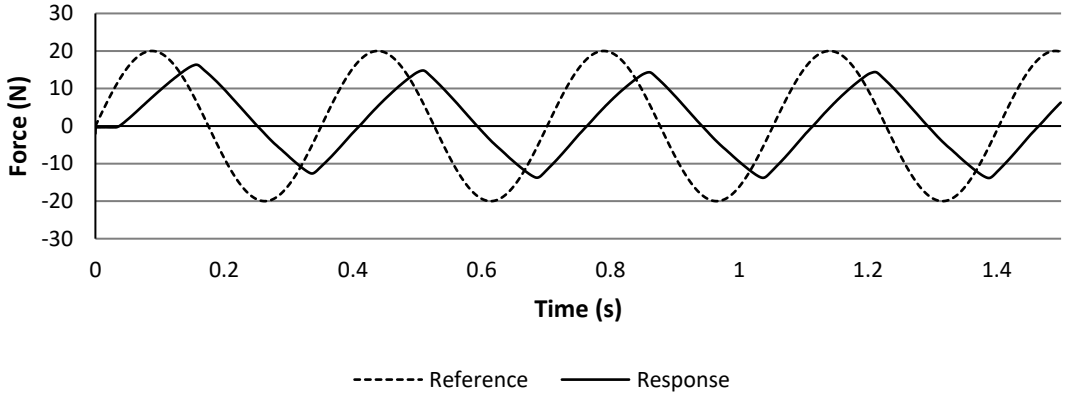

Figure 6.15 Frequency response of the actuator at 2.85Hz under NLISS (experiments)

All the results shown above have been taken in the case where the piston is fixed at one position. The performance of the controller based on the proposed nonlinear integral sliding surface needs to be evaluated as well in the case where the piston is changing its position. For this purpose, the piston is displaced as shown in Figure 6.16 using an external human force during control operation while tracking a step input. This challenges the control system to maintain the steady state because of expansion and contraction of chamber volumes. The result shown in Figure 6.17 indicates that the performance of the controller based on the proposed sliding surface does not deteriorate in the case where the piston is changing its position and the system is able to maintain steady state despite changes in chamber volumes.

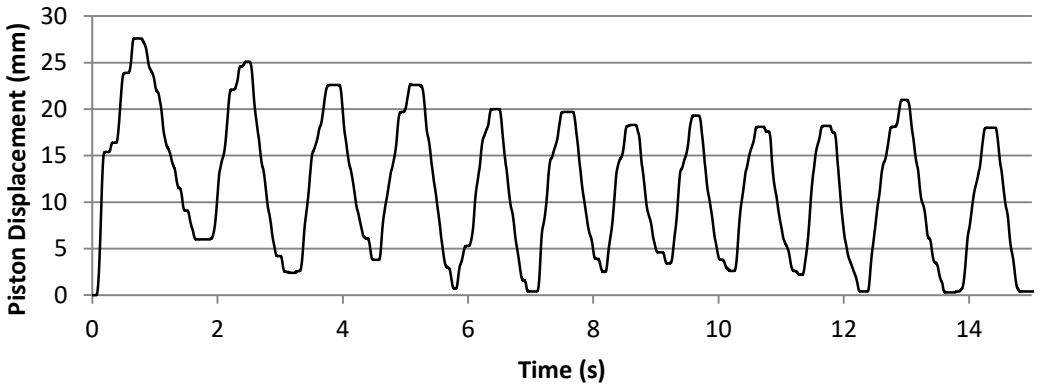

Figure 6.16 Change in piston position using external human force while tracking a step input under NLISS (experiments)

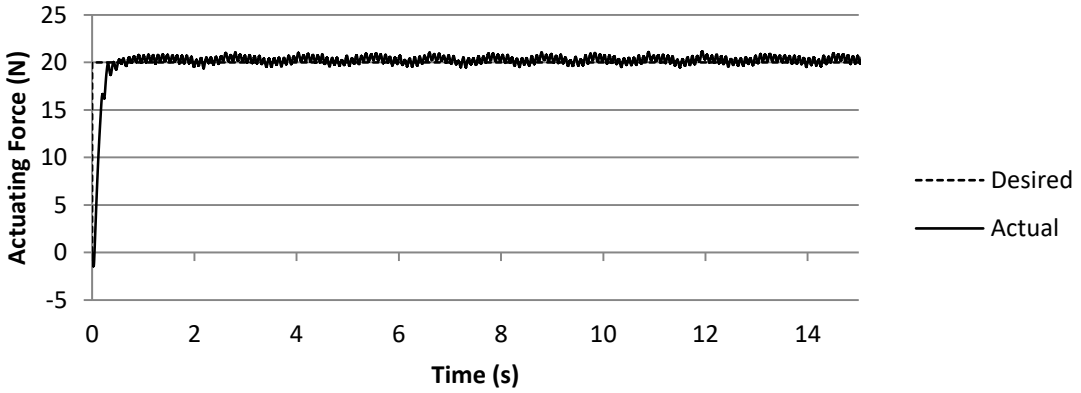

Figure 6.17 Experimental results of actuating force control under NLISS in case of piston changing its position

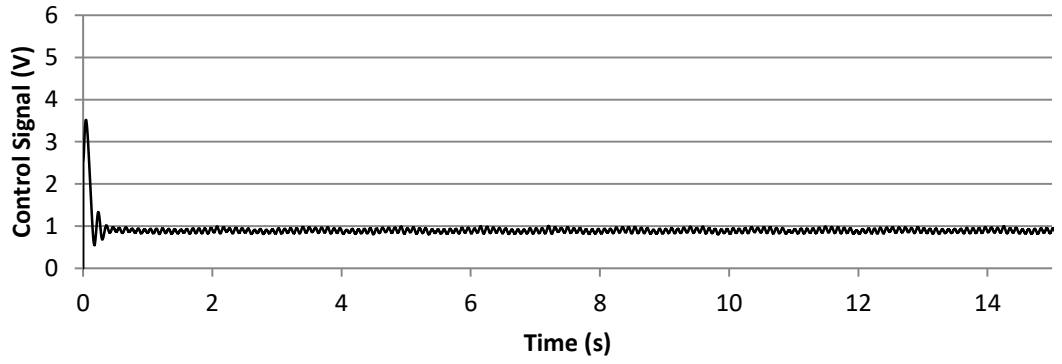

Figure 6.18 Control signal of NLISS for actuating force control in case of piston changing its position (experiments)

6.3 Summary

The performances of controllers based on linear and proposed nonlinear integral sliding surfaces for a force controlled pneumatic actuator with long transmission lines and indirect pressure measurements were compared. Simulation and experimental results were presented. For an unbiased and effective comparison, the parameters of both the controllers were tuned for the desired system response using the proposed optimization algorithm driven tuning. The controller based on the proposed nonlinear integral sliding surface outperformed the one based on linear integral sliding surface. The controller based on the proposed nonlinear integral sliding surface successfully eliminated the overshoot in the transient response of the actuator without compromising controller bandwidth, rise, and settling times.

Chapter 7

Conclusions

This thesis proposed and implemented a novel nonlinear integral sliding surface to design a full order sliding mode controller for a force-controlled pneumatic actuator with long transmission lines and indirect pressure measurements. The proposed sliding surface did not have a reaching phase in case of initial error and even multiple steps in the desired trajectory. Therefore, the robustness against matched uncertainties was guaranteed throughout the system response. The proposed sliding surface enabled the sliding mode controller to offer a variable damping during the system response. The variable damping successfully avoided the trade-off between overshoot and rise and settling times, which otherwise always existed in the presence of a linear sliding surface. The controller exploited this feature to eliminate the overshoot in the response of the actuator without compromising rise and settling times. The stability analysis of the force controller built upon the proposed sliding surface showed that the controller was asymptotically stable if a condition on the robustness parameter of the controller was satisfied. The performances of the force controllers based on linear and proposed nonlinear integral sliding surfaces were examined on a purpose-built experimental setup consisting of an MRI-compatible pneumatic gripper with 9m long transmission lines between valve and cylinder and distant pressure transducers. The gripper was also

subjected to an uncertain human force. For performance evaluation, bipolar square pulses were used as test signals as they subject the system to large initial error and discontinuities in the desired trajectory. The controller with the proposed sliding surface outperformed the one having a linear integral sliding surface in terms of the transient response of the actuator. The superior performance rendered by the controller with the proposed sliding surface justified its use in developing a sliding mode controller for a high-performance force-controlled pneumatic actuator with long transmission lines and indirect pressure measurements. The approximate linear transfer function with time delay model of the 9m long pneumatic tube provided a reasonable estimation of chamber pressures for feedback and thus provided a solution to implement sliding mode force control on pneumatic actuators in MRI-environment without using MRI-compatible force sensor and pressure transducers. This feature can be exploited for the cost-effective and time-efficient development of MRI-compatible force control applications.

The thesis also presented a novel globalized multimodal optimization algorithm and applied it for model-based offline and model-free online tuning of controller parameters. The algorithm had improved globalization and lower numerical cost in solving multimodal optimization problems in comparison to global population-based and other globalized local search algorithms. When tested on 10 complex multimodal optimization benchmarks, the algorithm achieved a global minimum in all cases and outperformed GA with elitism, PSO with adaptive inertia, PSO with linearly decreasing weights, and Luersen's GBNM with probabilistic restarts. The algorithm achieved globalization with exceedingly lower numerical cost in all cases. These features made

algorithm an excellent choice for time-efficient tuning of controller parameters, which is also a multimodal optimization problem in nature.

The effectiveness of the proposed algorithm for model-based offline and model-free online tuning was examined by applying it to a servo pneumatic position control application with performance reported earlier after rigorous manual tuning using trial-and-error. The model-based offline tuning based on the proposed algorithm improved the performance by up to 42% which improved further by up to 21% with model-free online tuning using the same algorithm. The performance improvement was obtained without any human effort for tuning in as little as 50s for model-based offline tuning and 4h for model-free online tuning. The thesis, therefore, suggested that model-based offline tuning based on the proposed algorithm presented a favorable option for precise tuning where a sufficiently adequate system model was available or system iterative runs were time-consuming or expensive. Otherwise, the proposed algorithm-driven model-free online tuning should be opted for a time-efficient and improved tuning. The results also suggested that drawing conclusions on the capability of controllers on the basis of trial-and-error tuning despite expertise, greater effort and spending more time was inaccurate. Time-efficient, logically driven tuning methods provide a reliable platform for unbiased comparison of performances of control schemes under consideration.

7.1 Research Contributions

The contributions made by this research are:

- A novel nonlinear integral sliding surface has been proposed and implemented for a high-performance force-controlled pneumatic actuator with long transmission lines and indirect pressure measurements.
- A novel globalized multimodal optimization algorithm, which has improved globalization and lower numerical cost in solving multimodal optimization problems, has been proposed.
- The proposed optimization algorithm has been applied towards time-efficient model-based offline and model-free online precise tuning of controllers to draw conclusions on their capabilities.
- An MRI-compatible test-rig, which can also be used for position control, impedance control, and admittance control applications in MRI environment, has been developed.
- Offline and online tuning setups, which are extendible to other control applications, have been proposed.
- A generalized MATLAB code of the proposed optimization algorithm has been developed for solving nth-dimensional optimization problems with single objective or aggregated multi-objective cost function.

7.2 Future Work

This research will lead to the future work, which includes but is not limited to the following:

- The performance of the force controller based on the proposed nonlinear integral sliding surface can be improved further by incorporating valve spool inertia in system dynamics and compensating for valve dead-zone.
- A fMRI-compatible impedance control application can be built upon the proposed nonlinear integral sliding surface and the developed test rig for investigative studies.
- The power grip is an important study tool for investigation of motor control with fMRI [Ehrsson, Fagergren, Jonsson, Westling, Johansson, & Forssberg, 2000; Ward, & Frackowiak, 2003; Floyer-Lea, & Matthews, 2004; Halder et al, 2007; Ward, Swayne, & Newton; 2008] and is especially useful in patients with motor disorders [Binkofski et al, 1998; Ward, Brown, Thompson, & Frackowiak, 2003a; Ward, Brown, Thompson, & Frackowiak, 2003b; Ward et al, 2007]. Motor control patients can be asked to trace a continuously changing target by adjusting their isometric grip force over a defined period of time under fMRI. The exercise can help investigate the neural signatures of demand task and feedback accuracy on grip force tracking [Sterr, Shen, Kranczioch, Szameitat, Hou, & Sorger, 2009]. The MRI-compatible force control application developed in this research can be used as a tool for such research studies. The controlled stiffness levels during the tasks may help draw new correlations and relationships for human motor control studies in future.

References

Abd El Khalick Mohammad, A. M., Uchiyama, N., & Sano, S. (2015). Energy saving in feed drive systems using sliding-mode-based contouring control with a nonlinear sliding surface. *IEEE/ASME Transactions on Mechatronics, 20*(2), 572-579.

Astrakas, L. G., Naqvi, S. H., Kateb, B., & Tzika, A. A. (2012). Functional MRI using robotic MRI compatible devices for monitoring rehabilitation from chronic stroke in the molecular medicine era. *International Journal of Molecular Medicine, 29*(6), 963-973.

Bandyopadhyay, B., & Fulwani, D. (2009). High performance tracking controller for discrete plant using non-linear sliding surface. *IEEE Transactions on Industrial Electronics, 56,* 3628–3637.

Bandyopadhyay, B., Fulwani, D., Postletwaithe, I., & Turner, M.C. (2010). A nonlinear sliding surface to improve performance of a discrete-time input-delay system. *International Journal of Control, 83*(9), 1895-1906.

Boubakir, A., Labiod, S., & Boudjema, F. (2012). A stable self-tuning proportional-integral-derivative controller for a class of multi-input multi-output nonlinear systems. *Journal of Vibration and Control, 18*(2), 228-239.

Binkofski, F., Dohle, C., Posse, S., Stephan, K. M., Hefter, H., Seitz, R. J., & Freund, H. J. (1998). Human anterior intraparietal area subserves prehension A combined lesion and functional MRI activation thesis. *Neurology*, *50*(5), 1253-1259.

Cao, W., & Xu, J. (2004). Nonlinear integral type sliding surface for both matched and unmatched uncertain systems. *IEEE Transactions on Automatic Control, 49*(8), 1355–1360.

Castanos, F., & Fridman, L. (2006). Analysis and design of integral sliding manifolds for systems with unmatched perturbations. *IEEE Transactions on Automatic Control*, *51*(5), 853–858.

Chapius, D., Gassert, R., Burdet, E., & Bleuler, H. (2008). A hybrid ultrasonic motor and electrorheological fluid clutch actuator for force feedback in MRI/fMRI. In *Proceedings of the 30th International IEEE EMBS Conference* (pp. 3438-3442). Vancouver, British Columbia: IEEE.

Chen, B.M., Lee, T.H., Peng, K., & Venkataramanan, V. (2003). Composite nonlinear feedback control for linear systems with input saturation: Theory and an application. *IEEE Transactions on Automatic Control*, *48*, 427–439.

Chiha, I., Liouane, N., & Borne, P. (2012). Tuning PID controller using multiobjective ant colony optimization. *Applied Computational Intelligence and Soft Computing*, *2012*, 11.

Colombo, R., Pisano, F., Mazzone, A., Delconte, C., Micera, S., Carrozza, M. C., & Minuco, G. (2007). Design strategies to improve patient motivation during robot-aided rehabilitation. *Journal of Neuroengineering and Rehabilitation*, *4*(1), 3.

dos Santos Coelho, L., & Coelho, A. A. R. (2009). Model-free adaptive control optimization using a chaotic particle swarm approach. *Chaos, Solitons & Fractals*, *41*(4), 2001-2009.

Ehrsson, H. H., Fagergren, A., Jonsson, T., Westling, G., Johansson, R. S., & Forssberg, H. (2000). Cortical activity in precision-versus power-grip tasks: an fMRI thesis. *Journal of Neurophysiology*, *83*(1), 528-536.

Elhawary, H., Zivanovic, A., Davies, B., & Lamperth, M. (2006). A review of magnetic resonance imaging compatible manipulators in surgery. *Proceedings of the Institution of Mechanical Engineers, Part H: Journal of Engineering in Medicine*, *220*(3), 413-424.

Fasoli, S. E., Krebs, H. I., Stein, J., Frontera, W. R., & Hogan, N. (2003). Effects of robotic therapy on motor impairment and recovery in chronic stroke. *Archives of Physical Medicine and Rehabilitation*, *84*(4), 477-482.

Fischer, G. S., Krieger, A., Iordachita, I., Csoma, C., Whitcomb, L. L., & Fichtinger, G. (2008, September). MRI compatibility of robot actuation techniques–a comparative thesis. In *International Conference on Medical Image Computing and Computer-Assisted Intervention* (pp. 509-517). Springer, Berlin, Heidelberg.

Floyer-Lea, A., & Matthews, P. M. (2004). Changing brain networks for visuomotor control with increased movement automaticity. *Journal of Neurophysiology*, *92*(4), 2405-2412.

Forrest, S., & Mitchell, M. (1993). What makes a problem hard for a genetic algorithm? Some anomalous results and their explanation. In *Genetic Algorithms for Machine Learning* (pp. 129-163). Springer, Boston, MA.

Gao, Z., & Liao, X. (2013). Integral sliding mode control for fractional-order systems with mismatched uncertainties. *Nonlinear Dynamics*, *72*(1-2), 27–35.

Guin, J. A. (1968). Modification of the complex method of constrained optimization. *The Computer Journal*, *10*(4), 416-417.

Halder, P., Brem, S., Bucher, K., Boujraf, S., Summers, P., Dietrich, T., & Brandeis, D. (2007). Electrophysiological and hemodynamic evidence for late maturation of hand power grip and force control under visual feedback. *Human Brain Mapping*, *28*(1), 69-84.

Hamayun, M.T., Edwards, C., & Alwi, H. (2016). Integral sliding mode control. Fault Tolerant Control Schemes using Integral Sliding Modes, 17-37, Springer Cham.

Kennedy, J., & Spears, W. M. (1998, May). Matching algorithms to problems: an experimental test of the particle swarm and some genetic algorithms on the multimodal problem generator. In *Proceedings of the IEEE International Conference on Evolutionary Computation*(pp. 78-83). Anchorage: IEEE.

Killingsworth, N. J., & Krstic, M. (2006). PID tuning using extremum seeking: online, model-free performance optimization. *IEEE Control Systems*, *26*(1), 70-79.

Kim, D. H. (2011). Hybrid GA–BF based intelligent PID controller tuning for AVR system. *Applied Soft Computing*, *11*(1), 11-22.

Le, T. D., Kang, H. J., Suh, Y. S., & Ro, Y. S. (2013). An online self-gain tuning method using neural networks for nonlinear PD computed torque controller of a 2-dof parallel manipulator. *Neurocomputing*, *116*, 53-61.

Liu, S. J., & Krstic, M. (2012). *Stochastic averaging and stochastic extremum seeking*. Springer Science & Business Media.

Lin, Z., Pachter, M., & Banda, S. (1998). Towards improvement of tracking performance nonlinear feedback for linear Systems. *International Journal of Control, 70,* 1–11.

Luersen, M. A., & Le Riche, R. (2004). Globalized Nelder–Mead method for engineering optimization. *Computers & Structures*, *82*(23-26), 2251-2260.

Matthews, G.P., & DeCarlo, R.A. (1988). Decentralized tracking for a class of interconnected nonlinear systems using variable structure control. *Automatica*, *24*(2), 187-193.

Nelder, J. A., & Mead, R. (1965). A simplex method for function minimization. *The Computer Journal*, *7*(4), 308-313.

Oliveira, J. B., Boaventura-Cunha, J., Oliveira, P. M., & Freire, H. (2014). A swarm intelligence-based tuning method for the sliding mode generalized predictive control. *ISA Transactions*, *53*(5), 1501-1515.

Padula, F., & Visioli, A. (2011). Tuning rules for optimal PID and fractional-order PID controllers. *Journal of Process Control*, *21*(1), 69-81.

Prange, G. B., Jannink, M. J., Groothuis-Oudshoorn, C. G., Hermens, H. J., & IJzerman, M. J. (2006). Systematic review of the effect of robot-aided therapy on recovery of the hemiparetic arm after stroke. *Journal of Rehabilitation Research and Development*, *43*(2), 171-184.

Rahman, R. A., He, L., & Sepehri, N. (2016). Design and experimental thesis of a dynamical adaptive backstepping–sliding mode control scheme for position tracking and regulating of a low-cost pneumatic cylinder. *International Journal of Robust and Nonlinear Control*, *26*(4), 853-875.

Reynoso-Meza, G., Garcia-Nieto, S., Sanchis, J., & Blasco, F. X. (2013). Controller tuning by means of multi-objective optimization algorithms: A global tuning framework. *IEEE Transactions on Control Systems Technology*, *21*(2), 445-458.

Richer, E., & Hurmuzlu, Y. (2000a). A high performance pneumatic force actuator system: I. Nonlinear mathematical model. *ASME Journal of Dynamic Systems, Measurement, and Control*, *122*(3), 416-425.

Richer, E., & Hurmuzlu, Y. (2000b). A high performance pneumatic force actuator system. II. Nonlinear controller design. *ASME Journal of Dynamic Systems, Measurement, and Control, 122*(3), 426-434.

Ripamonti, F., Orsini, L., & Resta, F. (2017). A nonlinear sliding surface in sliding mode control to reduce vibrations of a three-link flexible manipulator. *Journal of Vibration and Acoustics, 139*(5), 051005.

Sergi, F., Erwin, A. C., & O'Malley, M. K. (2015). Interaction control capabilities of an MR-compatible compliant actuator for wrist sensorimotor protocols during fMRI. *IEEE/ASME Transactions on Mechatronics*, *20*(6), 2678-2690.

Shen, X. (2010). Nonlinear model-based control of pneumatic artificial muscle servo systems. *Control Engineering Practice*, *18*(3), 311-317.

Shen, X., Zhang, J., Barth, E. J., & Goldfarb, M. (2006). Nonlinear model-based control of pulse width modulated pneumatic servo systems. *Journal of Dynamic Systems, Measurement, and Control*, *128*(3), 663-669.

Shtessel, Y., Edwards, C., Fridman, L., & Levant, A. (2014). *Sliding mode control and observations*. New York: Springer.

Singer, S., & Nelder, J. (2009). Nelder-mead algorithm. *Scholarpedia*, *4*(7), 2928.

Slotine, J. J. E., & Li, W. (1991). *Applied nonlinear control* (Vol. 199, No. 1). Englewood Cliffs, NJ: Prentice hall.

Sterr, A., Shen, S., Kranczioch, C., Szameitat, A. J., Hou, W., & Sorger, B. (2009). fMRI effects of task demand and feedback accuracy on grip force tracking. *Neuroscience Letters*, *457*(2), 61-65.

Stoianovici, D., Song, D., Petrisor, D., Ursu, D., Mazilu, D., Mutener, M., & Patriciu, A. (2007). "MRI Stealth" robot for prostate interventions. *Minimally Invasive Therapy & Allied Technologies*, *16*(4), 241-248.

Turkseven, M., & Ueda, J. (2017). An asymptotically stable pressure observer based on load and displacement sensing for pneumatic actuators with long transmission lines. *IEEE/ASME Transactions on Mechatronics, 22*(2), 681-692.

Turner, M.C., & Postlethwaite, I. (2004). Nonlinear regulation in constrained input discrete time linear systems. *International Journal of Control, 77,* 1330–1342.

Turner, M.C., Postlethwaite, I., & Walker, D.J. (2000). Nonlinear tracking control for multivariable constrained input linear systems. *International Journal of Control, 73,* 1160–1172.

Tursini, M., Parasiliti, F., & Zhang, D. (2002). Real-time gain tuning of PI controllers for high-performance PMSM drives. *IEEE Transactions on Industry Applications, 38*(4), 1018-1026.

Utkin, V., Guldner, J., & Shi, J. (1999). *Sliding mode control in electromechanical system.* London: Taylor and Francis.

Utkin, V., & Shi, J. (1996). Integral sliding mode in systems operating under uncertainty conditions. In *Proceedings of the IEEE Conference on Decision and Control*(pp. 4591-4596). Kobe: IEEE.

Venkataramanan, V., Peng, K., & Chen, B.M. (2003). Discrete-time composite nonlinear feedback control with an application in design of a hard disk servo system. *IEEE Transactions on Control System Technology, 48,* 427–439.

Vigaru, B., Sulzer, J., & Gassert, R. (2016). Design and evaluation of a cable-driven fmri-compatible haptic interface to investigate precision grip control. *IEEE Transactions on Haptics*, *9*(1), 20-32.

Wade, E., & Winstein, C. J. (2011). Virtual reality and robotics for stroke rehabilitation: where do we go from here? *Topics in Stroke Rehabilitation*, *18*(6), 685-700.

Ward, N. S., Brown, M. M., Thompson, A. J., & Frackowiak, R. S. J. (2003a). Neural correlates of outcome after stroke: a cross-sectional fMRI thesis. *Brain*, *126*(6), 1430-1448.

Ward, N. S., Brown, M. M., Thompson, A. J., & Frackowiak, R. S. J. (2003b). Neural correlates of motor recovery after stroke: a longitudinal fMRI thesis. *Brain*, *126*(11), 2476-2496.

Ward, N. S., & Frackowiak, R. S. J. (2003). Age-related changes in the neural correlates of motor performance. *Brain*, *126*(4), 873-888.

Ward, N. S., Newton, J. M., Swayne, O. B., Lee, L., Frackowiak, R. S., Thompson, A. J., & Rothwell, J. C. (2007). The relationship between brain activity and peak grip force is modulated by corticospinal system integrity after subcortical stroke. *European Journal of Neuroscience*, *25*(6), 1865-1873.

Ward, N. S., Swayne, O. B., & Newton, J. M. (2008). Age-dependent changes in the neural correlates of force modulation: an fMRI thesis. *Neurobiology of Aging, 29*(9), 1434-1446.

Wang, J., Lee, T., & Juang, Y. (1996). New methods to design an integral variable structure controller. *IEEE Transactions on Automatic Control, 41*(1), 140–143.

Wolpert, D. H., & Macready, W. G. (1995). *No free lunch theorems for search* (Vol. 10). Technical Report SFI-TR-95-02-010, Santa Fe Institute.

Xu, J., Pan, Y., & Lee, T. (2003). Analysis and design of integral sliding mode control based on Lyapunov's direct method. In *Proceedings of the American Control Conference*(pp. 192-196). Denver: IEEE.

Yang, B., Tan, U., McMillan, A., Gullapalli, R., & Desai, J.P. (2011). Design and control of a 1-DOF pneumatically actuated robot with long transmission lines. *IEEE/ASME Transactions on Mechatronics, 16*(6), 1040-1048.

Yu, N., Hollnagel, C., Blickenstorfer, A., Kollias, S., & Riener, R. (2008). Comparison of MRI-compatible mechatronic systems with hydrodynamic and pneumatic actuation. *IEEE/ASME Transactions on Mechatronics, 13*(3), 268-277.

Yu, N., Murr, W., Blickenstorfer, A., Kollias, S., & Riener, R. (2007). An fMRI compatible haptic interface with pneumatic actuation. In *Proceedings of the IEEE International Conference on Rehabilitation Robotics*(pp. 714-720). Noordwijk: IEEE.